Design and Evaluation of CMUTs for Medical Ultrasound Imaging with a Focus on Non-Invasive Blood Pressure Waveform Monitoring

by

Chirag GOEL

THESIS PRESENTED TO ÉCOLE DE TECHNOLOGIE SUPÉRIEURE
IN PARTIAL FULFILLMENT OF A MASTER'S DEGREE
WITH THESIS
M.A.Sc.

MONTREAL, 23, JANUARY, 2026

ÉCOLE DE TECHNOLOGIE SUPÉRIEURE
UNIVERSITÉ DU QUÉBEC

BOARD OF EXAMINERS

THIS THESIS HAS BEEN EVALUATED

BY THE FOLLOWING BOARD OF EXAMINERS

M. Ricardo Izquierdo, memorandum supervisor
Département de génie électrique à l'École de Technologie Supérieure

M. Paul Vahe Cicek, co-supervisor
Microtechnologies Integration & Convergence Research Group, Université du Québec à Montréal (UQAM)

M. Alexandre Robichaud, co-supervisor
Department of Applied Sciences, Université du Québec à Chicoutimi (UQAC)

M. Dominic Deslandes, president of the board of examiners
Département de génie électrique à l'École de Technologie Supérieure

M. Fréderic Nabki, member of the jury
Département de génie électrique à l'École de Technologie Supérieure

THIS THESIS WAS PRESENTED AND DEFENDED

IN THE PRESENCE OF A BOARD OF EXAMINERS AND THE PUBLIC

ON 16, JANUARY, 2026

AT ÉCOLE DE TECHNOLOGIE SUPÉRIEURE

ACKNOWLEDGEMENTS

I would first like to express my sincere thanks to my thesis supervisor, Professor Ricardo Izquierdo, and to Paul Vahe Cicek and Alexandre Robichaud. I would especially like to thank them for both the freedom they gave me in choosing the direction of my research project, and for their advice and ideas, which made my research what it is today.

I would also like to thank the co-author of my articles, Mathieu Gratuze. However, this list of acknowledgements would not be complete if I did not include my colleagues Normand Gravel, Musthafa, and Oliver Richard, as well as my friends at the Laboratoire de Communications et d'Intégration de la MicroÉlectronique (LaCIME) and at the École de technologie supérieure.

I would also like to thank all those who contributed to this thesis. I must mention in particular CMC Microsystems, which provided the design tools and enabled the fabrication of the various MEMS chips developed during this master's.

Finally, I would also like to thank my parents and my brother for their support throughout my life and my studies. Dad, Mom, thank you! Without you, none of this would have been possible.

Conception et évaluation de CMUT pour l'imagerie médicale par ultrasons, en mettant l'accent sur la surveillance non invasive de la courbe de pression artérielle

Chirag GOEL

RÉSUMÉ

Cette thèse étudie les transducteurs ultrasonores micromachiné (MUT) pour la surveillance non invasive de la forme d'onde de la pression artérielle (PA), en mettant plus particulièrement l'accent sur les transducteurs ultrasonores micromachiné capacitifs (CMUT). Le travail combine : (i) une revue critique des dispositifs ultrasonores pour la mesure de la forme d'onde de PA ; (ii) une analyse expérimentale de la topologie des CMUT, du facteur de qualité et de l'amortissement ; et (iii) le développement d'un procédé de fabrication hybride de type CMUT intégrant des conducteurs imprimés avec des cavités et des membranes issues de la microfabrication de surface.

Premièrement, la thèse présente une revue de la littérature sur les dispositifs ultrasonores pour la surveillance continue et non invasive de la forme d'onde de PA, en examinant les approches à base de transducteurs piézoélectriques massifs, de PMUT et de CMUT. L'analyse met en évidence que la plupart des systèmes rapportés reposent encore sur des sondes massives ou sur des PMUT, et que les solutions fondées sur des CMUT en particulier sur des substrats flexibles ou à faible coût restent largement sous-explorées.

Deuxièmement, quatre topologies de CMUT, fabriquées par le procédé PolyMUMPs, sont étudiées, combinant des bras de type ressorts ou rectilignes avec des ancrages basculants (« rocker ») ou fixes. La vibrométrie laser Doppler en air et sous vide est utilisée pour mesurer la fréquence de résonance et le facteur de qualité en fonction de la tension de polarisation continue et de l'excitation alternative. Un point de fonctionnement commun, normalisé par rapport à la tension de pull-in, est défini, et les données mesurées air/vide sont analysées à l'aide d'un modèle additif, afin de séparer les pertes fluidiques des pertes intrinsèques. La comparaison des quatre permutations montre que les ancrages basculants constituent la principale source de pertes intrinsèques, ce qui les rend adaptés aux applications à faible facteur de qualité, où une haute résolution axiale est recherchée, tandis que les bords rectilignes à ancrage fixe procurent un facteur Q élevé, mieux adapté aux opérations d'émission/réception efficaces.

Enfin, une structure hybride de type CMUT est réalisée sur verre en combinant une électrode inférieure en aluminium déposée par pulvérisation cathodique, une couche sacrificielle en LOR lithographiée avec AZ 5214E, une membrane en SU-8 percée de trous de gravure et une électrode supérieure en argent sérigraphié et entièrement réticulé. La compatibilité thermique et chimique du procédé est établie, et un réseau 2×2 est fabriqué. Les mesures de profilométrie et de vibrométrie confirment une épaisseur d'argent imprimé d'environ 9.2 µm, deux résonances mécaniques nettes à 1.01 MHz et 1.42 MHz avec des facteurs de qualité d'environ $Q_1 \approx 6.6$ et $Q_2 \approx 235$, ainsi qu'une tension de collapse d'environ 20 V. Ces résultats montrent que des dispositifs de type CMUT peuvent être réalisés avec un ensemble réduit d'équipements,

offrant une plateforme pratique pour de futurs capteurs ultrasonores de forme d'onde de pression artérielle (BP) à faible coût et potentiellement flexibles, avec une durée de fabrication réduite.

Mots-clés: CMUT, ultrasons MEMS, facteur de qualité, amortissement, fabrication hybride, sérigraphie, pression artérielle non invasive, capteurs à ultrasons

Design and Evaluation of CMUTs for Medical Ultrasound Imaging with a Focus on Non-Invasive Blood Pressure Waveform Monitoring

Chirag GOEL

ABSTRACT

CMUT, MEMS ultrasound, quality factor, damping, hybrid fabrication, screen printing, non-invasive blood pressure, ultrasonic sensors.

This thesis investigates micromachined ultrasonic transducers (MUTs) for non-invasive blood pressure (BP) waveform monitoring, with a focus on capacitive micromachined ultrasonic transducers (CMUTs). The work combines: (i) a critical review of ultrasonic BP-waveform sensing; (ii) experimental analysis of CMUT topology, quality factor, and damping; and (iii) the development of a hybrid CMUT fabrication process that integrates printed conductors with surface-micromachined cavities and membranes.

First, four CMUT topologies fabricated in a PolyMUMPs process are studied, combining spring versus straight arms with rocker versus fixed anchoring. Laser Doppler vibrometer in air and vacuum is used to extract resonance frequency and quality factor as a function of dc bias and ac drive. A pull-in-normalized common operating point is introduced, and paired air/vacuum data are analyzed using an additive $1/Q$ model to separate fluidic and intrinsic losses. By comparing the four permutations, rocker anchors are identified as the dominant intrinsic loss source, suitable for low Q factor operations where high axial resolution is required whereas straight fixed rims provide a high-Q, suitable for efficient transmit/receive operation.

Second, the thesis reviews ultrasonic devices for continuous non-invasive BP waveform monitoring, examining bulk piezoelectric, PMUT, and CMUT approaches. The analysis highlights that most reported systems still rely on bulk probes or PMUTs, and that CMUT-based solutions—particularly on flexible or low-cost substrates—remain underexplored.

Finally, a hybrid CMUT-like structure is demonstrated on glass by combining a sputtered aluminum bottom electrode, a LOR sacrificial layer patterned with AZ 5214E, an SU-8 membrane with etch holes, and a fully cured screen-printed silver top electrode. Temperature and chemical compatibility are mapped, and a 2×2 array is fabricated. Profilometry and vibrometry confirm a printed silver thickness of approximately $9.2\,\mu$m, two clear mechanical resonances at $1.01\,$MHz and $1.42\,$MHz with quality factors of approximately $Q_1 \approx 6.6$ and $Q_2 \approx 235$, and a collapse voltage around $20\,$V. The results show that CMUT-like devices can be realized with a reduced tool set, providing a practical platform for future low-cost and potentially flexible ultrasonic BP-waveform sensors with reduced fabrication duration.

Keywords: Design and Evaluation of CMUTs for Medical Ultrasound Imaging with a Focus on Non-Invasive Blood Pressure Waveform Monitoring

TABLE OF CONTENTS

Page

INTRODUCTION 1

CHAPTER 1 REVIEW ON DEVELOPMENT OF ULTRASONIC BASED SENSORS FOR NON-INVASIVE BLOOD PRESSURE WAVEFORM MONITORING 7
1.1 Introduction 7
1.2 Ultrasound Principles for Blood-Pressure Sensing 13
1.2.1 Core Working Principle 13
1.2.2 Depth of penetration and lateral resolution 13
1.2.3 Bandwidth and axial resolution 15
1.2.4 Models Relating Artery Diameter to BP 17
1.2.4.1 Arterial wall tracking 17
1.2.4.2 Pulse transit time (PTT) and Pulse wave velocity (PWV) 19
1.2.5 Performance Parameters in the Transducer for Specific Target Applications 21
1.3 Ultrasonic transducer technologies 23
1.3.1 Bulk Transducers 23
1.3.1.1 General description and working principle 23
1.3.1.2 Fabrication 25
1.3.2 MEMS Ultrasonic Transducers 27
1.3.3 Modeling of MEMS Ultrasonic Transducers 28
1.3.4 PMUTs (Piezoelectric Micromachined Ultrasonic Transducers) 30
1.3.4.1 Fabrication of PMUTs 33
1.3.5 CMUTs (Capacitive Micromachined Ultrasonic Transducers) 35
1.3.5.1 Fabrication of CMUTs 37
1.4 Technological evolution for BP Waveform Monitoring using ultrasound transducers 38
1.4.1 Bulk Piezoelectric Transducers 38
1.4.1.1 Non-flexible substrate based devices 38
1.4.1.2 Flexible substrate based devices 41
1.4.2 PMUTs (Piezoelectric Micromachined Ultrasonic Transducers) 44
1.4.2.1 Non-flexible substrate based devices 44
1.4.2.2 Flexible devices 50
1.5 Critical review and Future Directions 52
1.5.1 Challenges and Limitations 56
1.5.2 Future Directions 58
1.6 Conclusion 59

CHAPTER 2 A METHOD FOR EXPANDING THE BANDWIDTH AND DECREASING THE ACTUATION VOLTAGE OF CMUT DEVICES 61
2.1 Introduction 63
2.2 Operating Principle 64
2.3 Methods 65
2.4 Characterization and Results 67
2.5 Conclusion 69

CHAPTER 3 DECOMPOSING INTRINSIC AND FLUIDIC LOSSES IN CMUT TOPOLOGIES: A COMPARATIVE STUDY OF ARM GEOMETRY, ANCHORING, AND ENVIRONMENT 73
3.1 Introduction 73
3.2 Methods 75
3.2.1 Devices and prior work 75
3.2.2 Electromechanical model (spring softening) 75
3.2.3 Damping model: air vs. vacuum 76
3.2.4 Pull-in-normalized operating point for Q-factor comparison 77
3.2.5 Damping decomposition at the common operating point 78
3.2.6 Voltage sensitivities of f and Q 79
3.3 Characterization and Results 79
3.3.1 Characterization Methodology 79
3.3.2 Air-coupling 80
3.3.3 Vacuum-coupling 81
3.3.4 Quality-Factor Comparison and Damping Decomposition Across CMUT Topologies 81
3.3.5 Resonant frequency dependence on bias and drive 86
3.3.6 Quality factor dependence on bias and drive 88
3.3.6.1 Observations in air 88
3.3.6.2 Observations in vacuum 89
3.4 Discussion 89
3.4.1 Anchors vs. Arms: Who Sets Q? 90
3.4.2 Frequency Tuning and Controlled Nonlinearity 90
3.4.3 Air vs. Vacuum: Fluidic vs. Structural Damping 91
3.4.4 Applicability of the Common Operating Point and $1/Q$ Decomposition Framework 91
3.4.5 Positioning Relative to Reported CMUT/PMUT Designs 92
3.5 Conclusion 96

CHAPTER 4 HYBRID SURFACE MICROMACHINED AND SCREEN PRINTED CMUT FABRICATION PROCESS 97
4.1 Introduction 97
4.2 MEMS Fabrication Strategies for Ultrasonic Devices 98
4.2.1 Conventional Silicon MEMS Platforms 98

4.2.2 Polymer and Flexible MEMS 99
4.2.3 Hybrid and Additive Approaches 99
4.3 Device Concept and Process Integration Constraints 100
4.4 Hybrid Process Development and Concept 101
4.4.1 Seed Materials and Target 101
4.4.2 Iterative Development: From Printed Stack to Hybrid Flow 101
4.4.2.1 Trial 1: Printed bottom / PR / printed top 101
4.4.2.2 Trial 2: (Lift-off resist) LOR buffer under AZ 5214E 102
4.4.2.3 Trial 3: Sputtered Al bottom / LOR+AZ / printed top 102
4.4.2.4 Trial 4 (final): Sputtered Al bottom / LOR sacrificial / SU-8 membrane / printed top 103
4.4.2.5 Release-chemistry development 103
4.4.3 Temperature compatibility 104
4.4.4 Chemical compatibility 105
4.5 Final Hybrid Fabrication Process 106
4.5.1 Materials and Equipment 106
4.5.2 Baseline process flow 107
4.6 Unit-Cell Topology and Array Layout 112
4.7 Thickness and Structural Verification 114
4.8 Summary and Outlook 115

CONCLUSION AND RECOMMENDATIONS 117
5.1 Summary of contributions 117
5.1.1 Impact of CMUT Topology on Q-Factor and Damping Mechanisms 117
5.1.2 Ultrasonic devices for non-invasive BP waveform monitoring 118
5.1.3 Hybrid surface-micromachined and screen-printed CMUT process 119
5.2 Limitations 121
5.3 Recommendations and Future work 122
5.3.1 CMUT design and damping engineering 122
5.3.2 Hybrid process and materials 122
5.4 Broader perspectives 123

APPENDIX I COMMON OPERATING POINT AND Q-FACTOR EXTRACTION 125

LISTE DE RÉFÉRENCES BIBLIOGRAPHIQUES 129

LIST OF TABLES

Page

Table 1.1 Target-specific design window for ultrasonic BP-waveform probes, expressed in the qualitative five-column layout used for technology comparisons. Depths, wall excursions and model choices are consolidated PWV and diameter–pressure studies 22

Table 1.2 Qualitative Comparison of Ultrasonic Transducer Families for Continuous, Cuff-Free Blood-Pressure Waveform Monitoring 39

Table 1.3 Performance of Ultrasound-Based Blood-Pressure Waveform Systems (Part 1 of 2)..... 54

Table 1.4 Performance of Ultrasound-Based Blood-Pressure Waveform Systems (Part 2 of 2)..... 55

Table 2.1 CMUT topologies and characterization at 26 V_{pp} 65

Table 3.1 CMUT topologies and characterization at 20 V_{pp} 80

Table 3.2 Pairwise results at a common pull–in–margin operating point, $\hat{V}_{dc} = 0.269$ and $\hat{V}_{pp} = 0.026316$. Values are obtained by linear interpolation at the operating point 81

Table 3.3 Air: raw and normalized $\Delta f/f_0$ sensitivities. Slopes are fit in the raw voltage domain; normalized S^f use V_{PI} (A–D: 40, 160, 106, 260 V) 85

Table 3.4 Vacuum: raw and normalized $\Delta f/f_0$ sensitivities. Slopes are fit in the raw voltage domain; normalized S^f use V_{PI} (A–D: 40, 160, 106, 260 V) 86

Table 3.5 Air: raw and normalized $\Delta Q/Q_0$ sensitivities. Slopes are fit in the raw voltage domain; normalized S^Q use V_{PI} (A–D: 40, 160, 106, 260 V) 86

Table 3.6 Vacuum: raw and normalized $\Delta Q/Q_0$ sensitivities. Slopes are fit in the raw voltage domain; normalized S^Q use V_{PI} (A–D: 40, 160, 106, 260 V) 86

Table 3.7 Summary of CMUT and PMUT characteristics from different studies..... 95

Table 4.1 Comparison of MEMS fabrication strategies relevant to ultrasonic devices.....100

Table 4.2 Temperature windows for materials in the hybrid flow 105

Table 4.3 Chemical compatibility summary (qualitative, based on this work) 106

Table 4.4 Materials used in the hybrid CMUT process 107

Table 4.5 Equipment used for the hybrid CMUT process 107

Table 4.6 Geometric parameters of the hybrid CMUT design 113

LIST OF FIGURES

Page

Figure 1.1 Blood pressure waveform monitoring tree 10

Figure 1.2 Non-invasive BP waveform estimation using a wearable ultrasound probe Taken from author Athaya & Choi (2022)..... 18

Figure 1.3 Local PWV measurement principle Taken from author Xu, Wang, Xia, Wu, Chen, Du, Liu, Xue & Fang (2022) 19

Figure 1.4 Cardiovascular system and major arteries for Blood pressure waveform measurement. (A) Carotid Artery; (B) Radial Artery; (C) Ulnar Artery; (D) Femoral Artery; (E) Renal Artery; (F) Branchial Artery; (G) Abdominal Aorta; (H) Heart..... 23

Figure 1.5 Schematic of a 1-3 piezoelectric composite: ceramic pillars embedded in a polymer matrix..... 25

Figure 1.6 (A) PMUT and (B) CMUT Structures 31

Figure 1.7 Test setup for two-element bulk ultrasound probe Taken from author Seo, Pietrangelo, Lee & Sodini (2015b)..... 40

Figure 1.8 3 element bulk piezoelectric transducer to track arterial wall displacement Taken from author Xu, Wu, Xia, Geng, Lu, Wang, Chen, Li, Du, Liu, Li, Chang & Fang (2023) 41

Figure 1.9 Schematic of measurement configuration for measuring the ulnar artery diameter variations. (a) Measurement by using the ultrasound probe, (b) Measurement by using the flexible sensor Taken from author Peng, Chen, Sim, Zhu & Jiang (2021a)..... 42

Figure 1.10 a) The FAUS is integrated into the wristband and is worn on the arm to measure radial artery blood pressure. b) Schematic diagram of the structure of FAUS. c) FAUS monitors blood pressure waveforms by capturing the pulsating vessel diameter of the radial artery using a pulse-echo method. Taken from author Li, Wang, Luo, Peng, Wang, Liu, Wang & Liu (2023)..... 43

Figure 1.11 Representation of PMUT based device for blood pressure monitoring in ambulatory sheep Taken from author Pen, Pala, Shao, Ding, Xie & Lin (2022) 45

Figure 1.12 Schematic of wearable sensor with a close-up detail of the device construction Taken from author Zhou, Cheng, Qu, Lv, Liu & Xie (2023a) 46

Figure 1.13 (a) SEM image of the fabricated PMUT chip with four arrays. (b) Enlarged view of a single PMUT unit. (c) Cross-sectional view of the PMUT structure via FIB cutting Taken from author Wu, Liu, Wang, Li, Wu, Yang & Li (2023) 47

Figure 1.14 (a) Schematic of the pulse-echo detection signal transfer system. (b) Radial artery monitoring (corresponding to the dashed box in (a)). (c) Customized PCB for PMUT package and size comparison with a coin Taken from author Wu et al. (2023) 48

Figure 1.15 Representation of PMUT based flexible device Taken from author Zhou, Qu, Liu, Wang, Zhang, Zheng & Xie (2025) 51

Figure 1.16 Representation of beam steering of ultrasound pulse by a PMUT based device Taken from author Xia, Peng, Ji, Saini, Wang, Wudaru, Yu, Luo, De Guzman, Wang, Yuan, Chien & Lin (2025)..... 52

Figure 2.1 CMUT dimensions and design features..... 65

Figure 2.2 (A) Fabricated cell of CMUT A & B. (B) Fabricated cell of CMUT C & D. 66

Figure 2.3 Vibrometer test setup 68

Figure 2.4 Acceleration PSDs of CMUTs vs Frequency: (a) CMUT A (i) different bias voltages (20 V_{pp}); (ii) different signal amplitudes (26 V_{dc}), (b) CMUT B (i) different bias voltages (20 V_{pp}); (ii) different signal amplitudes (70 V_{dc}), (c) CMUT C (i) different bias voltages (20 V_{pp}); (ii) different signal amplitudes (70 V_{dc}), (d) CMUT D (i) different bias voltages (20 V_{pp}); (ii) different signal amplitudes (70 V_{dc}), and (e) Acceleration PSD of CMUTs B, C, and D at 30 V_{dc} and 20 V_{pp}, and CMUT A at 26 V_{dc} and 20 V_{pp} 71
(a) CMUT A..... 71
(b) CMUT B..... 71
(c) CMUT C..... 71
(d) CMUT D..... 71
(e) All CMUTs 71

Figure 3.1 Normalized DC bias range $\hat{V}_{dc}$ for CMUTs A–D. Solid horizontal bars indicate the accessible $\hat{V}_{dc}$ interval per device, open circles

mark all evaluated operating points, and the vertical dashed line denotes the selected common $\hat{V}_{dc}$ used for cross-device 78

Figure 3.2 Acceleration PSDs of CMUTs vs. frequency in air: (a) CMUT A: (i) different bias voltages at 20 V_{pp}; (ii) different drive amplitudes at 26 V_{dc}; (b) CMUT B: (i) different bias voltages at 20 V_{pp}; (ii) different drive amplitudes at 70 V_{dc}; (c) CMUT C: (i) different bias voltages at 20 V_{pp}; (ii) different drive amplitudes at 70 V_{dc}; (d) CMUT D: (i) different bias voltages at 20 V_{pp}; (ii) different drive amplitudes at 70 V_{dc}; (e) comparison of CMUTs at a common operating condition (CMUT B, C, D at 30 V_{dc}, 20 V_{pp}; CMUT A at 26 V_{dc}, 20 V_{pp}) 82
(a) CMUT A 82
(b) CMUT B 82
(c) CMUT C 82
(d) CMUT D 82
(e) All CMUTs 82

Figure 3.3 Acceleration PSDs of CMUTs vs. frequency in vacuum: (a)–(d) CMUTs A–D under (i) dc-bias sweeps at fixed 1 V_{pp} and (ii) drive sweeps at fixed 10 V_{dc}; (e) comparison of CMUTs A–D at 10 V_{dc} and 1 V_{pp} 83
(a) CMUT A 83
(b) CMUT B 83
(c) CMUT C 83
(d) CMUT D 83
(e) All CMUTs 83

Figure 3.4 Bias- and drive-induced changes in (a,b) quality factor and (c,d) resonant frequency for CMUTs A–D in air and vacuum. Dashed lines are least-squares fits used to extract the sensitivities reported in Tables 3.3–3.4 and 3.5–3.6 87
(a) Relative change in Q-factor in air 87
(b) Relative change in Q-factor in vacuum 87
(c) Relative change in resonant frequency in air 87
(d) Relative change in resonant frequency in vacuum 87

Figure 4.1 Schematic cross-section and plan view of the hybrid CMUT cell 111

Figure 4.2 Optical microscope image of fabricated hybrid CMUT cell, bottom aluminum electrode, printed silver top electrodes, and etch-hole pattern 113

Figure 4.3 Acceleration PSD of a single hybrid CMUT cell in air at 3 V dc bias and 8 V_{pp} ac drive, showing two clear mechanical resonance around 1 MHz and 1.41 MHz.....115

LIST OF ABREVIATIONS

Al	Aluminium
Ag	Silver
AlN	Aluminium nitride
BP	Blood pressure
CMUT	Capacitive micromachined ultrasonic transducer
COTS	Commercial off-the-shelf
CNN	Convolutional neural network
DBP	Diastolic blood pressure
DI	Deionized (water)
FAUS	Fabric-based ultrasonic sensor
IC	Integrated circuit
IPA	Isopropyl alcohol
LDV	Laser Doppler vibrometer
LOR	Lift-off resist
MAP	Mean arterial pressure
MEMS	Microelectromechanical systems
MRayl	Mega Rayl (unit of acoustic impedance)
NDT	Non-destructive testing
NMP	N-methyl-2-pyrrolidone

PCB	Printed circuit board
PDMS	Polydimethylsiloxane
PMUT	Piezoelectric micromachined ultrasonic transducer
PSD	Power spectral density
PTT	Pulse transit time
PZT	Lead zirconate titanate (piezoelectric ceramic)
PWV	Pulse wave velocity
QA	Flow–area method for PWV estimation
SBP	Systolic blood pressure
SEM	Scanning electron microscope
SOI	Silicon-on-insulator
SU-8	Negative epoxy-based photoresist
UQAM	Université du Québec à Montréal
UQAC	Université du Québec à Chicoutimi
AZ 5214E	Image reversal photoresist (AZ 5214E)

LIST OF SYMBOLS AND UNITS OF MEASUREMENTS

A	Cross-sectional area of the vessel
A_{plate}	Active plate area
c	Speed of sound in the propagation medium
D	Membrane (cell) diameter
d_h	Etch-hole diameter in SU-8 membrane
E	Young's modulus (when used in mechanical models)
f_{res}	Resonant frequency
g	Electrostatic gap height (cavity thickness)
k_{eff}	Effective stiffness of the CMUT plate
L_{bot}	Length of bottom electrode
L_{top}	Length of top electrode
MAP	Mean arterial pressure
M_{total}	Effective modal mass of the vibrating plate
N_x	Number of cells along x
N_y	Number of cells along y
P	Blood pressure
P_{dia}	Diastolic blood pressure
P_{sys}	Systolic blood pressure
PWV	Pulse wave velocity

p_h	Pitch between etch holes
p_x	Cell pitch in the x-direction
p_y	Cell pitch in the y-direction
Q	Mechanical quality factor of the CMUT mode
Q_v	Volumetric flow rate
t_{Ag}	Printed silver top-electrode thickness
t_{Al}	Sputtered aluminium bottom-electrode thickness
t_{LOR}	LOR sacrificial-layer thickness
t_{SU8}	SU-8 membrane thickness
V_{dc}	DC bias voltage applied between CMUT electrodes
V_{PI}	Pull-in (collapse) voltage of the CMUT membrane
V_{pp}	Peak-to-peak AC drive voltage
W_{bot}	Width of bottom electrode
W_{top}	Width of top electrode
Z_{c}	Characteristic impedance of the vessel
β	Exponential stiffness index in BP–diameter model
Δf	-3 dB bandwidth
ν	Poisson's ratio (when used in mechanical models)
ρ	Density of blood

INTRODUCTION

Context of study and the problems

Cardiovascular disease remains one of the leading causes of mortality worldwide and imposes a substantial burden on healthcare systems. Early detection and continuous monitoring of hemodynamic parameters, in particular the arterial blood pressure (BP) waveform is critical for prevention, risk stratification, and therapy guidance. Yet, most widely used clinical tools such as oscillometric cuffs or catheter-based measurements are either intermittent, bulky, operator-dependent, or invasive. They do not provide comfortable, beat-to-beat tracking of the BP waveform in daily life.

In parallel, the rapid maturation of microfabrication technologies and the growing ecosystem of wearable and portable devices are transforming what is technically possible for physiological monitoring. There is a strong demand for ultra-thin, low-power, skin-conformal sensors capable of continuously probing arterial mechanics without constraining the user. Among the existing technologies, ultrasonic sensing is particularly attractive: it is safe, directional, depth-resolved, and inherently sensitive to arterial wall motion and pulse wave propagation.

Micromachined ultrasonic transducers (MUTs), and especially capacitive MUTs (CMUTs), offer a promising pathway toward such wearable systems. CMUTs combine: (i) broadband operation suitable for resolving detailed pressure waveforms; (ii) fine lateral and vertical scaling compatible with dense arrays; and (iii) potential monolithic integration with readout electronics. However, three key challenges currently limit their deployment in flexible, wearable BP monitoring:

- **Bias voltage:** Conventional CMUTs often require tens to hundreds of volts of dc bias to achieve sufficient electromechanical coupling, which complicates power delivery, raises safety and EMC concerns, and is poorly suited to battery-powered, on-body devices.

- **Quality factor and bandwidth:** Many CMUT designs exhibit high mechanical quality factor (Q), leading to narrow bandwidth and long ringdown. For time-domain sensing of arterial waveforms, a controlled and, in many cases, reduced effective Q is desirable to shorten pulses and enable broadband operation without sacrificing sensitivity.

- **Fabrication platform:** Most CMUT processes are realized on rigid silicon using complex, high-temperature, multi-mask surface micromachining or wafer bonding flows. These routes are costly, slow to iterate, and not directly compatible with flexible substrates or large-scale, low-cost manufacturing.

This thesis addresses these three challenges within a unified objective: to explore and develop CMUT architectures, analysis methods, and fabrication strategies that move toward low-bias, broadband, and potentially flexible ultrasonic transducers suitable for continuous, non-invasive blood pressure waveform monitoring.

Objectives of the research

The overarching goal is to support the realization of CMUT-based wearable BP monitoring systems by advancing four tightly connected aspects:

1. **Understand and frame the application requirements.** Quantify what continuous BP waveform monitoring demands from an ultrasonic front-end in terms of frequency range, bandwidth, coupling, form factor, and power consumption.

2. **Engineer CMUT structures with reduced bias and tailored Q.** Investigate CMUT topologies that can operate at lower dc bias while providing sufficiently low or controllable Q for high-resolution, broadband sensing.

3. **Develop robust methods to decompose and compare damping mechanisms.** Establish a framework to experimentally separate intrinsic, anchoring, fluidic, and loading-related losses, enabling rational CMUT design for specific pulse-echo and sensing scenarios.

4. **Explore hybrid fabrication routes compatible with flexible, low-cost platforms.** Design and demonstrate a CMUT process that combines conventional micromachining with additive printing to reduce complexity and enable direct fabrication on non-traditional substrates suited for wearables.

These objectives are reflected in the main contributions of the thesis.

Main contributions

The original contributions of this work, viewed through the lens of the above objectives, are:

1. **Comprehensive review of ultrasonic approaches for non-invasive BP waveform monitoring.** A critical survey of state-of-the-art CMUT, PMUT, and bulk-transducer-based strategies, identifying performance gaps, calibration challenges, and design targets for future wearable systems.

2. **Low-Q, low-bias CMUT architectures for portable imaging and sensing.** Design, simulation, and experimental validation of CMUT structures that achieve significantly reduced Q and lower operating voltages, improving suitability for portable and high-resolution applications relevant to BP monitoring.

3. **Experimental demonstration that anchoring and geometry control nonlinearity, Q, and actuation voltage.** A systematic comparative study showing how support conditions and structural design shape the type of nonlinearity, quality factor, and bias requirements, providing practical design rules for application-specific CMUTs.

4. **Quantitative Q-factor decomposition methodology.** Development and application of an experimental framework to decompose measured Q into intrinsic and fluidic components across CMUT topologies and environments, enabling fair comparison and targeted damping engineering.

5. **Hybrid CMUT fabrication process concept and proof-of-principle implementation.** Proposal and demonstration of a CMUT process that combines sputtered thin films, micromachined cavities, and printed conductors. This hybrid route reduces layer complexity, shortens turnaround time, and is, in principle, extendable to flexible substrates for wearable BP monitoring patches.

Together, these contributions advance both the understanding of how CMUTs should be designed for continuous BP sensing and the practical means by which such devices can be fabricated and evaluated.

Structure of the thesis

The thesis is organized to follow this logic from fundamentals to implementation:

- **Chapter 1:** Provides a focused review of ultrasound-based blood pressure monitoring, with emphasis on CMUT and PMUT implementations, signal processing strategies, and calibration challenges. It consolidates the system-level constraints that a practical CMUT-based BP device must satisfy and positions the designs of Chapters 2, 4, and 5 within that landscape.

- **Chapter 2:** Presents the design, fabrication, and characterization of CMUT structures engineered for low bias and controlled low Q suitable for high-resolution, portable medical imaging and sensing. This chapter demonstrates that CMUT behavior can be tuned through geometry and support to better match wearable BP monitoring requirements.

- **Chapter 3:** Extends the experimental CMUT study to a detailed analysis of damping and quality factor. Using measurements in air and vacuum, it applies a Q-factor decomposition framework to separate intrinsic and fluidic losses and to compare different designs on a common basis. This chapter translates empirical observations into actionable guidelines for engineering Q in CMUTs intended for broadband, low-voltage operation.

- **Chapter 4:** Proposes and demonstrates a hybrid CMUT fabrication process that combines surface micromachining with additive printing of conductive layers. The chapter details the process integration constraints, presents a proof-of-principle device, and discusses how the approach can be extended to flexible substrates and large-area arrays suitable for wearable BP monitoring.

This structure ensures that each component device physics, design strategies, loss decomposition, and fabrication is explicitly connected to the overarching goal of enabling CMUT-based, low-bias, high-resolution, and ultimately wearable blood pressure waveform monitoring systems.

CHAPTER 1

REVIEW ON DEVELOPMENT OF ULTRASONIC BASED SENSORS FOR NON-INVASIVE BLOOD PRESSURE WAVEFORM MONITORING

1.1 Introduction

Cardiovascular diseases (CVDs) are those that affect the normal functioning of the heart or blood vessels. CVDs are also one of the leading causes of global mortality, with 17 million deaths in 2019 accounting for 32% of global deaths, of which 85% were specifically related to heart attack or stroke (Wor (2021)). CVDs include conditions such as coronary artery disease, stroke, heart failure, and peripheral artery disease. These diseases disrupt the normal functioning of the cardiovascular system, which is responsible for delivering oxygen and nutrients to various parts of the body. Critical CVDs are related to blood flow to the heart and brain as these are critical organs. A World Health Organization report stated that of the 17.3 million deaths in 2008, 7.3 million were due to coronary heart disease and 6.2 million were due to stroke (Shrivastava, Singh, Raizada & Singh (2015)).

Coronary heart disease is caused by a lack of blood supply to the heart muscle through the arteries, whereas stroke is caused by a lack of blood flow to the brain. High blood pressure (hypertension), high cholesterol, smoking, obesity, diabetes, and a sedentary lifestyle are just a few of the variables that can contribute to CVD. Hypertension is the most significant modifiable risk factor, accounting for 9.4 million deaths yearly, with stroke accounting for 51% of deaths and coronary heart disease for 45%. This figure is expected to increase in the coming years as the population ages (Forouzanfar & Alexander (2015)). Despite these facts, only 33% of hypertension individuals are aware of their disease and control their blood pressure by obtaining relevant treatments (Chow, Teo, Rangarajan, Islam, Gupta, Avezum, Bahonar, Chifamba, Dagenais, Diaz, Kazmi, Lanas, Wei, Lopez-Jaramillo, Fanghong, Ismail, Puoane, Rosengren, Szuba, Temizhan, Wielgosz, Yusuf, Yusufali, McKee, Liu, Mony & Yusuf (2013)).

By 2030, approximately 23.6 million people are expected to lose their lives due to CVD, mainly attributed to heart disease and stroke, which will become the leading causes of death worldwide. Furthermore, the prevalence of CVDs among younger adults 40 years and older is expected to increase in the coming years (Nag & Ghosh (2013)).

It is established that CVDs are of global health concern. According to a report released by the European Society of Cardiology, there is a clear and consistent relationship between blood pressure levels and the risk of hypertension. This suggests that blood pressure is a crucial indicator when assessing the risk of CVDs. In addition to other diagnostic tools such as electrocardiograms (ECG) and echocardiograms, arterial blood pressure (ABP) plays an important role in the diagnosis and prediction of CVD outcomes. Therefore, monitoring and managing blood pressure is essential.

However, traditional methods of measuring blood pressure, such as auscultatory or oscillometric measurements, have limitations. These methods are intrusive and provide measurements at specific time intervals. Consequently, they may not capture the patient's physiological condition in a timely manner and vital signals could be missed. This is particularly problematic because certain risk patterns may be invisible when the patient is at rest and manifest only sporadically during periods of stress on the circulatory system (Zhao, Liang, Huang, Zhou, Xiao, Ji, Zhang & Zhao (2023)).

Another limitation is that these methods only provide systolic and diastolic pressure while not taking into account the complete arterial pressure waveform, thus limiting their capacity to capture beat-to-beat fluctuations and complex hemodynamic parameters. This limitation is particularly significant in clinical research and practice because continuous waveform data provide critical insights into cardiovascular function, such as pulse pressure variation and rate of pressure change, that are valuable for detecting arrhythmias, reflecting arterial elasticity, compliance, and cardiac performance (Bayda, Adeel, Tuccinardi, Cordani & Rizzolio (2019)).

A reliable continuous monitoring system of the blood pressure waveform would significantly improve the rate of awareness, treatment, and control of hypertension, considering the preventable nature of the condition and its importance in healthcare strategies in ambulatory settings.

By providing continuous monitoring, such a system would offer several advantages over traditional intermittent measurement methods. Firstly, it would enable healthcare professionals to capture a more comprehensive picture of BP patterns in a patient, including variations throughout the day and in response to different activities or stressors. This would provide a more accurate assessment of the patient's overall BP profile and would aid in diagnosing and managing hypertension.

Furthermore, continuous monitoring would increase the patient's awareness of their blood pressure fluctuations and patterns, promoting self-management and proactive participation in their healthcare. Patients would have access to real-time information about their blood pressure, allowing them to make lifestyle modifications or seek medical attention promptly when necessary. This empowerment could lead to better adherence to treatment plans and better long-term blood pressure control (Rastegar, GholamHosseini & Lowe (2019)).

Currently, the gold standard for measuring the blood pressure waveform is arterial catheterization. This invasive procedure involves inserting a thin catheter into arteries such as the radial, brachial, or femoral artery. Although highly accurate, arterial catheterization poses significant risks, including infections, hematoma formation, vessel damage, and blood loss, and requires specialized skill, making it unsuitable for routine monitoring and long-term applications (Nguyen & Bora (2023)). Thus, there is a critical need for reliable, continuous, and non-invasive alternatives capable of capturing dynamic BP waveforms safely, conveniently, and over prolonged durations.

In response, non-invasive sensor technologies, particularly ultrasonic sensors, have garnered significant attention. Ultrasonic sensors function by transmitting acoustic waves through biological tissues, capturing reflections from arterial walls, and translating these signals into accurate and continuous measurements of arterial dynamics (Brown, Sharma, Leadbetter,

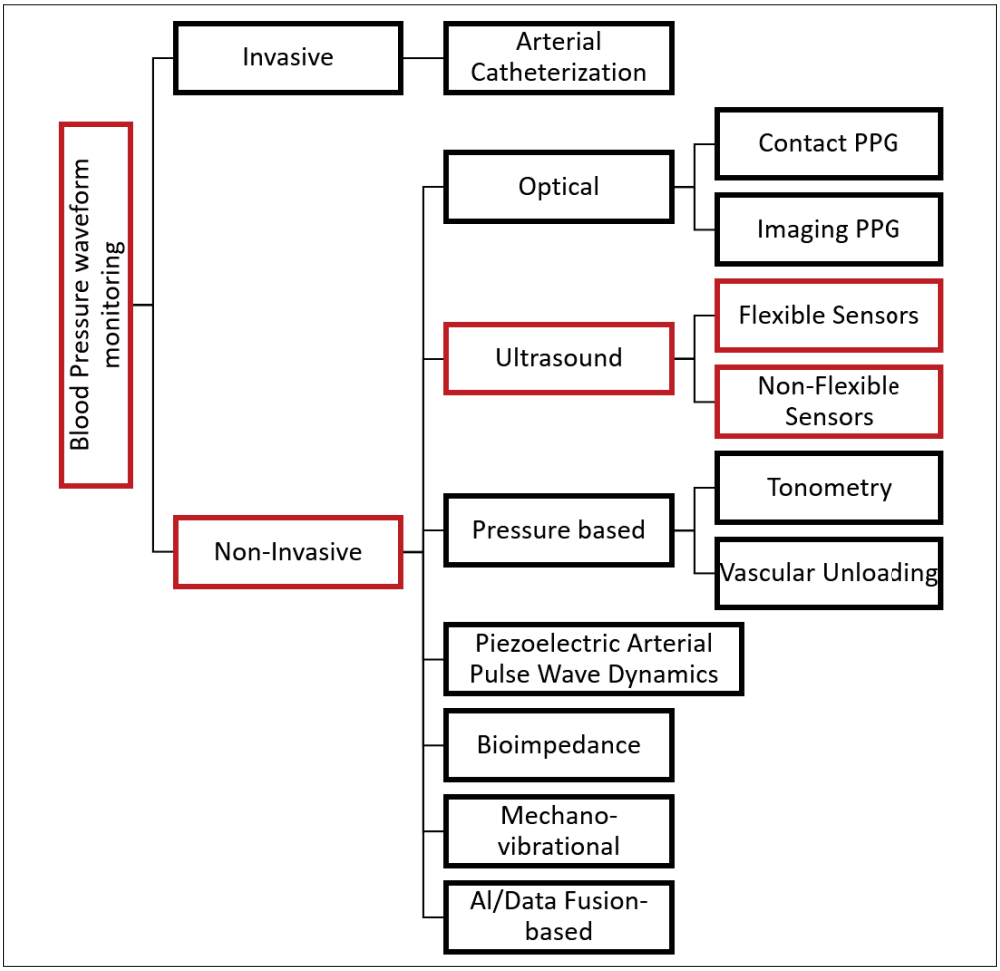

Figure 1.1 Blood pressure waveform monitoring tree

Cochran & Adamson (2014); Cochran (2012); Shung & Zipparo (1996)). Compared to traditional cuff-based methods, ultrasonic sensors have the distinct advantages of measuring central blood pressure waveforms directly and continuously, providing deeper insights into cardiovascular health parameters such as arterial stiffness and cardiac output variability (Zhu, Liu, Shi, He, Sun, Guo, Liu, Sulaiman, Dong & Lee (2019)). Furthermore, the integration of these sensors with microelectromechanical systems (MEMS) technology enables device miniaturization, lower power consumption, and wireless connectivity, significantly improving portability and convenience for clinical and ambulatory use (Mallegni, Molinari, Ricci, Lazzeri, La Rosa, Crivello & Milazzo (2022); Pattanaik & Ojha (2023)).

However, for practical clinical and ambulatory settings, ultrasonic sensors must not only be miniaturized and energy-efficient but also flexible and conformal. Flexibility ensures a close and stable contact between the sensor and the skin surface, improving acoustic coupling and measurement accuracy (Przybyla, Shelton, Guedes, Izyumin, Kline, Horsley & Boser (2011)). Conformability is essential to comfortably accommodate various anatomical locations, maintain consistent sensor positioning during patient movement, and promote patient adherence, especially in long-term monitoring scenarios. Therefore, recent advances have increasingly focused on the development of MEMS-based ultrasonic sensors that utilize flexible substrates and innovative fabrication techniques, thus promising significant improvements in comfort, measurement fidelity, and practical clinical applicability (Li, Lin, Li, Yang, Liu, Jiang, Zhang & Wang (2022a); Xu et al. (2023); Yi, Liu, Li, Ruan, Chen, Liu, Yang, Zhang, Yi, Li, Zhang, Liu, Ruan, Chen, Liu & Yang (2022)).

Ultrasonic transducers generate acoustic pressure waves using different mechanisms such as piezoelectric and electrostatic. In piezoelectric transducers, certain materials (e.g., quartz, PZT) convert mechanical strain into electric charge and vice versa. By applying an alternating voltage at the resonance frequency of the material, the piezoelectric element oscillates and emits ultrasonic waves into the surrounding medium (José Horst, Paulo Andrade Junior, De Almeida Vieira, Paulo de Andrade Junior, Adriano Duvoisin & de Almeida Vieira (2020); Kenawy & Khalil (2020); Qin, Xia, Rogers, Jackman, Zhao & Whitesides (1998)). This mechanism enables both generation and detection of ultrasound signals. Electrostatic transducers employ a thin membrane and a fixed electrode, separated by a small gap. When an alternating voltage is applied, electrostatic forces periodically move the membrane, creating ultrasonic vibrations. As the membrane oscillates, it radiates or detects acoustic waves, acting as a transmitter and receiver of ultrasound (Shanbhag & Patil (2017); Teh (2017)).

Transducers can be fabricated using MEMS technology and traditional methods. Traditional transducers, such as bulk piezoelectric devices, rely on thick ceramic layers that vibrate in the thickness mode but face challenges in miniaturization, array pitch, and power consumption. In contrast, micromachining and MEMS methods have given rise to micromachined ultrasonic

transducers (MUTs), which include piezoelectric micromachined ultrasonic transducers (PMUTs) and capacitive micromachined ultrasonic transducers (CMUTs). These devices operate using electrostatic forces where the membrane moves in the air gap fabricated in the device (Badry, Ibrahim, Gamal, Shehata, Ezzat & Elhaes (2020); Kim & Meng (2015); Prabakar, Killivalavan, Sivakumar, Chandra Babu Naidu, Sathyaseelan, Senthilnathan, Baskaran, Manikandan, Rao, Sarma & Ratnamala (2020); Shanbhag & Patil (2017); Teh (2017); Zorman & Mehregany (2004)). They offer advantages such as smaller feature sizes, batch fabrication, and easier integration with complementary metal–oxide–semiconductor (CMOS) electronics. Researchers are also exploring flexible substrates (e.g., polyimides) to facilitate conformal, wearable sensors suitable for continuous physiological monitoring (Yao & Peddi (2016)).

However, despite the growing attention to ultrasonic solutions for continuous blood pressure monitoring, much of the current literature still centers on bulk piezoelectric transducers and PMUT-based designs. Research on CMUTs within this specific application remains comparatively limited, leaving a significant gap in understanding how CMUTs could be optimized for non-invasive arterial pressure waveform measurement (Kim & Meng (2015)).

Figure 1.1 provides a roadmap of existing technologies for the continuous monitoring of blood pressure waveforms. While the left branch denotes the invasive gold standard (arterial catheterization), the right side spans the full suite of non-invasive approaches: vascular unloading based on the cuff, tonometry, optical / PPG, acoustic / ultrasound, mechano-vibrational and bioimpedance methods. In this review, we focus exclusively on the **ultrasonic** branch.

By critically examining the existing literature, we aim to investigate the underlying design principles, fabrication techniques, and performance characteristics of these sensors. In addition, we will analyze the challenges and opportunities associated with their implementation in clinical settings.

In the following sections, we begin with an overview of the core working principles of ultrasound sensors for BP waveform monitoring in section 1.2. Transducer characteristics are discussed for high resolution imaging. Then, We cover different models used to calculate the blood pressure

signal from dynamic artery displacement. Next, in section 1.3, we explain the basic concepts and fabrication processes of bulk, piezoelectric and capacitive micromachined ultrasonic transducers. Finally in the section 1.4, we take a close look at the state of the art and the technological evolution of ultrasound sensors for BP waveform monitoring from bulk transducers to PMUTs and CMUTs, we then discuss their limitations before delving into future directions in section 1.5.

1.2 Ultrasound Principles for Blood-Pressure Sensing

1.2.1 Core Working Principle

Ultrasonic blood-pressure waveform monitoring most commonly employs a pulse-echo approach. A transducer emits brief, high-frequency ultrasound pulses (typically 5–10 MHz) toward a superficial artery and then records the echoes returning from the near and far walls. By measuring the time-of-flight difference $\Delta\mathrm{TOF}(t)$ between these reflections, the instantaneous arterial diameter

$$D(t) = \frac{c\,\Delta\mathrm{TOF}(t)}{2} \tag{1.1}$$

(where $c \approx 1540$ m/s is the speed of sound in soft tissue) can be determined at kilohertz sampling rates, yielding upto sub-micrometre axial and sub-millisecond temporal resolution of diameter fluctuations (Seo et al. (2015b)). These diameter waveforms are then converted into calibrated pressure waveforms $P(t)$ using different models (Section 1.2.4) or invasive measurement for absolute scaling (Bayda et al. (2019)). Because this purely acoustic, non-occlusive method directly tracks central arteries and can be implemented on flexible, conformal MEMS arrays, it enables continuous, cuff-free monitoring of beat-to-beat blood-pressure waveforms.

1.2.2 Depth of penetration and lateral resolution

Depth of penetration (DoP) refers to the furthest distance along the beam axis at which echo signals can still be detected by the receiver transducer. As an ultrasonic wave travels through

biological media, its energy diminishes for two main reasons. First, the beam spreads out in three dimensions, so its intensity falls with the inverse square of the distance from the source. Second, the mechanical oscillations of the wave are partly converted into heat—an absorption process whose coefficient increases approximately with the square of the insonation frequency (Kremkau & Taylor (1986); Wear (2011)). In soft tissues this frequency-dependent loss typically lies between 0.3 and 1.1 dB $MHz^{-1}cm^{-1}$ and rises toward the upper end of that range in more fibrous or mineralised organs (Goss, Johnston & Dunn (1978)). Because attenuation grows rapidly with frequency, high-frequency pulses lose energy faster and therefore cannot probe as deeply. Once the combined geometric and absorptive losses push the echo signal below the receiver noise, the returning wavefront is effectively invisible to the transducer. Since ultrasound devices are generally operated at their resonant frequency, clinicians select low-frequency probes when imaging deeply situated structures such as the adult heart, and reserve higher-frequency arrays for superficial targets like the radial or brachial artery (Li & Wang (2021); Parker (2022)).

Lateral resolution tells us how closely two side-by-side reflectors can sit before they blur into one on an ultrasound image. It depends mainly on the probe's active width (aperture) and how tightly the beam is focused, captured by the f-number

$$F\# = \frac{\text{focus depth}}{\text{aperture width}}. \tag{1.2}$$

Near the focus, the beam width—and therefore the smallest resolvable gap—is approximately

$$\Delta x \;\approx\; 1.02\,\lambda\,F\#, \tag{1.3}$$

where λ is the ultrasound wavelength in tissue (Ploquin, Basarab & Kouamé (2015)). Beam geometry in a wearable BP probe is governed by two hardware levers. The aperture width D equals the total active area of the transducer: in single-element devices it is fixed by the crystal or CMUT/PMUT die diameter, whereas in linear or matrix arrays the beamformer can widen or narrow D by activating more or fewer elements, trading probe footprint for lateral sharpness (Wang, Li, Hu, Zhang, Huang, Lin, Zhang, Yin, Huang, Gong, Bhaskaran, Gu, Makihata, Guo,

Lei, Chen, Wang, Li, Zhang, Chen, Pisano, Zhang, Zhou & Xu (2018)). The focus depth z_f the point where the beam is narrowest—is established either passively with a curved acoustic lens bonded to the transducer face or actively with phased-array time delays that converge the wavefront at a selectable depth and can be updated dynamically as echoes return (Hu, Huang, Li et al. (2023)).

A low f-number(wide aperture or strong focusing) gives a thin beam and sharp detail but a shallow in-focus zone and higher side-lobes. A high f-number produces a wider beam with lower detail yet a deeper focal region. Probe designers therefore favour low f-numbers for superficial targets such as small arteries, and higher f-numbers for deeper organs to keep the beam effective over a longer path.

1.2.3 Bandwidth and axial resolution

Axial resolution is the minimum spacing along the beam's path (the transducer's axis) at which two reflectors can still be distinguished as separate echoes. Enhancing this resolution allows finer tracking of subtle arterial-diameter variations, thereby improving the accuracy of the reconstructed blood-pressure waveform. Depth of penetration (DoP) is dictated by the transducer's resonant—frequency, whereas axial resolution is governed by the response's spectral width, i.e., its bandwidth, as quantified in the following relationship given by eq. 1.4 (Cootney & Coatney (2001); Ng & Swanevelder (2011))

$$\Delta z \approx \frac{c}{2\,\Delta f}, \tag{1.4}$$

where Δf is absolute –6 dB bandwidth (Hz), there exists a frequency dependence on the axial resolution as the bandwidth is a function of resonant frequency and the fractional bandwidth (BW_{frac}) is given by eq 1.5, where f_0 is the resonant frequency,

$$BW_{frac} = \frac{\Delta f}{f_0} \tag{1.5}$$

therefore, 2 devices with same fractional bandwidth but different resonant frequency will have different axial resolution. This leads to the classic trade-off between resolution and penetration: raising the resonant frequency shortens the wavelength and sharpens both axial and lateral detail, yet the accompanying increase in attenuation confines useful imaging to progressively shallower (Foiret, Cai, Bendjador, Park, Kamaya & Ferrara (2022)).

Conventional bulk PZT transducers typically exhibit relatively narrow fractional bandwidths—often on the order of 50–70% at -6 dB—due to their high mechanical quality factor and the need for multiple acoustic-matching layers to bridge the impedance mismatch with soft tissue (Gerardo, Cretu & Rohling (2018); Li et al. (2008)). In contrast, CMUTs behave like near-ideal broadband pistons: their thin silicon membranes couple efficiently to the medium, routinely achieving fractional bandwidths of 100–120 % around 1–5 MHz and enabling sub-cycle pulse generation for transform-limited axial resolution (Gerardo et al. (2018); Wang, Ma, Yang, Jiang, Ding & Xie (2020); Wang, He, Zhang, Li, Gao, Meng, Zhang, Yang, Wang, Cui, Wang, Zhang, Ren, Zhen, Jiao & Zhang (2022)). PMUTs occupy an intermediate position: early AlN-based flexural designs were limited to 40–60 % bandwidth, but more recent PZT and mass-loaded AlN implementations have pushed PMUT fractional bandwidths into the 80–110 % range at resonant frequencies between 3 and 8 MHz (Ruan, Wang, Hu, Li, Xu, Liu, Yang & Liu (2025); Zhao, Xia, Yang & Lu (2024)). This progression of bandwidth (bulk PZT « PMUT < CMUT) highlights CMUTs as the prime choice for ultra-broadband imaging, while optimized PMUTs offer a compelling compromise between MEMS scalability and ultrasound performance.

Hence, a rational probe-design workflow is as follows :

1. Select the lowest resonant frequency that still gives the desired lateral (wavelength limited) resolution and target depth.

2. Push fractional bandwidth as high as the transducer physics allows to bring axial resolution to the transform limit while preserving the penetration depth already secured.

1.2.4 Models Relating Artery Diameter to BP

Several BP models for non-invasive ultrasound based measurements discussed by researchers in previous works (Goncalves Seabra, Silva, Stieglitz & Amado-Rey (2022)). These include, Linear relationship, Exponential relationship, laplace's Law + MK equation, Bramwell-Hill equation and Joukowsky's equation + PWV. It should be noted that these equations require an initial calibration using a BP cuff. The BP cuff measures the diastolic blood pressure (DBP) and systolic blood pressure (SBP). This is correlated with mean arterial pressure (MAP) by $MAP = 0.42 \times SBP + 0.58 \times DBP$ (Papaioannou, Protogerou, Vrachatis, Konstantonis, Aissopou, Argyris, Nasothimiou, Gialafos, Karamanou, Tousoulis & Sfikakis (2016)). DBP and MAP do not change significantly through the arterial tree. Pulse pressure is defined by $DBP - SBP$, and it changes significantly through the artery tree .

1.2.4.1 Arterial wall tracking

The non-invasive BP measurement using wall tracking is represented by Fig. 1.2 (Athaya & Choi (2022)). The process starts with design and fabrication of ultrasound device array based on specific parameters like resonant frequency, acoustic attenuation, sensitivity and arterial site. Then, the device is placed on the arterial site for measurement. An ultrasound pulse is emitted from the device, the pulse travels through the tissue until it hits the artery anterior wall. A part of the pulse is reflected, and the rest continues traveling till it hits the posterior wall. Again, a part of it is reflected and rest continues and dissipates in the tissue. The reflected pulses travel back to the device and create an output signal of the diameter of the arterial wall. This output signal is processed and input to the mathematical equation described below to get the BP waveform.

- **Linear Relationship** - Artery diameter waveform can be directly translated to blood pressure waveform using linear relationship. The relationship requires an estimate of brachial DBP and MAP for initial calibration. Diastolic and mean arterial diameter are also required and measured with the ultrasound transducer. Equation given by Eq. 1.6 equates blood pressure waveform with diameter waveform.

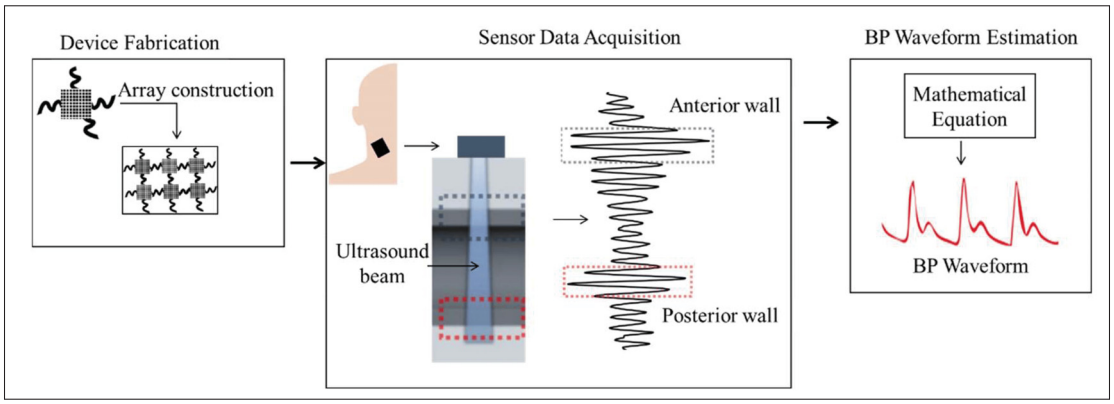

Figure 1.2 Non-invasive BP waveform estimation using a wearable ultrasound probe
Taken from author Athaya & Choi (2022)

$$P(t) = D(t) \cdot k + b \tag{1.6}$$

P(t) is instantaneous pressure, D(t) is diameter waveform, k is the slope calculated by calibration, and b is the intercept at diastolic pressure. The equation given by Eq. 1.7 gives slope where $\bar{D(t)}$ is the mean arterial diameter (Sun (2013)).

$$k = \frac{MAP - DBP}{\bar{D}(t) - D_d} \tag{1.7}$$

It was noted that the linear relation was only valid for more elastic arteries like carotid artery, whereas for peripheral arteries like radial artery, the diameter pressure relation shows an exponential relation (Hoeks (1993); Meinders & Hoeks (2004)).

- **Exponential Relationship** - Exponential relation between blood pressure waveform and artery area waveform is given by eq. 1.8.

$$P(t) = P_0 \cdot e^{\beta\left(\frac{A(t)}{A_d} - 1\right)} \tag{1.8}$$

The relationship requires an initial calibration by calculating SBP and DBP using a commercial BP cuff as well as measuring diameter at SBP and DBP using ultrasound sensor. Calibration factor is given by Eq. 1.9 (Giudici, Palombo, Morizzo, Kozakova, Cruickshank, Wilkinson & Khir (2021)). In the given equations, P_0 and P_d is initial diastolic BP, A(t) is artery area waveform, A_d is artery area at DBP, A_s is artery area at SBP and P_s is initial systolic BP. β is the artery stiffness index. For improved accuracy of β calculation, SBP, DBP and D(t) should be measured at the same site (Gavish & Izzo (2016); Kachuee, Kiani, Mohammadzade & Shabany (2017); Wang et al. (2018)).

$$\beta = \frac{A_d \cdot \ln\left(P_s/P_d\right)}{A_s - A_d} \tag{1.9}$$

1.2.4.2 Pulse transit time (PTT) and Pulse wave velocity (PWV)

PWV is defined as the stiffness of the artery and is measured by calculating the speed of a pressure pulse wave between two sites with known distance along the artery as shown in Fig. 1.3 (Xu et al. (2022)). The time it takes the pressure wave to go from the upstream pressure catheter to the downstream pressure catheter provides the PTT (Zhao et al. (2023); Zhou, Cui, Li, Jian, Li, Ji, Li, Xu, Liu, Yang, Zhou, Cui, Li, Jian, Li, Ji, Li, Xu, Liu, Yang & Ren (2023b)).

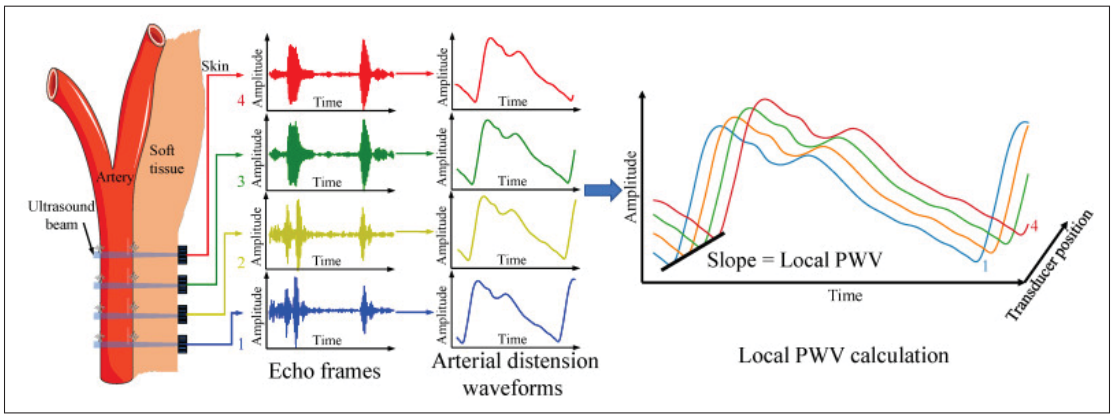

Figure 1.3 Local PWV measurement principle
Taken from author Xu et al. (2022)

- **Laplace's Law + MK equation** - This model requires local PWV to be calculated at the site of artery diameter waveform estimation. The relation of PWV with the artery radius is given by eq. 1.10. In this model, PWV is dependent on artery elasticity and artery wall thickness. E is the Young's elastic modulus of the arterial wall, h is the wall thickness, R is the artery's luminal radius (Vappou, Luo, Okajima, Di Tullio & Konofagou (2011)). This local PWV is further translated to arterial pulse pressure by eq. 1.11 where R(t) is arterial radius waveform, R_0 is radius at DBP and ρ is blood density. The real time blood pressure waveform is related to the arterial pressure difference by eq. 1.12 where P_o is the diastolic blood pressure.

$$PWV = \sqrt{\frac{E \cdot h}{2\rho \cdot R}} \tag{1.10}$$

$$\Delta P = 2\rho \cdot PWV^2 \cdot \log\left(\frac{R(t)}{R_0}\right) \tag{1.11}$$

$$\Delta P = P(t) - P_0 \tag{1.12}$$

- **Bramwell-Hill Equation** - In this model, improvements were made to MK equation by making PWV independent of artery elasticity and artery thickness. PWV was related to artery compliance. The relation of PWV with the pulse pressure is given by eq. 1.13 where $A(t)$ is the artery area as a function of time and dP and dA are differential pressure and artery area. Real time pressure waveform for this model is given by Eq. 1.14. It is assumed that PWV remains relatively constant during a cardiac cycle (C Bramwell, Hill, Crighton B ram ell & H ill (1922)).

$$PWV = \sqrt{\frac{A(t) \cdot dP}{\rho \cdot dA}} \tag{1.13}$$

$$P(t) - P_0 = \rho \cdot PWV^2 \cdot \ln\left(\frac{A(t)}{A_0}\right) \tag{1.14}$$

- **Joukowsky's Equation + PWV** - The equation is based on the principle of water hammer phenomenon. The pressure change is measured from the change in blood's velocity (Δv), PWV and blood density given by eq. 1.15. This model can be used to calculate BP waveform by extracting diameter and blood velocity waveform from consecutive waveform (Soleimani, Mokhtari-Dizaji, Fatouraee & Saberi (2016)).

$$\Delta P = \rho \cdot PWV \cdot \Delta v \tag{1.15}$$

Solving Eq. 1.13 with 1.15, results in Eq. 1.16

$$\Delta P = \rho \cdot (\Delta v)^2 \cdot \frac{A(t)}{\Delta A} \tag{1.16}$$

1.2.5 Performance Parameters in the Transducer for Specific Target Applications

Accurate probe selection hinges on knowing the vessel / organ dimensions and their location beneath the skin—specifically lumen diameter, pulsatile wall movement, anatomical position and imaging depth. Table 1.1 condenses the key performance targets and recommended probe settings for superficial versus deep arteries and for the heart represented in the fig. 1.4. Regardless of site, a fractional beam bandwidth above roughly 50 % is recommended to secure sufficient spatial resolution and faithful waveform capture.

Table 1.1 Target-specific design window for ultrasonic BP-waveform probes, expressed in the qualitative five-column layout used for technology comparisons. Depths, wall excursions and model choices are consolidated PWV and diameter–pressure studies

Target vessel / organ ; (Letters (A–H) correspond to the anatomical sites labeled in Fig 1.4)	**Physiology window** (depth; wall disp.*)	**Suggested acoustic specification**† Amado-Rey et al. (2024)	**Primary BP-estimation model(s)**§	**Imaging trade-off snapshot**
Radial; (A)	2–5 mm depth; 0.02–0.05 mm Domagała et al. (2021)	f_c - 12–20 MHz; axial Δz - 0.08–0.15 mm; DoP‡ - 2–5 mm; high-density linear array ≤10 mm aperture	Exponential; Linear; Beyaz (2021); Li et al. (2022a,2); Worthing (2016); Wu et al. (2023); Xia et al. (2025); Yi et al. (2022); Zhou et al. (2023a,2)	Ultra-high resolution, very shallow reach
Brachial; (B)	3–10 mm; 0.05–0.40 mm Bank et al. (1999); Ko et al. (2015)	f_c - 7–12 MHz; Δz - 0.12–0.25 mm; DoP - 5–10 mm; 20–25 mm linear array	Exponential; Linear; Pen et al. (2022); Yang et al. (2024)	High detail, modest depth tolerance
Carotid (CCA); (C)	5–30 mm; 0.26–0.90 mm Cinthio et al. (2010)	f_c - 5–10 MHz; Δz - 0.15–0.30 mm; DoP - 5–15 mm; large-aperture linear array	Bramwell-Hill; Exponential Joseph et al. (2016); Ng et al. (2023); Sempionatto et al. (2021); Seo et al. (2021); Soleimani et al. (2016); Wang et al. (2018); Xu et al. (2023); Zhou et al. (2024)	Balanced bandwidth vs. depth
Femoral; (D)	10–140 mm; 0.15–1.00 mm Benetos et al. (1993)	f_c - 3–5 MHz; Δz - 0.25–0.40 mm; DoP - 15–30 mm; wide linear / curvilinear array	MK; Bramwell-Hill Shahmirzadi et al. (2012); Westenberg et al. (2012)	Trade-off between depth and detail
Abdominal Aorta; (E)	40–100 mm; 0.57–2.00 mm Giannattasio et al. (2011)	f_c - 2–5 MHz; Δz - 0.35–0.50 mm; DoP - 20–50 mm; broad-beam curvilinear array	MK; Laplace; Joukowsky Hanya (2013); Vorp (2007)	Strong penetration, low axial detail
Heart; (F)	70–90 mm; 12–16 mm (LV wall) Dohi et al. (2008)	f_c - 1–3 MHz; Δz - 0.6–1.0 mm; DoP - 150–200 mm; broadband phased array	Laplace wall stress Klotz et al. (2006)	Excellent reach, coarse spatial resolution
Renal; (G)	30–80 mm; 0.10–0.25 mm Leslie & Sajjad (2023); Xue et al. (2017)	f_c 3–5 MHz; $\Delta z \approx 0.20$–0.30 mm; DoP 30–60 mm; curved / phased array Fernandez (2024); Granata et al. (2009)	MK; Laplace Cho et al. (2021); Fernandez (2024)	Moderate depth, spatial compromise
Ulnar; (H)	2–4 mm; 0.02–0.05 mm Kemmochi et al. (2022); Nielsen et al. (1993)	f_c 12–20 MHz; $\Delta z \approx 0.08$ mm; DoP 2–4 mm; high-density linear array Amado-Rey et al. (2024); Vegas et al. (2025)	Exponential; Linear Cho et al. (2021)	Ultra-high resolution, minimal depth

*Peak systolic–diastolic radial excursion. †Centre frequency f_c chosen as the lowest value meeting lateral-resolution demands; axial resolution $\Delta z \approx c/(2\Delta f)$ assumes 80 % fractional bandwidth. ‡DoP = depth where echo SNR has fallen by 6 dB (soft-tissue attenuation 0.5–0.7 dB cm^{-1} MHz^{-1}). §Model key—Exp P–D: single-exponential pressure–diameter curve; β-index: logarithmic stiffness parameter; BH: Bramwell–Hill distensibility–PWV relation; MK: Moens–Korteweg wave-speed law; Joukowsky: water-hammer pressure surge; PV-loop: left-ventricular pressure–volume relationship.

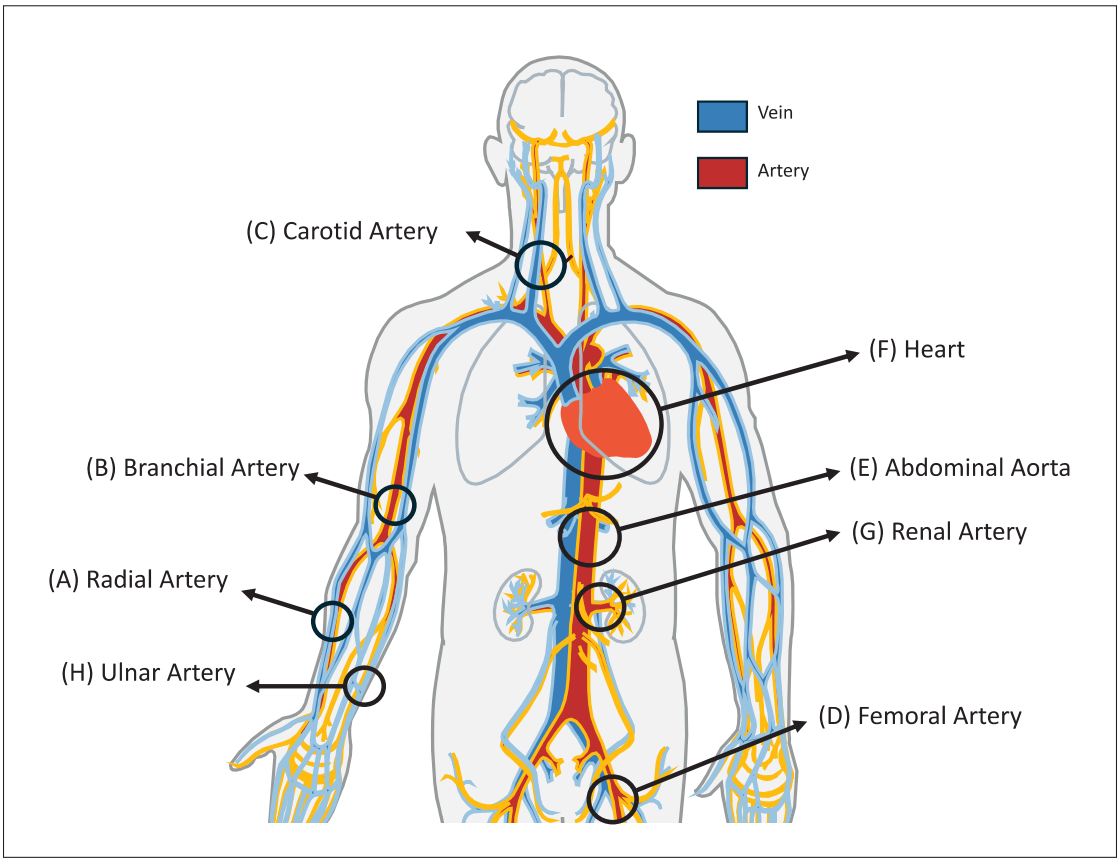

Figure 1.4 Cardiovascular system and major arteries for Blood pressure waveform measurement. (A) Carotid Artery; (B) Radial Artery; (C) Ulnar Artery; (D) Femoral Artery; (E) Renal Artery; (F) Branchial Artery; (G) Abdominal Aorta; (H) Heart

1.3 Ultrasonic transducer technologies

1.3.1 Bulk Transducers

1.3.1.1 General description and working principle

Bulk piezoelectric transducers, most commonly based on lead zirconate titanate (PZT), have been the cornerstone of medical and industrial ultrasound technology for decades. In these devices, a slab or disk of piezoelectric ceramic is polarized and operated in the thickness mode, where an alternating voltage causes the crystal to expand and contract along its thickness,

generating ultrasonic waves at frequencies typically ranging from 1 to 20 MHz for medical imaging (Lethiecq, Berson, Feuillard & Patat (1996)). The high piezoelectric coefficients (d_{33}) and electromechanical coupling factors (k_t) of PZT enable efficient conversion between electrical and acoustic energy, resulting in high sensitivity and strong echo signals. However, the high acoustic impedance of bulk PZT (approximately 30 MRayl) is much greater than that of biological tissue (about 1.5 MRayl), leading to significant reflection at the interface and reduced transmission efficiency. This impedance mismatch also narrows the bandwidth of the transducer, limiting its ability to resolve fine structures in tissue (Chen, Fei, Lin, Gao, Zhang, Quan, Chen, Li & Yang (2022); Li, Ma, Zhang, Shung & Zhu (2022b)).

To address these limitations, the 1-3 piezoelectric composite structure was introduced, wherein parallel rods of piezoelectric ceramic are embedded in a polymer matrix. This design significantly reduces the overall acoustic impedance of the transducer (to 10–20 MRayl), improving the acoustic match to water and tissue and thus enhancing transmission efficiency and sensitivity (Lei, Gao, Gan, Bai, Wei, Wang, Yuan, Hou, Hong & Dong (2025)). Figure 1.5 shows a schematic of a 1-3 piezoelectric composite structure. The 1-3 connectivity ensures that the piezoelectric rods vibrate predominantly in the thickness mode, while the polymer matrix suppresses unwanted lateral vibrations and parasitic modes. This results in a cleaner pulse-echo response and a broader bandwidth-fractional bandwidths of 70–90% at −6 dB are commonly reported for 1-3 composites, compared to 40–60% for bulk ceramics (Lei et al. (2025); Zhu, Ma, Qi, Shen, Liu, Sun, Zhang, Hernández, Ángel, Zhu, Ma, Qi, Shen, Liu, Sun & Zhang (2022)). The increased bandwidth enables higher axial resolution in imaging, which is critical for applications such as echocardiography, ophthalmic ultrasound, and intravascular imaging.

Moreover, the electromechanical coupling coefficient (k_t) of 1-3 composites can exceed 0.7, surpassing that of bulk ceramics, which typically range from 0.45 to 0.55 (Mi, Qin, Liao & Wang (2017)). This higher coupling translates to more efficient energy transfer and improved sensitivity, especially important in array transducers for advanced imaging modalities. The flexibility of the polymer matrix also allows for the fabrication of curved or conformal transducer arrays, further expanding the versatility of ultrasound probe design.

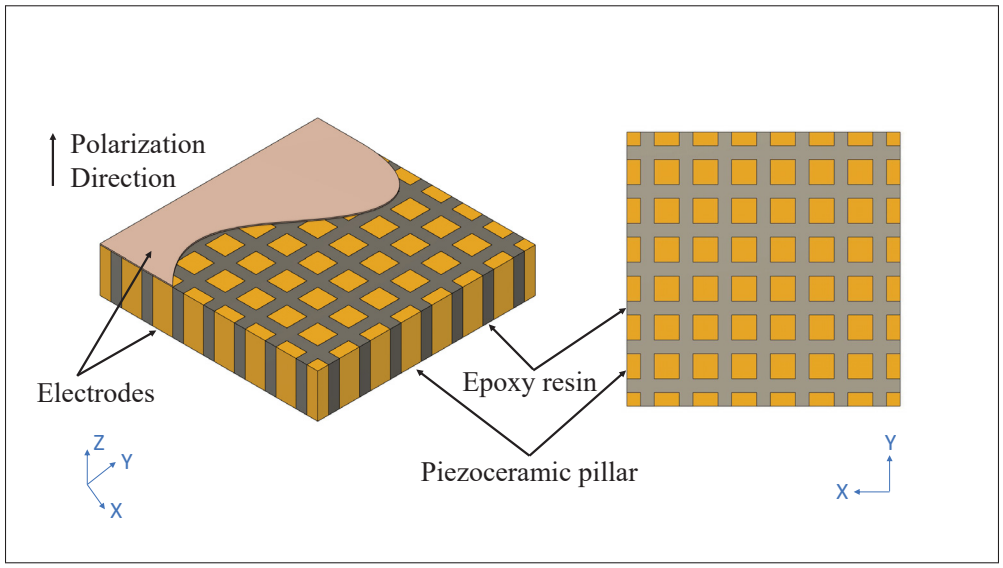

Figure 1.5 Schematic of a 1-3 piezoelectric composite: ceramic pillars embedded in a polymer matrix

Recent advances in fabrication techniques, such as fine-scale dice-and-fill, injection molding, and 3D printing, have enabled the production of high-frequency 1-3 composites with rod diameters below 50 μm, supporting imaging frequencies above 30 MHz for applications in dermatology, ophthalmology, and small animal imaging (Joshi, Sadeghpour, Kuznetsova, Wang & Kraft (2025); Lei et al. (2025)). Owing to the risks of lead oxide leaching into patient tissue, the European Union has imposed strict limits on its use in medical devices. In particular, lead-based ceramics are banned for any application involving direct bodily contact—such as intravascular ultrasound—due to contamination concerns. As a result, the field has turned to alternative, lead-free piezoelectric materials that can match PZT's functional performance in ultrasound transducer fabrication (Reg; Ringgaard, Levassort, Wang, Vaitekunas & Nagata (2024); Rödel, Jo, Seifert, Anton, Granzow & Damjanovic (2009); Shrout & Zhang (2007)).

1.3.1.2 Fabrication

Bulk piezoelectric transducers are typically fabricated by compacting piezoceramic powders, such as lead zirconate titanate (PZT) or barium titanate ($BaTiO_3$), using methods like uniaxial

or isostatic pressing. The compacted material is then sintered at high temperatures to achieve densification, after which electrodes are deposited (often by sputtering or screen printing). The final step is poling, where a strong electric field is applied at elevated temperature to align the ferroelectric domains and induce piezoelectricity (Ogbonna, Popoola & Popoola (2022); Shee, Banerjee, Alagirusamy & Ali (2025)).

The 1-3 piezoelectric composite fabrication process involves forming an array of piezoelectric ceramic rods or pillars (typically PZT or lead-free ceramics) embedded in a polymer matrix. The most common method is the "dice-and-fill" technique, where a bulk ceramic is diced to create pillars, and the voids are filled with polymer, followed by curing and electrode application. This structure reduces lateral coupling and acoustic impedance, enhancing bandwidth and sensitivity, which is especially advantageous for ultrasonic and biomedical transducer applications (Newnham, Safari, Giniewicz & Fox (1984); Ogbonna et al. (2022)).

Materials such as barium titanate ($BaTiO_3$) and potassium sodium niobate (KNN) are increasingly used in both bulk and composite transducer designs, offering improved environmental compatibility and promising piezoelectric performance (Ogbonna et al. (2022); Ringgaard et al. (2024)).

In summary, while bulk piezoelectric transducers remain important for their simplicity and high output, 1-3 piezoelectric composites offer superior acoustic matching, bandwidth, and sensitivity, making them the preferred choice for high-performance medical ultrasound and advanced imaging applications.

While conventional bulk ultrasound sensors have long been used for various applications, including medical imaging (Peng, Chen, Spicer & Jiang (2021b); Ter Haar (2001)), industrial non-destructive testing (Drinkwater & Wilcox (2006); Jiang, Kim, Zhang, Johnson & Salazar (2014)) and sensing (Jiang, Tang, Lu, Ng, Tsai, Boser & Horsley (2017); Tang, Lu, Jiang, Ng, Tsai, Horsley & Boser (2016)) due to their benefits, such as non-invasiveness, convenience, safety, high penetrability and sensitivity (Li, Ma, Zhang, Shung & Zhu (2022c)), these sensors often suffer from several drawbacks that limit their overall performance. Bulk ultrasound sensors

tend to be large and heavy and require complex transducer configurations, resulting in increased manufacturing costs. Moreover, their size can impede their integration into compact devices and limit their use in portable applications (Brown et al. (2014); Cochran (2012); Shung & Zipparo (1996)). In addition, conventional bulk sensors can consume significant power, leading to higher operational costs and reduced battery life in portable systems (Przybyla et al. (2011)). In contrast, ultrasound MEMS sensors offer a promising solution to overcome these limitations. MEMS technology allows the miniaturization of sensors, enabling the fabrication of microscale ultrasonic transducers (Judy (2001)). This miniaturization results in smaller and lighter devices that can be easily integrated into compact systems. Furthermore, MEMS ultrasonic sensors demonstrate improved energy efficiency, making them suitable for battery-operated and portable applications (Pattanaik & Ojha (2023)). There are 2 families of MEMS ultrasound devices, CMUTs and PMUTs.

1.3.2 MEMS Ultrasonic Transducers

Micro-Electromechanical Systems (MEMS) integrate miniature mechanical structures, sensors, actuators (and sometimes electronics) on a single silicon-based chip using micromachining techniques, yielding devices whose critical features span tens to hundreds of micrometers and whose packaged footprints are only a few square millimeters (Algamili, Khir, Dennis, Ahmed, Alabsi, Ba Hashwan & Junaid (2021)). Early MEMS found success in inertial sensors and microphones, and over time the technology has permeated microfluidics, energy harvesting, RF components and lab-on-a-chip platforms for analytical biology and chemistry (Herrera-May, Soler-Balcazar, Vázquez-Leal, Martínez-Castillo, Vigueras-Zuñiga & Aguilera-Cortés (2016); Kavallaris & Suzuki (2018); Lee, Kim & Kim (2018); Lee, Kong & Zhang (2016); Rafiee, Khatibi & Zehetbauer (2017)). In biomedical contexts—where they are often termed BioMEMS, μTAS or biochips—these devices support drug delivery, microsurgery, diagnostics, artificial organs, and cell manipulation tools (Gaudin (2019); Huang, Zhao, Liang & Wang (2018); Liang, Guo & Fan (2019); Lyshevski (2002); Martinez-Rivas, González-Quijano, Proa-Coronado,

Séverac & Dague (2017); Montalvão (2015); Pan, Wang, Ru, Sun & Liu (2017); Tung, Gower, Ooteghem, Nouredanesh & Gage (2021)).

Micromachined ultrasonic transducers (MUTs) generate ultrasound by patterning a thin vibrating membrane directly on silicon or flexible substrates alongside CMOS electronics, all in a single MEMS process flow (Judy (2001); Pattanaik & Ojha (2023)). This monolithic integration eliminates bulky connectors and matching networks, sharply reducing energy loss and enabling compact, low-power designs. Because the membrane resonates in a flexural mode, its mechanical impedance is much closer to that of soft tissue than bulk PZT ceramics, often eliminating the need for separate matching layers and simplifying fabrication (Chorsi, Curry, Chorsi, Das, Baroody, Purohit, Ilies & Nguyen (2019)). Moreover, unlike traditional transducers whose frequency is set by material thickness alone, MUTs allow resonance tuning through membrane geometry, such as diameter, shape, and layer stack, providing designers with exceptional flexibility. Fabrication use the same materials as MEMS: silicon for structural layers, SiO_2/Si_3N_4 for sacrificial or insulation layers, and polymers (SU-8, polyimide, parylene) or nanocomposites for encapsulation and biointerface coatings (Badry et al. (2020); José Horst et al. (2020); Keçili, Büyüktiryaki & Hussain (2020); Kenawy & Khalil (2020); Kim & Meng (2015); Prabakar et al. (2020); Qin et al. (1998); Shanbhag & Patil (2017); Teh (2017); Yao & Peddi (2016); Zorman & Mehregany (2004)). Finally, the choice of piezoelectric thin film, from high-coupling PZT to CMOS-friendly AlN or even flexible PVDF, lets one balance sensitivity, bandwidth, and drive voltage to meet the demands of clinical imaging and wearable blood pressure monitoring (Chorsi et al. (2019)).

1.3.3 Modeling of MEMS Ultrasonic Transducers

Medical ultrasound transducers convert electrical signals into sound waves, and back again, by vibrating a thin membrane. A simple way to imagine the motion of this membrane is as a mass on a spring with some friction (Fig. 1a). When a driving force F is applied, the membrane (mass m) moves against the spring (stiffness k) and is slowed by damping (coefficient b), yielding eq. 1.17,

$$m\,\ddot{x} + b\,\dot{x} + k\,x = F, \tag{1.17}$$

where x is the displacement of the membrane, m is the mass of the membrane, b is the damping coefficient, k is the total spring constant and F is the applied external force. The natural frequency f_r of the membrane given by eq. 1.18,

$$f_r = \frac{1}{2\pi}\sqrt{\frac{k}{m}} \tag{1.18}$$

indicates its optimal generation or detection frequency (Moten; Smyth & Kim (2015)). Although the mass-spring model accurately captures the flexural behavior of the membrane, it cannot predict the electrical characteristics of the MUT, which are crucial for the analysis and design of the transducer's front-end electronics.

To integrate this into electronics, the Mason equivalent circuit is used where the membrane's static capacitance C_0 appears at the electrical port. An L–C–R network models the mass (L), spring (C), and damping (R), linked by a transformer of ratio $1:\eta$ that converts voltage to mechanical force, and another transformer of ratio $A_{\text{eff}}:1$ converting displacement to acoustic pressure over area A_{eff} (Shen, Xu, Li, Chen, Cui & Jian (2021); Sherrit, Leary, Dolgin & Bar-Cohen (1999)). This approach captures the coupled electromechanical and acoustic behavior of the transducer by linearizing around its bias operating point (Pop, Herrera, Cassella & Rinaldi (2020); Smyth & Kim (2015)), but it does not account for any non-linear distortion effects.

Real-world devices exhibit non-ideal effects: CMUT pull-in instability under large DC bias is analyzed via modified lumped models and stability criteria, while PMUT piezoelectric hysteresis and non-linear stiffness have been quantified and incorporated into refined damping models $b(x)$ (Moten; Shen et al. (2021)).

For full-wave analysis, including nonlinearities, mode shapes, and stress distributions, finite element modeling (FEM) is indispensable and is the standard in both academic and industrial

transducer design. FEM can couple piezoelectric constitutive equations with structural mechanics and acoustics to calculate impedance and acoustic output over wide frequency ranges (Moten; Shen et al. (2021); Smyth & Kim (2015))

1.3.4 PMUTs (Piezoelectric Micromachined Ultrasonic Transducers)

PMUTs consist of a thin membrane that vibrates when subjected to an alternating voltage. This thin membrane is supported by an acoustic cavity, allowing it to deform. PMUT structure is shown in Fig. 1.6. The PMUT membrane consists of a thin piezoelectric layer that is sandwiched between two electrodes and can be used to transmit and receive ultrasound waves (Wang, Kobayashi & Lee (2016a)). An AC voltage is applied across the electrodes to drive the membrane along the direction perpendicular to the surface of the device. This AC voltage creates an electric field across the piezoelectric layer, which also creates a transverse displacement of the membrane. This flexural movement creates pressure acoustic waves that are transmitted through the medium. In transmit mode, the piezoelectric membrane vibrates to generate ultrasonic waves, while in receive mode, the incoming ultrasonic waves cause a slight deformation of the membrane, generating an electrical signal through the piezoelectric effect (Liu, Yoshida, Horsley & Tanaka (2022); Sadeghpour, Joshi, Wang & Kraft (2022)). PMUTs utilize thin-film piezoelectric films as their transduction mechanism, offering advantages over bulk thick-film ultrasound transducers. They require lower actuation voltages, making them energy-efficient and suitable for portable applications. In addition, PMUTs exhibit efficient impedance matching in both air and water, and their compact size provides greater versatility and convenience (Roy, Lee & Lee (2023)).

The resonant frequency and performance of PMUTs depend significantly on the properties of the piezoelectric material, shape, dimensions, boundary conditions, intrinsic stress, and mechanical stiffness of the membrane (Qiu, Gigliotti, Wallace, Griggio, Demore, Cochran & Trolier-McKinstry (2015); Wong, Roy, Lee & Zhu (2024)). The most commonly reported diaphragm shapes in the reported literature are circular and square. These shapes are favored due to their consistent reliability and the simplicity they offer for equivalent modeling,given that

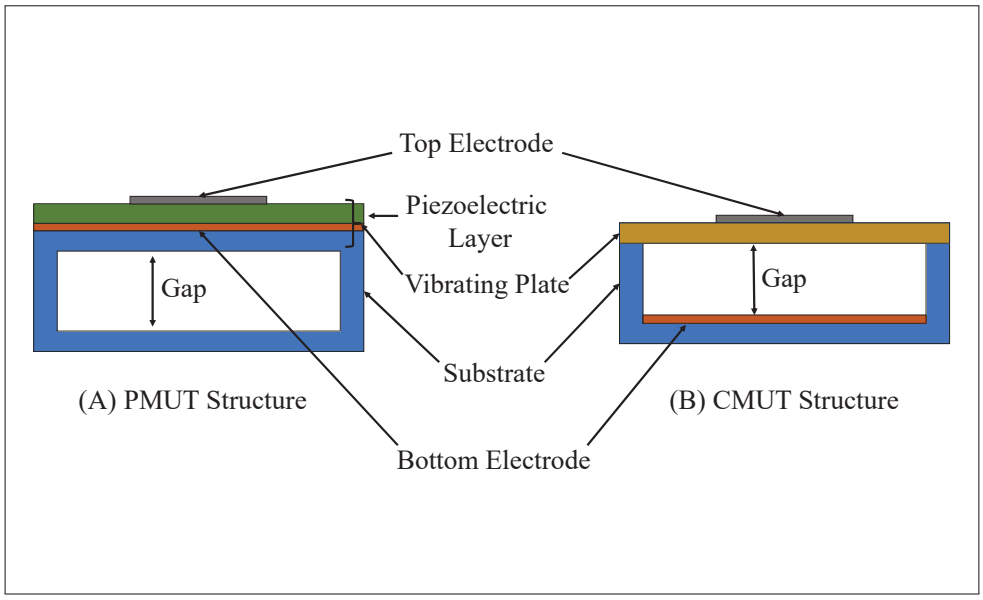

Figure 1.6 (A) PMUT and (B) CMUT Structures

their resonant frequencies can be determined analytically. In particular, for a circular-shaped fully-clamped transducer, the resonant frequency is given by eq. 1.19,

$$f_r = \frac{\alpha}{2\pi r^2}\sqrt{\frac{D_E}{\rho h}} \tag{1.19}$$

where α is the first mode circular constant, r is the radius of the membrane, D_E is the flexural rigidity, ρ is the density of the membrane, and h is the thickness of the membrane (He, Wan, Jiang & Peng (2022)).

An important parameter to consider in the fabrication of PMUT is the thickness of the active piezoelectric layer. As membrane deflection is induced by the lateral strain produced by the piezoelectric effect, transverse dynamic strain should be avoided and this is guaranteed when the PZT has a thickness under 3 µm (Roy et al. (2023)). Thus, thin-film-based devices are preferred over thick-film PMUTs, as they present better performance (they easily deform with low amounts of stress), a better temperature coefficient and greater stability (Wong et al. (2024)).

The common piezoelectric materials used include lead zirconate titanate (PZT), polyvinylidene fluoride (PVDF), aluminum nitride (AlN) and zinc oxide (ZnO). Each material has unique characteristics that influence its suitability for specific applications (Zang, Fan, Li, Duan, Wu, Cui & Xue (2022); Zhang, Yan, Ye, Luo, He & Chou (2024)).

PVDF is commonly used in piezoelectric bulk transducers as a result of its chemical resistance and thermal properties. However, it degrades at high temperatures over time and presents challenges for thin film production and adhesion to substrates and metal, requiring bonding (Moisello, Novaresi, Sarkar, Malcovati, Costa & Bonizzoni (2024)).

PZT thin films for PMUT applications are typically deposited to thicknesses of 0.3–3 µm, using techniques such as sputtering (0.3–2 µm), sol–gel processing (0.5–1.5 µm), and metal–organic chemical vapour deposition (MOCVD) (up to 3 µm). Post-deposition annealing at 550–700 °C is required to crystallize the perovskite phase and maximize piezoelectric performance (Jung, Han, Ning, Kim, Choi, Jang & Baek (2024)).

In undoped polycrystalline PZT films, the transverse piezoelectric coefficient d_{31} typically ranges from –100 to –180 pm/V, with electromechanical coupling factors $k_t \approx 0.40$–0.50 and relative permittivities $\varepsilon_r \approx 800$–$2000$. Substitutional Nb doping (PZNT) improves these properties, increasing d_{31} to -150 to -230 pm / V and k_t to 0.50–0.65, at the cost of higher thermal budgets and increased considerations of lead toxicity (Ichinose, Shimizu, Sakata, Yamada, Ehara & Funakubo (2021)).

Monocrystalline PZT films offer further performance improvements: d_{31} increases to –150 to –220 pm/V, ε_r decreases to 500–800, and the Curie temperature rises to 360 C (versus 320 C in polycrystalline films) (Wong et al. (2024)).

For lower-temperature or non-ferroelectric implementations, aluminium nitride (AlN) and zinc oxide (ZnO) films can be used. Sputtered AlN (deposited below 350 °C) exhibits $d_{31} \approx 2$ pm/V and $\varepsilon_r \approx 9$, while c-axis-textured ZnO typically achieves $d_{31} \approx 10$–15 pm/V and $\varepsilon_r \approx 8$–10 (Wong, Na, Chen, Li, Macecek & Yeow (2016)).

While PZT offers excellent piezoelectric properties, its high-temperature deposition poses challenges for CMOS integration and may release harmful lead. As an alternative, AlN thin films allow monolithic integration with CMOS through low temperature sputtering, making them favorable for specific transducer applications (Birjis, Swaminathan, Nazemi, Raj, Munirathinam, Abu-Libdeh & Emadi (2022); Sun, Wang, Zhang, Ning, Ma, Yuan, Niu, Rong, Wang & Pang (2022)).

1.3.4.1 Fabrication of PMUTs

The fabrication of PMUT arrays can be broadly categorized into two types: rigid and flexible PMUT arrays. Rigid PMUT arrays are created using either bulk micromachining or surface micromachining techniques. On the other hand, flexible PMUT arrays can be further classified into two subtypes: those with flexible substrates but rigid elements and fully flexible arrays (Roy et al. (2023)).

Bulk micromachining involves etching a single silicon-based substrate to form the entire PMUT structure. This process enables the creation of intricate 3D structures with high aspect ratios, ideal for PMUT applications. Careful control of the etching parameters ensures an accurate definition of the thin piezoelectric layer and acoustic cavity, optimizing transducer performance. A first process uses a pyrogenic oxide coating on the bottom surface of the silicon wafer, followed by boron diffusion and oxide deposition for electrical isolation. Deep Silicon Wet Etching is then used to release the diaphragm, and a metalized sol-gel PZT sandwich is coated on the top surface to create electrical contacts (Akasheh, Myers, Fraser, Bose & Bandyopadhyay (2004)). In another process, a silicon-on-insulator (SOI) substrate undergoes surface oxidation and metalization, followed by deep reactive ion etching to release the membrane. A third process involves the use of a bulk lithium niobate ($LiNbO3$) crystal that is metalized, flipped, and bonded to a silicon wafer. Metal deposition and etching define the structure, and deep reactive ion etching releases the membrane (Belgacem, Calame & Muralt (2005)).

Surface micromachining is another method where thin films of different materials are deposited on the substrate and selective etching shapes the desired structures. This process allows for the creation of complex 3D structures, including beams, cantilevers, membranes, and gears, with precise control over their dimensions and positions. Surface micromachining is commonly employed in the fabrication of various MEMS devices such as accelerometers, gyroscopes, pressure sensors, micro-mirrors, and microfluidic devices. In one surface micromachining process, the silicon wafer is coated with wet oxide and silicon nitride. Reactive ion etching is used to create a shallow trench, and another wafer is bonded to it with an oxide-coated surface facing downward. The upper layer of silicon is thinned and a metal sandwich containing PZT material is deposited and selectively etched (Yang, Tian, Wang, Shu, Zhou, Sun, Zhang, Chen & Ren (2013)). In another process, a silicon wafer is subjected to oxidation, nitride coating, and metalization with ZnO. Etching creates the desired pattern, and wet etching releases the membrane (Perçin & Khuri-Yakub (2002)).

Flexible PMUT arrays with rigid elements have a flexible array structure with individual rigid PMUT elements. One study utilized an oxidized SOI substrate, underwent metalization, and patterned etching to achieve the desired structure. PZT material was patterned and further oxidized and metalized to establish the top contacts. Deep reactive ion etching (DRIE) was used to release the membrane by etching through the bulk silicon, followed by patterned reactive ion etching (RIE) to selectively etch silicon from the top, forming bendable springs (Sadeghpour, Lips, Kraft & Puers (2020)).

Fully flexible PMUTs consist of both a flexible PMUT array and flexible PMUT elements. In one study, a fully flexible PMUT array was fabricated using the flexmems process. A transferable PMUT was fabricated on a silicon donor substrate, detached using a diluted HF solution, and a PDMS stamp was used to pick up the PMUT structure and separate it from the donor substrate. A flexible receiver was fabricated by depositing a thin layer of PMMA (sacrificial layer) and then a layer of polyimide on a silicon wafer. Photolithography and etching were used to pattern a cavity, and the PMUT structure was aligned to this cavity and transferred to the receiver

substrate. The sacrificial layer was removed using acetone, separating the silicon wafer from the flexible polyimide layer (Sun, Zhang, Gao, Liu & Pang (2018)).

1.3.5 CMUTs (Capacitive Micromachined Ultrasonic Transducers)

CMUTs are ultrasound transducers that are based on an electrostatic transduction mechanism. The structure of CMUT is described by Fig. 1.6. The device is comprised of a metalized or highly conductive membrane anchored above an air or vacuum cavity (Sewify, Antico, Alzubaidi, Alwzwazy, Roots, Pivonka & Fontanarosa (2025)). This flexible membrane acts as the top electrode, while another electrode is located on the stationary lower substrate within the cavity. This gap between the upper and lower electrode creates a shallow cavity, forming a variable capacitor (Ergun, Yaralioglu & Khuri-Yakub (2003); Joseph, Ma & Khuri-Yakub (2022)). The device operates on the basis of electrostatic forces. Under a time-varying bias $V(t)$, the instantaneous electrostatic force on the CMUT plate is given by eq 1.20 (Biriukov & Korsunsky (2024)),

$$F_{\text{elec}}(x,t) = -\frac{A\,\varepsilon_0\,\varepsilon_r\,V(t)^2}{2\,(g-x)^2}. \tag{1.20}$$

where g is the gap distance, A is the area of the membrane and $V(t)$ is the time varying voltage across the electrodes. The cavity can be filled with vacuum or air and typically features an electric field of the order of several tens of volts per μ or more (Brenner, Ergun, Firouzi, Rasmussen, Stedman & Khuri-Yakub (2019); Herrera-May et al. (2016); Nathani, Nazemi, Love, Lopez, Swaminathan & Emadi (2020)), thus resulting in a high electro-mechanical coupling coefficient. In order to prevent any contact—and consequent short circuit—between the electrodes, an insulating layer can also be added (Brenner et al. (2019); Gerardo et al. (2018)).

In transmission mode, a time-varying voltage applied between the electrodes causes the membrane to vibrate in the cavity, generating ultrasound waves during transmission (Caliano, Matrone & Savoia (2017)). In receive mode, incoming ultrasound pressure waves cause membrane deflection, altering the capacitance, which is sensed to calculate the resulting pressure variation. To ensure linear operation in transmission and signal generation during

reception, CMUTs rely on a bias voltage (Pappalardo, Caliano, Savoia & Caronti (2008)). As the bias voltage increases, the gap between the membrane and the bottom electrode reduces. Eventually, the bias voltage reaches a critical value known as the pull-in or collapse voltage, where the membrane collapses onto the bottom electrode (Bayram, Oralkan, Ergun, Hæggström, Yaralioglu & Khuri-Yakub (2005)). The pull-in voltage ($V_{pull-in}$) can be expressed by eq. 1.21

$$V_{\text{pull-in}} = \sqrt{\frac{8\, k_{\text{eff}}\, g^3}{27\, \varepsilon_0\, \varepsilon_r\, A}} \tag{1.21}$$

This is a vital characteristic for the performance of CMUT, as the efficiency is maximum when the bias voltage nearly reaches the collapse voltage (Biriukov & Korsunsky (2024); Goel, Cicek & Robichaud (2022b)).

The spring softening effect in CMUTs is dependent on DC bias (V_{DC} and leads to a change in resonance frequency. As the bias voltage increases, the top electrode moves closer to the bottom electrode, resulting in an increased electric field. This displacement (x)causes the top electrode to behave as if its spring constant decreases under the influence of the applied voltage (Ding, Wang, Zhang, Huang, Sun, Qin, Ren, Zhu, He & Zhang (2021)). Mathematically, the effective spring constant is given by eq. 1.22 (Biriukov & Korsunsky (2024); Ding et al. (2021))

$$k_{\text{eff}} = k_{\text{mech}} - \frac{A\, \varepsilon_0\, \varepsilon_r\, V_{\text{DC}}^2}{(g - x^3)} \tag{1.22}$$

and the resonance frequency softens to f_{eff} given by eq. 1.23

$$f_{\text{eff}} = \frac{1}{2\pi}\sqrt{\frac{k_{\text{eff}}}{m}} \tag{1.23}$$

In array implementations, element pitch and fill-factor critically determine beam-forming performance and mutual coupling. A high fill-factor (>80 %) maximizes transmit efficiency but can exacerbate cross-talk; care must be taken in interconnect layout and ground shielding.

Advanced topologies (e.g., uniplanar or conformal arrays) have been demonstrated to optimize field-of-view while minimizing grating lobes (Huang, Wang & Yu (2021); Oralkan, Ergun, Johnson, Karaman, Demirci, Kaviani, Lee & Khuri-Yakub (2002b); Oralkan, Ergun, Cheng, Johnson, Karaman, Lee & Khuri-Yakub (2003b)).

1.3.5.1 Fabrication of CMUTs

With respect to the fabrication of CMUT arrays, two main processes are utilized: sacrificial release and wafer-bonding methods. In the sacrificial release process, a silicon nitride insulation layer is deposited on a highly doped wafer (bottom electrode), followed by the deposition and patterning of polysilicon sacrificial layers to create anchors for the deflecting membrane. Afterward, silicon nitride is deposited to form the top layer and channels are created to allow KOH wet etching to remove the sacrificial layers. The resulting gap is vacuum sealed by low-pressure chemical vapor deposition (LPCVD) of silicon nitride. Aluminum is sputtered to form the top electrode, and the height of the cavity is determined by the thickness of the sacrificial polysilicon layer (Brenner et al. (2019)).

In the wafer-bonding method, a heavily doped Si wafer is subjected to thermal oxidation to define the CMUT gap height. Lithography is used to define the gap dimensions and geometry, and a second thermal oxidation passivates the exposed Si to prevent shorting. Etching removes bumps along the upper edge of the cavity. The SOI wafer is then directly bonded to the oxidized Si wafer, and another thermal oxidation covalently bonds the two wafers. Mechanical grinding and wet etching release the handle and buried oxide from the SOI wafer, forming the CMUT plates. Electrical contact is created through metal sputtering, and device isolation etch separates the metal pads and isolates the devices, defining the array. Oxide or nitride deposition is used for passivation to prevent surface conduction. Lastly, a low-temperature deposition provides sidewall passivation (Brenner et al. (2019)).

Capacitive micromachined ultrasonic transducers (CMUTs) leverage electrostatic actuation between a suspended membrane and a rigid substrate to achieve ultra-wide bandwidth (>100

%) and seamless CMOS integration (Caliano et al. (2017)). Two primary fabrication methods, sacrificial release (polysilicon cavities sealed with LPCVD nitride) and direct SOI wafer bonding, have matured to produce uniform vacuum-sealed devices (Brenner et al. (2019); Roy et al. (2023)).

1.4 Technological evolution for BP Waveform Monitoring using ultrasound transducers

Over the past decade, ultrasound-based blood pressure (BP) waveform monitoring has evolved from bulky, stationary systems to miniaturized, wearable platforms. Early work focused on bulk piezoelectric transducers, which proved the feasibility of non-invasive waveform reconstruction but suffered from size, power, and alignment limitations. More recently, micromachined devices, PMUTs and CMUTs have addressed many of these challenges, offering low-voltage operation, high spatial resolution, and potential for on-chip integration. A detailed qualitative comparison between different ultrasound technologies and their applicability for blood-pressure waveform monitoring is in Table 1.2. This section reviews the chronological progression of these technologies, weaving together seminal studies to illustrate how each builds on its predecessors.

1.4.1 Bulk Piezoelectric Transducers

1.4.1.1 Non-flexible substrate based devices

In 2015, Seo *et al.* (Seo et al. (2015b)) demonstrated that a two-element bulk ultrasound probe could extract blood pressure waveform by simultaneously tracking vessel cross-sectional area (via Doppler) and volumetric flow (Fig. 1.7).

PWV was calculated using the flow area (QA) method instead of the more traditional pulse transit time (PTT) method to reduce errors in the area of interest. Mathematically, PWV_{QA} can be defined by eq. 1.24 where Z_c is the characteristic impedance of the vessel given by eq. 1.25.

Table 1.2 Qualitative Comparison of Ultrasonic Transducer Families for Continuous, Cuff-Free Blood-Pressure Waveform Monitoring

Technology	**Acoustic Principle and Bandwidth Profile (Amado-Rey et al. (2024))**	**Wearability & Skin Coupling (Joshi et al. (2025); Moisello et al. (2024))**	**Electronics & Power Demand (Joshi et al. (2025); Moisello et al. (2024))**	**Validation Stage***
Bulk PZT	Thickness-mode ceramic; moderate BW, high acoustic impedance, strong output pressure.	Rigid crystal; must be pressed against gel pad or standoff block—impractical for day-long wear.	Pure AC excitation but tens–hundreds V_{pp}; large matching network.	Human catheter-matched demos (TRL 6) (Seo et al. (2015b); Xu et al. (2023)).
1-3 Piezo-composite	Composite rods in polymer give lower impedance and broader BW (60–90 %).	Millimetre-thin film can bend around wrist; still needs gel but tolerates slight motion.	20–50 V_{pp} AC; no DC bias; front-end ICs available off-the-shelf.	Radial-artery patch with < 1% SBP/DBP error (TRL 6) (Peng et al. (2021a)).
PMUT (rigid Si die)	Flexural membrane in vacuum/air cavity; 80–110 % BW; centre freq 5–10 MHz.	Silicon chip glued to soft lens; patch thickness ≈ 4 mm; positional drift if strap loosens.	5–20 V_{pp} AC; CMOS co-integration possible.	Pilot human wrist study, single-session (TRL 5) (Pen et al. (2022); Zhou et al. (2023a)).
PMUT (soft stretch patch)	Same membrane physics but over-moulded in silicone; BW somewhat narrower after encapsulation.	Ecoflex-backed array stretches 60 %; adheres without gel for several hours.	15–25 V_{pp}; discrete driver IC on flex PCB; coin-cell lasts <8 h.	Wearable prototypes exist (TRL 4) (Xia et al. (2025); Zhou et al. (2025)).
CMUT (rigid Si die)	Electrostatic gap transducer; ultra-broad BW > 100 %; near-perfect impedance match.	Rigid die; still relies on gel and strap; bias converter adds bulk.	30–100 V DC bias + 3–10 V_{pp} AC; needs charge pump and safety guard.	In-vivo imaging; no in-vivo BP waveform yet (TRL 3) (Gurun et al. (2014); Liu et al. (2019)).
CMUT (flex concept)	Polyimide diaphragm with vacuum cavity; bandwidth similar to rigid CMUT.	Concept designs show micron-thin, conformal sheet; vacuum seal durability unproven.	20–60 V DC bias; low AC swing; ultra-low mass allows on-skin electronics.	Proof-of-principle (TRL 2) (Omidvar et al. (2021); Welsch et al. (2022)).

*Technology-readiness interpretation: 1 = idea, 3 = lab prototype, 5 = first human/pilot, 7 = extended in-vivo trials, 9 = marketed device.

$$\mathrm{PWV_{QA}} = \sqrt{\frac{A}{\rho}\frac{\mathrm{d}P}{\mathrm{d}A}} = \frac{1}{Z_\mathrm{c}}\frac{\mathrm{d}P}{\mathrm{d}A} = \frac{\mathrm{d}Q}{\mathrm{d}P}\frac{\mathrm{d}P}{\mathrm{d}A} = \frac{\mathrm{d}Q}{\mathrm{d}A} \tag{1.24}$$

$$Z_\mathrm{c} = \frac{\mathrm{d}P}{\mathrm{d}Q} = \sqrt{\frac{\rho}{A}\frac{\mathrm{d}P}{\mathrm{d}A}} \tag{1.25}$$

The PWV and arterial diameter waveform obtained using wall tracking is inputted to Bramwell-Hill Equation to calculate the blood pressure waveform. They measured PWV at 8.47 ± 0.63 m/s and reported a scaling error of -1.56 ± 14.0%. This method also requires a cuff-based calibration to measure diastolic pressure and the corresponding diameter of the artery. A skilled

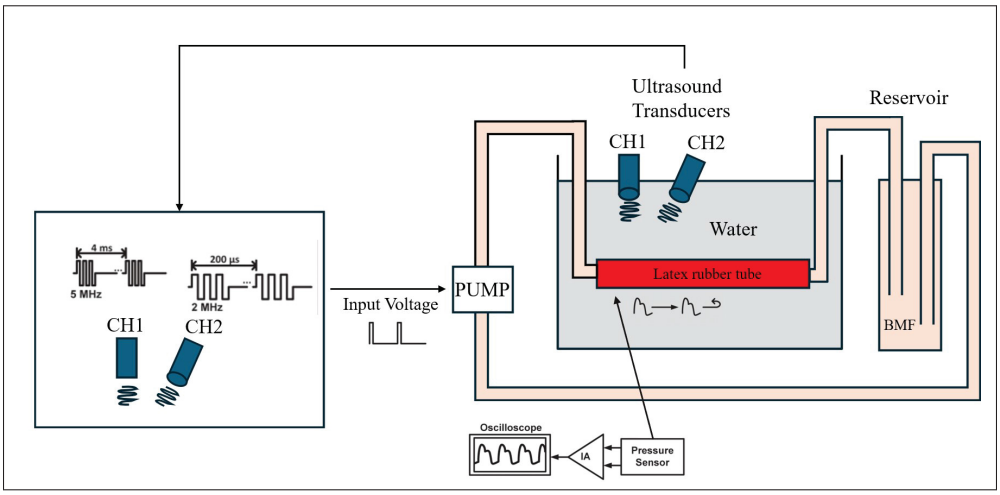

Figure 1.7 Test setup for two-element bulk ultrasound probe
Taken from author Seo et al. (2015b)

sonographer is needed to accurately align the transducer with the center of the artery as the device lacks vessel tracking elements.

Building on this, Xu *et al.* (Xu et al. (2023)) replaced the two elements with three element transducers to track arterial wall displacement as shown in fig. 1.8. Then, unlike the earlier work, the PWV in this study was calculated by measuring the time taken by the pressure wave to travel between elements of the transducer. This study also used the Bramwell–Hill equation to obtain the real-time blood pressure waveform. The novel transducer was evaluated by comparing the waveform with arterial tonometer and demonstrated a high correlation ($r = 0.978 \pm 0.014$). The mean absolute error obtained from the transducer was found to be within 5 ± 8 mmHg for diastolic pressure, systolic pressure and MAP (Xu et al. (2023)) in in-vivo study. Using three element transducer instead of two elements reduced errors and improved accuracy of measurements. It was noted that high pulse repetition frequency is important to obtain accurate data point for local PWV measurement. It should be noted that this study only measured the Pulse pressure waveform and calibrated the minimum pressure with the measurements of tonometer to make the comparison. Several limitations were also noted in the literature. The assumptions regarding arteries like perfectly elastic and cylindrical geometry undermine the effects artery complexity. Viscoelastic behaviour causes the distension waveform to lag behind

the pressure waveform and leads to nonlinear propagation of the PWV. Improvements can be made by implementing this blood pressure monitoring method on flexible MEMS for wearable operation. Effects of misalignment of transducer over the artery were not discussed as it can increase time required and accuracy for measurements.

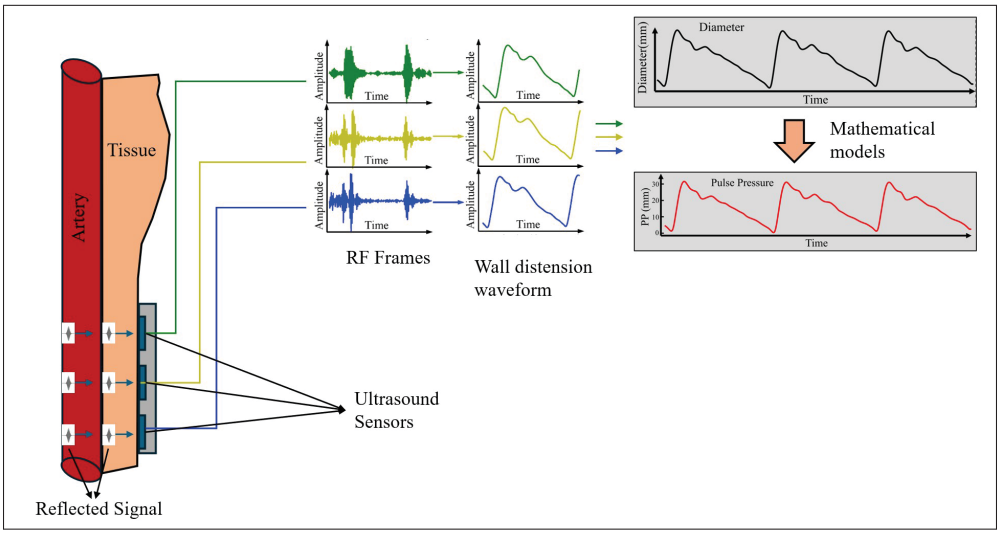

Figure 1.8 3 element bulk piezoelectric transducer to track arterial wall displacement
Taken from author Xu et al. (2023)

1.4.1.2 Flexible substrate based devices

Most of the studies which employed flexible substrate based devices used 1-3 piezoelectric composite transducers (Li et al. (2023); Peng et al. (2021a); Wang et al. (2018)). One of the earliest studies was done by Wang et. al (Wang et al. (2018)) where an ultra-thin conformal ultrasonic device was proposed for non-invasive blood pressure waveform monitoring. The device only measured 240 μm in thickness and could stretch up to 60%. The device was formed of 1-3 piezoelectric composite in a 4 x 5 array and operated at a frequency of 7.5 MHz. To make the device wearable and conformal, the device used ecoflex as a substrate. The individual elements could be operated independently which enabled sensing of artery location and bypass the need for manual alignment. This device was also based on the principle of continuous measurement of artery diameter which is translated to BP waveform using exponential relation.

This work was taken forward by Peng *et al.* (Peng et al. (2021a)) by improving the transducer design and flexibility by introducing flexible electrodes Au and AgNWs. The device is fabricated with PZT-5H for its high electromechanical coupling coefficient and dielectric constant and filled with PDMS for its excellent flexibility, biocompatibility and impedance matches with the impedance of human tissue. The fabrication process resulted in flexible piezo-composite ultrasonic sensor. The test setup is represented by fig. 1.9. The sensor was operated at a frequency of around 5 MHz. This study also used exponential relation to translate the artery waveform to blood pressure waveform.

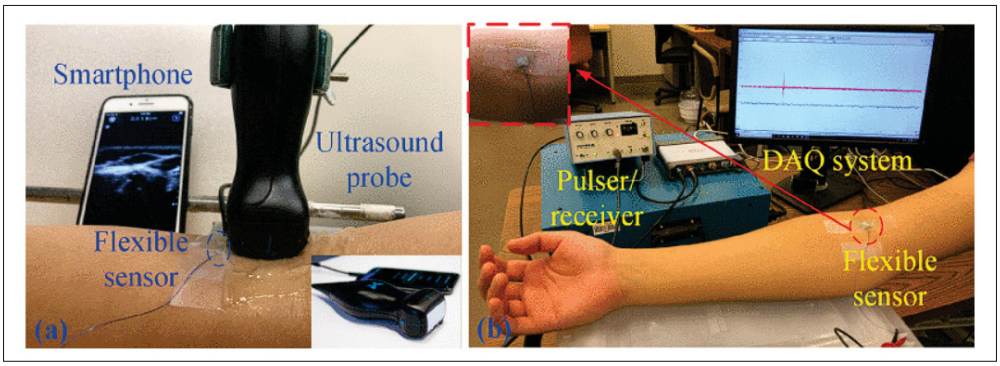

Figure 1.9 Schematic of measurement configuration for measuring the ulnar artery diameter variations. (a) Measurement by using the ultrasound probe, (b) Measurement by using the flexible sensor Taken from author Peng et al. (2021a)

Following up on using this transducer technology, a study by Li et. al. (Li et al. (2023)) envisioned fabric-based ultrasonic sensor (FAUS) with an integrated 1-3 piezoelectric composite. Using textile fiber materials is a step further to make non invasive, conformal and a long term wearable blood pressure monitoring sensor. This sensor employed an "S"-shaped stretchable island bridge electrode on a fabric substrate using hot press transfer technique for better stretchability, represented by fig. 1.10. The device featured a 4 × 5 array of ultrasonic sensors and operated at 7.5 MHz. This study also reported using PZT-5H as the piezoelectric layer and filled with a conductive epoxy resin. The electrodes were made by laser cutting copper and encapsulated with Polyimide. The fabric substrate selected was a polyester ammonia elastic fabric for its good

abrasion resistance, good elasticity, good air permeability, and fast drying. This study also used the exponential relationship to convert artery diameter waveform to blood pressure waveform.

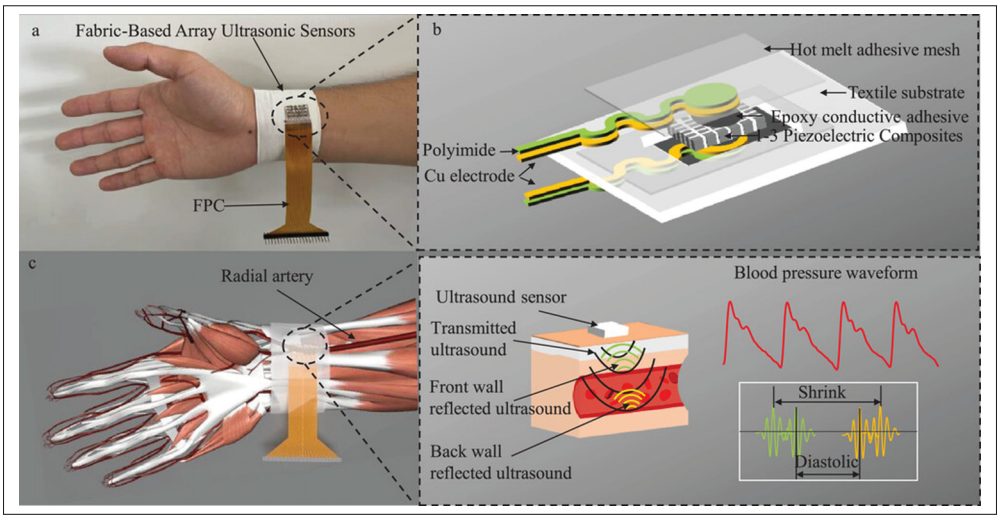

Figure 1.10 a) The FAUS is integrated into the wristband and is worn on the arm to measure radial artery blood pressure. b) Schematic diagram of the structure of FAUS. c) FAUS monitors blood pressure waveforms by capturing the pulsating vessel diameter of the radial artery using a pulse-echo method. Taken from author Li et al. (2023)

When comparing the performance of these devices, one of the most important parameter is the acoustic impedance which signifies the transmission efficiency due to losses at the material boundary. In the studies conducted by (Li et al. (2023); Peng et al. (2021a); Wang et al. (2018)), all reported acoustic impedance of around 15.3 MRayl. This is due to the fact all of the fabricated transducers utilized piezoelectric material (PZT-5H) and filling materials with similar acoustic impedance as well as the filling factor of around 50%. It should be noted that all the transducers were encapsulated with different materials which affects the net mismatch of acoustic impedance and more importantly affect the comfort and conforming ability to the skin for more accurate measurement. (Wang et al. (2018)) spin coated a thin layer of silicon on top of the ecoflex substrate to eliminate any air gaps and need for any gel during application, (Peng et al. (2021a)) did not use any conforming layer on top of the PDMS encapsulation and relied on using gel during measurements, restricting the long term usability. On the other hand (Li

et al. (2023)) reported using hot-melt adhesive mesh on top of the transducer to bond it with the fabric. They also compared comfort at the measurement site with ecoflex based device and reported significantly lower skin irritation due to better air permeability. Encapsulation material and filling material also affects the overall damping of the transducer which affects its overall bandwidth. Devices with softer materials like Ecoflex and silicon (Wang et al. (2018)) reported lower bandwidth compared to PDMS (Peng et al. (2021a)) (32.0 % vs 47.6% -6dBm bandwidth).

Axial resolution is determined by the absolute bandwidth of the device which is based on the resonance frequency and fractional bandwidth. Highest axial bandwidth was reported by (Li et al. (2023)) followed by (Wang et al. (2018)) and (Peng et al. (2021a)) at 330 um, 400 um and 490 um respectively. Highest penetration was reported by (Li et al. (2023)) followed by (Wang et al. (2018)) and (Peng et al. (2021a)) at 50mm, 40mm um and 20 um respectively. Lowest error is reported by (Peng et al. (2021a)) and (Li et al. (2023)) ≈ (Wang et al. (2018)).

1.4.2 PMUTs (Piezoelectric Micromachined Ultrasonic Transducers)

1.4.2.1 Non-flexible substrate based devices

Non-flexible PMUT platforms have begun to close the gap between laboratory prototypes and truly wearable BP monitoring systems by introducing MEMS-level integration and low-drive voltages. One of the first studies which introduced PMUTs for BP monitoring was done in 2022 (Pen et al. (2022)) using AlN PMUTs with a footprint of only 3 mm * 3 mm for each array implanting it beneath the skin of an ambulatory sheep (Figure. 1.11). In vitro study revealed very high resolution of artery diameter change at around 2.3 μm. The measurements were done on the brachial artery and experiments showed a linear relationship between artery diameter and blood pressure. The PMUTs array is based on the AlN thin film structure fabricated from a micromachined cavity-SOI process with a 5 um-thick Si elastic layer encapsulating the array.

The same technology of PMUT was used by Zhou et. al (Zhou et al. (2023a)), where they implimented the PMUT chip in strap like bracelet (Figure. 1.12). The radial artery is chosen for

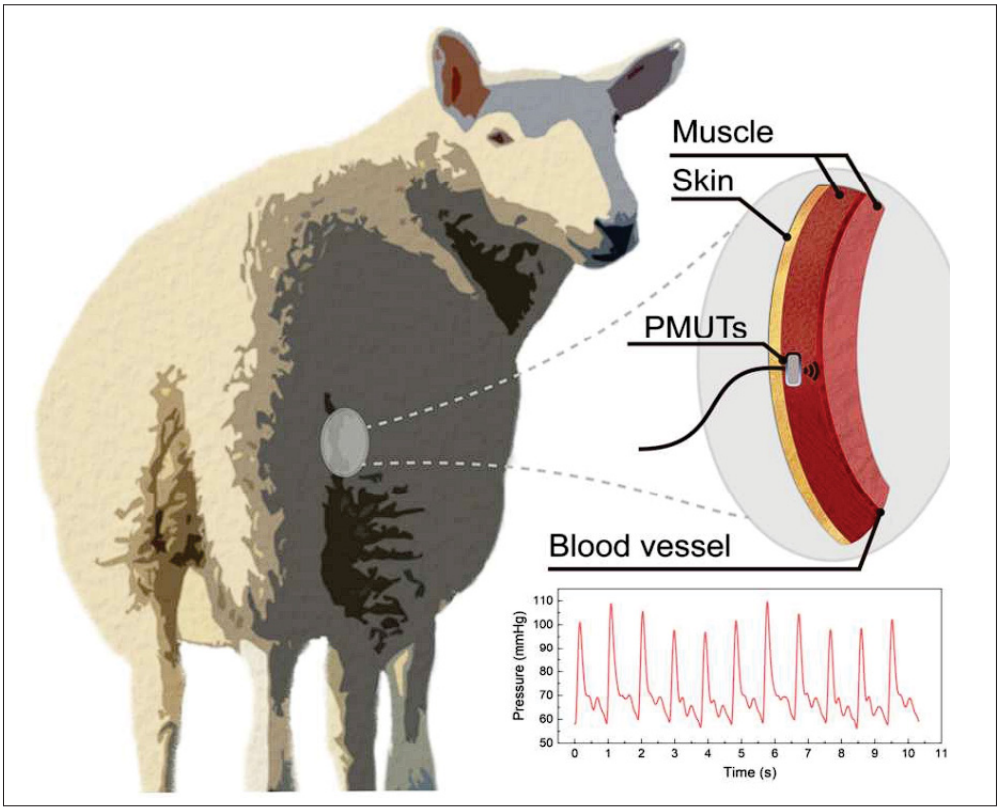

Figure 1.11 Representation of PMUT based device for blood pressure monitoring in ambulatory sheep
Taken from author Pen et al. (2022)

blood pressure monitoring for its ease of access and its ability to give specific cardiovascular status. The resonant frequency of 6.636 MHz was noted but the devices were operated at 5Mhz for good penetration. This study also used linear relationship to convert the artery diameter to blood pressure waveform assuming small change in diameter which was experimentally proven in in-vitro experiment. Calibration using BP cuff for values of slope and diastolic pressure were used to convert diameter waveform to BP waveform. When compared with a commercial ultrasonic probe, PMUT array showed excellent accuracy in arterial diameter measurement of 99.6%. It was also noted that it is important to maintain conformal contact between the device and the skin. The authors did not discuss the alignment of the device over the artery and possible interference due to misalignment. The work can greatly benefit by implementation of flexible electronics in the design, this can help make the device more portable and easy to apply.

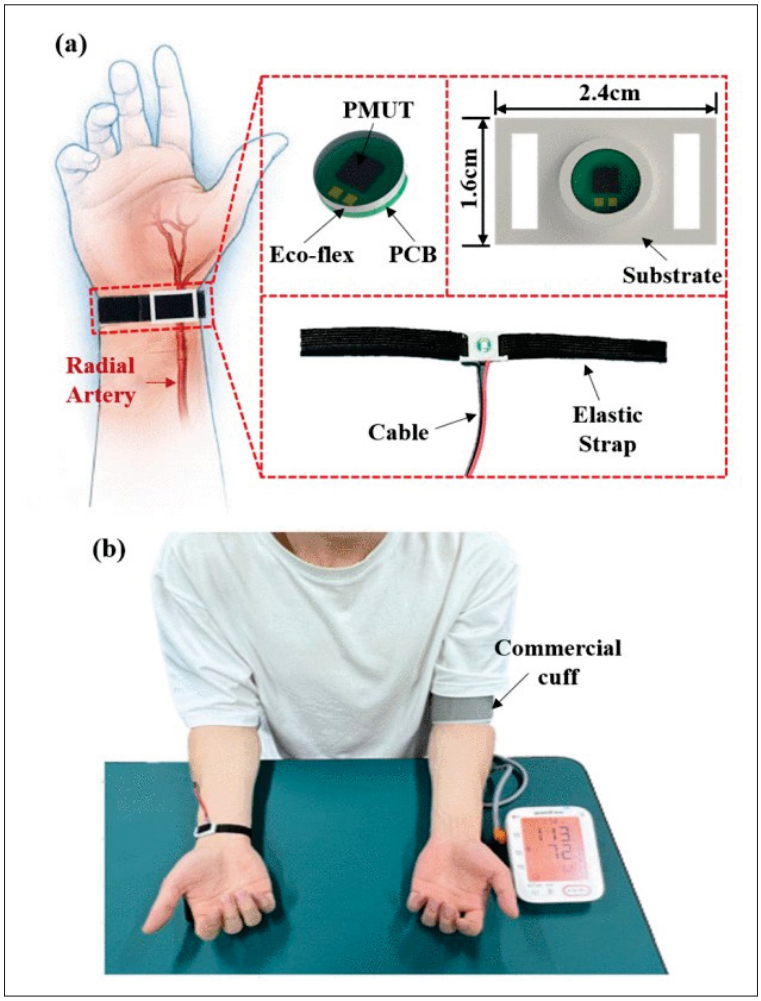

Figure 1.12 Schematic of wearable sensor
with a close-up detail of the device construction
Taken from author Zhou et al. (2023a)

Another study discussed AlN based PMUT for blood pressure waveform monitoring from the radial artery (Wu et al. (2023)). A hexagonal PMUT array device with high mechanical displacement sensitivity (24.47 nm/V at 5.94 MHz) and quality factor of 278 was created. (Fig. 1.13). A hexagonal array measuring 3 mm X 3 mm consisting of 91 elements was fabricated using surface micromachining process with element radius of 43 µm and fundamental resonance frequency of 6.47 MHz and 3.58 MHz in air and water respectfully. The hexagonal array improved impedance reduced the number of elements required compared to traditional square array. The fabricated device and signal processing system are shown in Fig. 1.14.

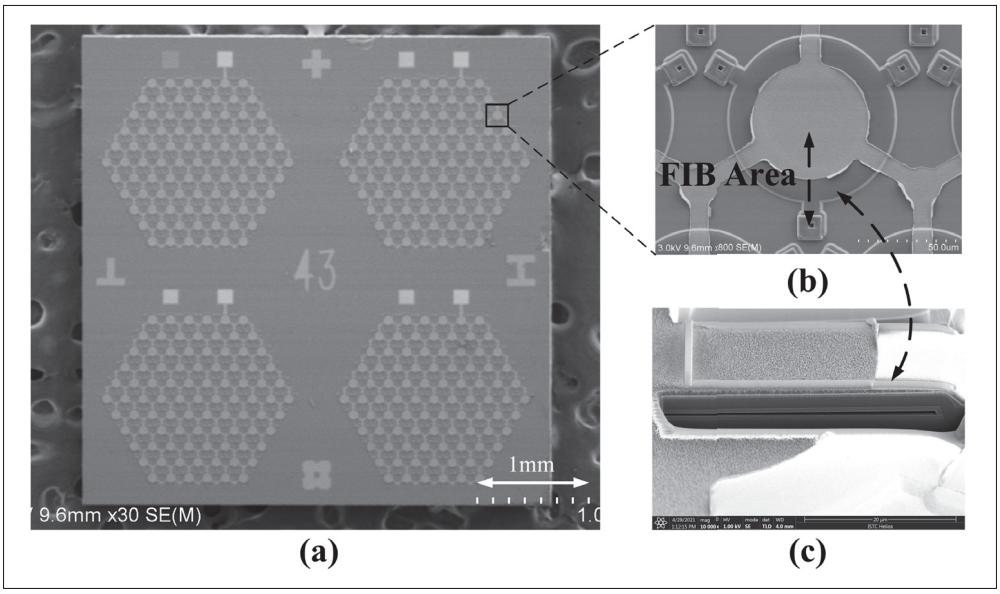

Figure 1.13 (a) SEM image of the fabricated PMUT chip with four arrays. (b) Enlarged view of a single PMUT unit. (c) Cross-sectional view of the PMUT structure via FIB cutting
Taken from author Wu et al. (2023)

The fabricated PMUT chip was wire bonded to a customized PCB, before being covered with epoxy adhesive for wire protection as well as electrical isolation from the environment. Human silica gel was then used to cover the device as an acoustic impedance matching layer, having low hardness and a similar density and acoustic speed to human tissue. In this study, the measured radial artery diameter change during the cardiac cycle was approximately 230 um and penetration depth of around 25 mm. Calibration using BP cuff for values of slope and diastolic

pressure. Using the PMUT device requires finger pressure on the PCB, which can lead to depth information signal jitter. The difference values of the upper and lower vessel wall depths, which represents the diameter change, are less effected by hand shaking and therefore more accurate. The presented device is proves the accuracy of methodology and serves as a proof of concept but the rigid device cannot be used for long term monitoring.

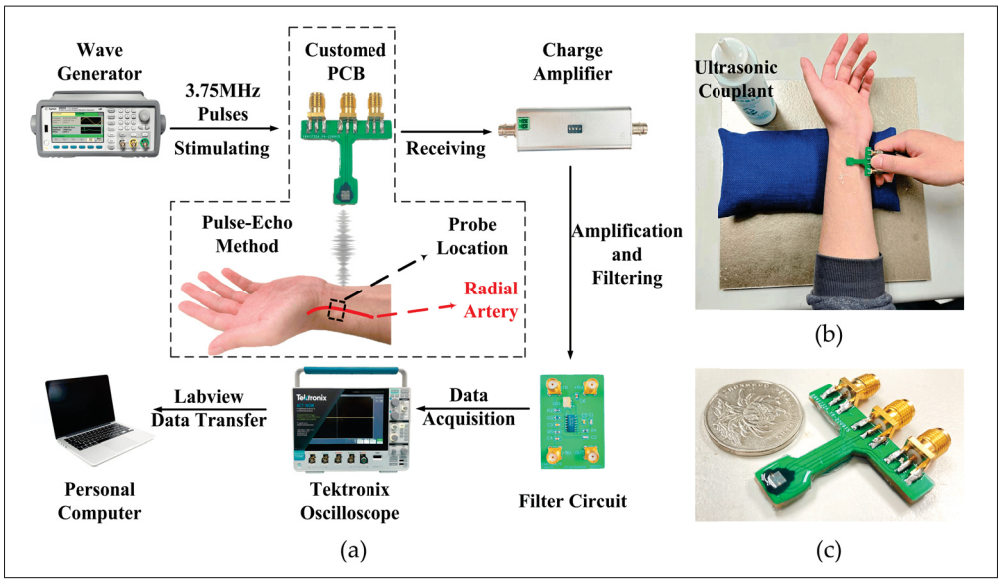

Figure 1.14 (a) Schematic of the pulse-echo detection signal transfer system. (b) Radial artery monitoring (corresponding to the dashed box in (a)). (c) Customized PCB for PMUT package and size comparison with a coin
Taken from author Wu et al. (2023)

This research presents a significant advancement in wearable medical technology through the development of a compact, low-power commercial PMUT array -based ultrasound system designed for continuous, non-invasive central blood pressure monitoring at the carotid artery. Utilizing a 32-channel PMUT linear array operating at 4.2 MHz, the device achieves ultrafast B-mode and M-mode imaging, facilitating precise measurement of arterial diameter and PWV without the need for calibration or traditional cuff-based methods. This approach first calculated the PWV of the artery, then using combined Bramwell-Hill Equation and exponential relationship determined the artery stiffness index (β). PWV and β was used to determine the diastolic blood

pressure. Then, the extracted variables were inputted in the exponential relationship again to determine the instantaneous blood pressure waveform. Experimental validation involving 12 subjects demonstrated the system's accuracy, with carotid artery blood pressure measurements closely matching expected physiological trends, being slightly lower (average differences of 4.5 mmHg in DBP and 5.9 mmHg in SBP) than radial artery values measured by commercial devices. These results highlight the considerable potential of PMUT technology to enable real-time, user-friendly wearable systems, significantly enhancing patient comfort, portability, and continuous cardiovascular monitoring capabilities. The system could measure arteries upto the depth of 6 cm.

Building on the increasingly sophisticated yet still non-flexible PMUT platforms (Yang et al. (2024)), pushed miniaturisation a decisive step further with a 64-element, 16 mm-wide PZT pMUT array fabricated on cavity-SOI and over-coated with PDMS for acoustic matching. Operating at 4.8 MHz with a drive voltage of only 9 V (about 2.8 times lower than a commercial clinical ultrasound probes), the array still maintains sufficient axial-wall velocity SNR to resolve diameter changes of 0.29 mm ± 0.06 mm with a bias of just 6 µm; the corresponding axial resolution is roughly 0.45 mm. It cleanly images the common carotid at typical neck depths of 20–50 mm, showing adequate penetration for superficial central arteries. Compared with the subcutaneous 3 × 3 mm AlN implant of (Pen et al. (2022)), the bracelet-style radial PMUT of (Zhou et al. (2023a)), the rigid hexagonal array of (Wu et al. (2023)), and the commercial 32-channel carotid system discussed earlier, Yang's design is the first to deliver a calibration-free, high-frame-rate pulse-wave-imaging pipeline—covering PWV, compliance, radius change, and local pulse pressure—with a MEMS platform small and low-voltage enough for a skin-mounted patch, thereby closing the final gap between laboratory prototypes and genuinely wearable, continuous, cuff-less blood-pressure monitors.

Collectively, these advancements illustrate a clear and cohesive trajectory toward practical MEMS-based ultrasonic wearables. Non-flexible PMUT platforms now routinely achieve low-voltage operation, cuff-free calibration, and clinical-grade haemodynamic metrics. However, their rigid construction remains the critical obstacle, repeatedly highlighted by alignment

sensitivity, coupling stability issues, and reliance on external electronics. Future developments must integrate conformal, hybrid flexible-rigid packaging, embed miniaturized electronics directly onto PMUT arrays, and conduct comprehensive validation in unsupervised, ambulatory scenarios. Addressing these remaining challenges will decisively transition PMUT technologies from laboratory prototypes into clinically meaningful, truly wearable devices for continuous, cuffless blood pressure monitoring.

1.4.2.2 Flexible devices

Zhou et al. (Zhou et al. (2025)) package a 23 × 26 AlN PMUT array (center frequency 6.8 MHz) inside a 22 mm × 16 mm × 6 mm wrist module that weighs 1.8 g; a soft Ecoflex lens lets the rigid silicon sit comfortably on skin is shown by fig. 1.15. It narrows the lateral beam to under 2.3 mm, shifts the acoustic focus to 16 mm, and still delivers more than 29 dB SNR with echoes detectable beyond 40 mm. Using two of these probes 16 mm apart, the system tracks diameter changes smaller than 1 mm, computes local PWV on every beat, and converts the result into blood-pressure waveforms with mean absolute errors of 2.6 mmHg (systolic) and 1.8 mmHg (diastolic); waveform correlations reach 0.998, and accuracy holds during hand-grip, cold-pressor, and Valsalva manoeuvres.

Xia et al. (Xia et al. (2025)) take an opposite route: they bond a much smaller 5 mm × 5 mm AlN bimorph array (5.6 MHz) to a semi-rigid PCB, then recover alignment errors electronically by steering the beam ±30° at 1.6 kHz; simulations and tests on a 16 mm-deep brachial artery show a 2 mm beamwidth, a four-fold wider field of view, and more than 70 % echo amplitude retention when the probe is misplaced by 5 mm, but the study reports only diameter pulsations (100 µm) and no pressure accuracy. This concept is represented by fig. 1.16.

In short, Zhou's soft-lens design already meets clinical blood-pressure targets yet still relies on 25 V drivers and a dual-probe layout, whereas Xia's steerable concept eases placement and shrinks the silicon footprint but has yet to prove blood-pressure accuracy and still uses benchtop electronics. Merging Xia's low-channel, alignment-tolerant steering with Zhou's

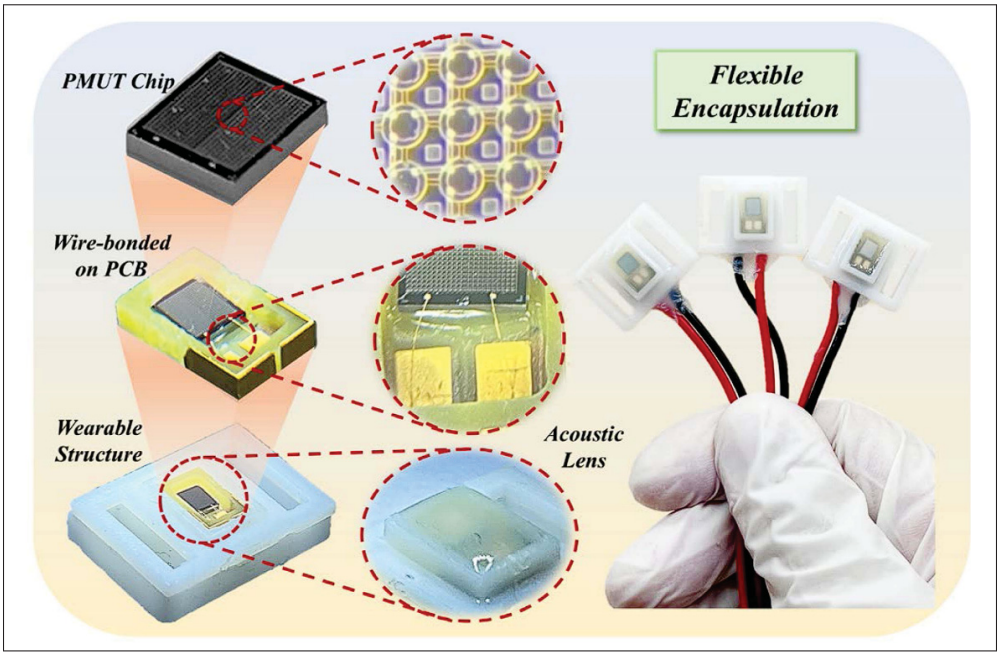

Figure 1.15 Representation of PMUT based flexible device
Taken from author Zhou et al. (2025)

high-SNR, gel-free encapsulation—while cutting the drive voltage and fully integrating the electronics—remains the key step toward a truly untethered, flexible PMUT patch for continuous, calibration-free blood-pressure monitoring.

In summary, the evolution from bulk piezoelectric through PMUTs to CMUTs illustrates a trajectory of miniaturization, power reduction, and integration. Bulk transducers established the physical principles and data-processing pipelines, PMUTs translated these into wearable form factors with progressively lower voltage and calibration needs, and CMUTs offer a fertile—but as yet underexplored—platform for monolithic, ultra-wide band, and CMOS-compatible BP waveform monitors.

Despite their imaging superiority, CMUTs have seen relatively little application in BP waveform monitoring. The spring-softening nonlinearity near pull-in voltage demands active bias stabilization, and the membrane's collapse behavior complicates linear pressure–voltage conversion. To date, no published study has demonstrated a wearable CMUT-based BP monitor analogous

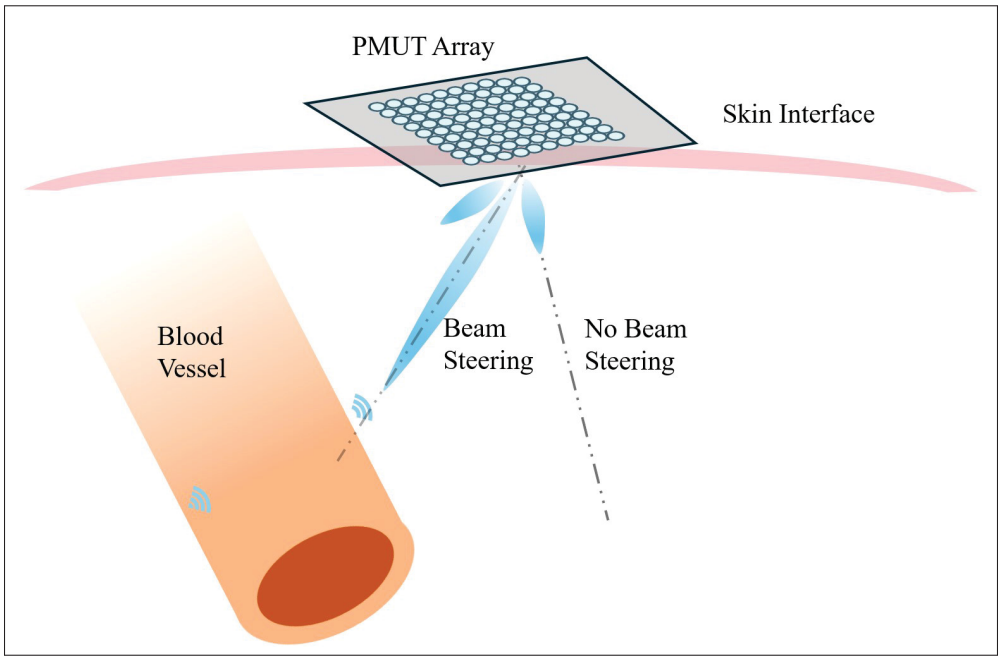

Figure 1.16 Representation of beam steering of ultrasound pulse by a PMUT based device
Taken from author Xia et al. (2025)

to the PMUT examples above. This gap highlights opportunities for future research: flexible CMUT membranes on polymer substrates for conformal skin attachment; integrated bias-control and front-end electronics for stable operation near collapse; and refined mechanical models that linearize membrane response across physiological pressure ranges.

1.5 Critical review and Future Directions

Table 1.3 and 1.4 gives a review of the performance of various ultrasound-based blood pressure waveform systems. The table compared different systems based on but not limited to the blood pressure model used, error in measurements compared to commercial devices, fabrication method (MEMS/non-MEMS) and its ability to conform to the human skin (Flexible/non-Flexible).

Various blood pressure models were discussed including the Bramwell-Hill equation, the exponential relationship, the linear relationship, the 1-D artery model, Joukowsky's equation and the Laplace law + MK equation. Of all previous research discussed in this review, blood pressure

waveform monitoring systems based on Exponential relationship have shown to have the highest accuracy compared to commercial blood pressure tools (Peng et al. (2021a); Wang et al. (2018)). It should also be noted that both devices were based on 1-3 piezoelectric composites and were flexible.

The blood pressure model to be used depends on the arterial site of interest. This is because central blood pressure and carotid artery diameter (neck) follow a mostly linear relationship due to its higher elasticity, while peripheral blood pressure in the diameter of the radial (wrist) or ular (forearm) artery follows a mostly exponential relationship due to saturation at near-systolic pressure (Seabra, Belén Amado Rey, Seabra, Carolina, da Silva, Rey, Belen, Seabra, Silva, Stieglitz, Member, Amado-Rey & diastolic systolic (2017)).

Table 1.3 Performance of Ultrasound-Based Blood-Pressure Waveform Systems (Part 1 of 2)

No.	Description	Advantages	Limitations	Calibration	Error Metric	BP Model	Site (Fig. 1.4)	MEMS?	Notes	Year	Flex	Ref.
1	BP waveform using two–element ultrasound system	Inexpensive; portable	Synchronization errors; skill required; not wearable	BP cuff	Scaling error $-1.56 \pm 14\,\%$	Bramwell–Hill	C	Non-MEMS (bulk)	Flow–area Doppler PWV	2015	No	Seo et al. (2015b)
2	Flexible piezo-composite sensor	Flexible; wearable	Gel needed; short-term	BP cuff	SBP/DBP < 1%	Exponential	H	MEMS (1–3 piezo)	—	2021	Yes	Peng et al. (2021a)
3	ToF + shear-wave elastography	Accounts for physiology	Alignment needed; no in-vivo validation	BP cuff	—	Linear	A	Non-MEMS (bulk)	Method only; no waveform	2021	No	Beyaz (2021)
4	Wearable PMUT array	Small; accurate	Motion artefacts	BP cuff	< 5 mmHg; 0.4% diam.	Linear	A	MEMS (AlN PMUT)	Artery-tracking suggested	2023	No	Zhou et al. (2023a)
5	Pulse-pressure (3-elem.)	Better PWV accuracy	Alignment; assumptions; not wearable	Volume clamp	PP 2.83 ± 0.04 mmHg; $r = 0.978$	Bramwell–Hill	C	Non-MEMS (bulk)	PWV via 3-transducer timing	2023	No	Xu et al. (2023)
6	Hexagonal AiN PMUT array	Low impedance; fewer elements	Oversimplified artery; not wearable	BP cuff	—	Linear	A	MEMS (AlN PMUT)	No in-vivo validation	2023	No	Wu et al. (2023)
7	ML BP estimation	Repeatable; no calibration	No waveform; not real-time	—	-2.84 mmHg (SBP); -0.88 mmHg (DBP)	CNN	A	Non-MEMS (bulk)	Piezo impulse → ML	2022	Yes	Li et al. (2022a)
8	Wearable haemodynamic patch	Wearable; multi-param.	Needs flexible MEMS for best match	BP cuff	—	Exponential	C	Non-MEMS (bulk)	Also lactate, glucose etc.	2021	Yes	Sempionatto et al. (2021)
9	Conformal ultrasonic device	Stretchable; self-aligning	Needs MEMS array for power	BP cuff	0.05 mmHg (SBP); 0.28 mmHg (DN)	Exponential	C	MEMS (1–3 piezo)	Phased array beam steering	2018	Yes	Wang et al. (2018)
10	Portable COTS system	Cheap; off-the-shelf	Not wearable	BP cuff	RMSE 4.9–17.5 mmHg	Bramwell–Hill	—	Non-MEMS (bulk)	Doppler flow-area PWV	2015	No	Seo, Pietrangelo, Lee & Sodini (2015a)
11	Motion-tolerant BP	Cheap; usable in motion	Not wearable	BP cuff	Flow error 2.66%	Bramwell–Hill	—	Non-MEMS (bulk)	Doppler + image declutter	2018	No	Seo, Pietrangelo, Sodini & Lee (2018)

Table 1.4 Performance of Ultrasound-Based Blood-Pressure Waveform Systems (Part 2 of 2)

No.	Description	Advantages	Limitations	Calibration	Error Metric	BP Model	Site (Fig. 1.4)	MEMS?	Notes	Year	Flex	Ref.
12	Valsalva tolerant BP	Cheap; tracks hemodynamics	Not wearable	BP cuff	RMSE 7–13.9 mmHg	Bramwell–Hill	C	Non-MEMS (bulk)	Doppler + image declutter	2021	No	Seo et al. (2021)
13	PZT arterial pulse	Portable; wearable	Arm posture sensitive	BP cuff	—	Piezo dynamics	A	MEMS (PZT)	Three correlation modes	2022	Yes	Yi et al. (2022)
14	MPG + US PP (no calib.)	Sync PWV+diameter	Only PP, no waveform	—	—	Bramwell–Hill	C	Non-MEMS (bulk)	MPG PWV + US diameter	2016	No	Joseph et al. (2016)
15	US images → waveform	Any site; cheap w/ clin. US	Not real-time; not portable	BP cuff	MAD −1.33 ± 6.55 mmHg	Joukowsky	C	Non-MEMS (imaging)	Sonograms for waveform	2017	No	Soleimani et al. (2016)
16	Ultrasound manometry	No transfer fn.	Not wearable; no waveform	—	r = 0.94–0.98 vs tonometer	Laplace+MK	G	Non-MEMS (imaging)	Wall disp. + PWV	2011	No	Vappou et al. (2011)
17	Commercial NDT probe	Cheap; COTS	Underestimates BP	BP cuff	SBP 89 vs 136 mmHg	Laplace+MK	A	Non-MEMS (probe)	Diameter + PWV	2016	No	Worthing (2016)
18	Aortic BP via PWV	Very accurate alg.	Not portable	BP cuff	SBP 1.4±0.8; DBP 0.9±0.8 mmHg	Bramwell–Hill	C	Non-MEMS (probe)	Aortic flow + diameter + tonometer	2024	No	Zhou et al. (2024)
19	QA PWV PP	Real-time; any diameter	Image quality dependent	—	r = 0.997–0.999 vs catheter	Bramwell–Hill	C	Non-MEMS (probe)	Flow-area (QA) method	2023	No	Ng et al. (2023)
20	Fabric ultrasonic sensor	Continuous; breathable	Limited depth for some configs	BP cuff	±2 mmHg vs cuff	Exponential	A	Non-MEMS (1–3 piezo)	Stretchable fabric electrodes	2023	Yes	Li et al. (2023)
21	EcoFlex based AlN PMUT	Conformal; high accuracy	Not breathable; dual probe layout	BP cuff	Corr. 0.998 with PPG; SBP ±2.6 mmHg; DBP ±1.8 mmHg vs cuff	Exponential	A	MEMS (AlN PMUT)	Rigid substrate; soft encapsulation	2025	Yes	Zhou et al. (2025)
22	Fabric ultrasonic sensor	Beam steering; breathable	Limited depth for some configs	BP cuff	±2 mmHg vs cuff	Exponential	A	Non-MEMS (1–3 piezo)	Stretchable fabric electrodes	2023	Yes	Xia et al. (2025)
23	Subcutaneous BP monitoring in sheep	Continuous	Rigid; invasive	BP cuff	—	Exponential	B	MEMS (AlN PMUT)	Proof-of-concept study in sheep	2023	No	Pen et al. (2022)
24	Calibration-free PMUT for BP monitoring	Continuous; conformal	Rigid; not breathable	Calibration free	Axial resolution < 0.45 mm	Exponential & Bramwell-Hill	B	MEMS (PZT PMUT)	No cuff needed for calibration	2024	No	Yang et al. (2024)

1.5.1 Challenges and Limitations

These devices can suffer from noise and artifacts that result from movements of the patient or misalignment of the sensor and the targeted artery, which can lead to false results. Such problems can be solved using MEMS based devices that are wearable and flexible for long-term assessment without providing discomfort to patients. MEMS based devices can also be cheaper and easily replaceable.

Although many studies have explored bulk non-MEMS transducers, a noticeable gap in the literature is evident when it comes to using flexible MEMS based ultrasonic transducers such as PMUTs and CMUTs. These devices can offer several advantages over bulk non-MEMS piezoelectric devices, such as miniaturization, broad frequency response, and lower acoustic impedance. Their implementation can reduce the cost and energy required for operation (He et al. (2022)). Flexible devices can conform to the physical features of skin and maintain good contact for more accurate results. It is also important to use biocompatible materials during the fabrication of the device. PZT is a widely used piezoelectric material, but it contains lead, which is toxic and can cause adverse effects after repeated exposure. Lead-free materials like ZnO, AlN, and PVDF can be used for making MEMS piezoelectric sensors.

It is widely known that central blood pressure gives a better estimate for assessing cardiovascular risks, but peripheral blood pressure can also be used when more convenient. Measurement of central blood pressure is of clinical interest for health assessment. It should also be noted that the significant differences between central blood pressure and peripheral blood pressure provide important diagnostic information. This is a result of the great variation in artery stiffness between the two sites. Therefore, for a complete blood pressure monitoring system for diagnostics, it is important to measure blood pressure waveform from both the sites.

One of the shortcomings in this field of research is the lack of standardized testing and validation procedure for non-invasive blood pressure waveform. The gold standard for the evaluation of the blood pressure waveform is the use of arterial catheterization usually in the radial artery or the femoral artery (groin). It is important to validate the waveform obtained from the ultrasound

system with the waveform obtained from arterial catheterization to improve the design and accuracy. This can also lead to faster implementation of non-invasive systems in clinical settings.

Implementation of arrays with artery detection capabilities can bypass the need for alignment. Artery detection can be implemented by using signals from only those elements that have the best signal integrity and quality. This feature can make putting the device on the skin a relatively low-skill operation. After proper validation and testing of the device, it is possible to apply this technology in already commercial devices such as smart watches. Beam forming can be done using an array for increased spatial resolution and depth of field as well as reduced noise and artifacts.

Currently most ultrasound-based non-invasive blood pressure monitoring systems require calibration using a blood pressure cuff and to get a baseline diastolic pressure. For long-term monitoring, multiple calibrations need to be done to get accurate results, this makes the whole procedure complicated and can result in errors. Some research has been done on extracting SBP and DBP using piezo-arrays using machine learning. Integrating similar technology in the flexible and wearable blood pressure monitoring system could be interesting. This integrated system can run autonomously without the need for an external calibration device and makes for a truly wearable blood pressure waveform monitoring system.

Overall, the present research proves that non-invasive blood pressure waveform monitoring is of great interest and of practical importance from a medical point of view. The research presented provides insight into our current understanding of technology. Implementing this technology in our medical systems will require more research and validation. Collaboration between multidisciplinary teams, incorporating expertise from engineering and medicine, will be essential. By collectively addressing current shortcomings and concerns, we can usher in an era of more accessible, accurate, and patient-friendly blood pressure waveform monitoring systems, ultimately contributing to improved cardiovascular health outcomes.

1.5.2 Future Directions

Continued research into advanced sensor technologies, such as piezo arrays and MEMS-based ultrasonic transducers such as PMUTs and CMUTs, offers great potential. These innovations could improve miniaturization, sensitivity, and signal quality. Integrating these cutting-edge sensors into wearable devices could make blood pressure monitoring more accurate and user-friendly.

Using machine learning algorithms for real-time signal processing and extraction of blood pressure parameters is a promising direction. Incorporating these capabilities into wearable monitors can enable autonomous operation, reduce the dependency on external calibration devices, and improve overall user convenience.

Collaboration between engineers and medical professionals is crucial to translate research into clinically viable solutions. Partnerships with healthcare providers and regulatory agencies can facilitate the integration of non-invasive blood pressure waveform monitoring into routine clinical practice, making these advanced technologies more accessible to patients.

Large-scale longitudinal studies are essential to evaluate the effectiveness and reliability of these monitoring systems in real world settings. These studies will provide valuable insight on device performance, patient outcomes, and clinical utility, helping to refine and optimize these technologies for better patient care.

Ensuring the long-term performance and durability of non-invasive blood pressure monitoring devices is critical. Future research should focus on how these devices perform for extended periods under various environmental conditions and across diverse patient populations. Understanding their longevity and consistency will be key to their success in continuous monitoring applications.

Ensuring that non-invasive blood pressure monitoring technologies are accessible to all is vital for addressing global healthcare disparities. Focusing on affordability, scalability, and user-friendliness in device design and distribution will help extend the benefits of these innovations to underserved populations around the world.

The field is rapidly evolving with emerging trends and innovations, such as the integration of flexible electronics, the development of hybrid sensor systems, and the use of new materials that improve sensor performance. Keeping abreast of these trends will help drive future research and development, ensuring that non-invasive blood pressure monitoring remains at the forefront of medical technology.

In conclusion, non-invasive blood pressure waveform monitoring has the potential to revolutionize cardiovascular health assessment. Achieving this potential requires ongoing innovation, interdisciplinary collaboration, and a commitment to addressing current challenges. In doing so, we can create accessible, accurate, and patient-friendly monitoring systems that improve cardiovascular outcomes worldwide.

1.6 Conclusion

It is clear that MEMS based ultrasound sensors have the potential to be used for flexible and wearable non-invasive blood pressure waveform monitoring system. MEMS based ultrasonic transducers have several advantages, including low power consumption, good sensitivity, miniaturization, flexibility, and low cost. The current systems face several challenges. Some of these challenges are lack of standardized validation with clinically accepted BP waveform techniques, bulky and non-wearable systems, requirement of frequent calibration, and lack of MEMS implementation in the systems. Not much research has been done on the implementation of MEMS in non-invasive blood pressure waveform monitoring systems. Solutions and future directions for research in the field have been provided in the literature for the issues faced by current systems. However, more research is still needed to solve these issues.

CHAPTER 2

A METHOD FOR EXPANDING THE BANDWIDTH AND DECREASING THE ACTUATION VOLTAGE OF CMUT DEVICES

Chirag Goel[1,4], Mathieu Gratuze[1,4], Alexandre Robichaud[3,4], Ricardo Izquierdo[1,4], Paul-Vahé Cicek[2,4]

[1] Département de Génie Électrique, École de Technologie Supérieure,
1100 Rue Notre-Dame Ouest, Montréal, Québec, H3C 1K3, Canada
[2] Université du Québec à Montréal (UQAM), Montreal, Canada
[3] Université du Québec à Chicoutimi (UQAC), Chicoutimi, Canada
[4] Regroupement stratégique en microsystèmes du Québec (ReSMiQ), Montréal, Québec, Canada

Article publié dans la revue
« IEEE sensors letters»
le 26 August 2025.
https://ieeexplore.ieee.org/abstract/document/11141753/

Résumé: Cet article présente un nouveau transducteur ultrasonore micromachiné capacitif (CMUT) fabriqué avec le procédé PolyMUMPs de MEMSCAP et intégrant deux nouveaux éléments de conception : des bras ressorts et des tiges basculantes (rocker stems). Cette structure permet un fonctionnement à faible facteur de qualité (Q) et à large bande passante dans une technologie de micro-usinage de surface commerciale, ce qui la rend adaptée aux applications à couplage dans l'air. Le dispositif fonctionne avec une tension de polarisation aussi faible que 26 V, ce qui est avantageux pour les systèmes portables. La caractérisation électrique montre une réduction par un facteur (6,5X) de la tension de polarisation par rapport aux conceptions traditionnelles. Quatre CMUT ont été fabriqués afin d'isoler et d'évaluer l'influence de chaque élément de conception. Les spectres de fréquence ont montré que le dispositif intégrant les nouvelles caractéristiques présentait la bande passante la plus large (un facteur de qualité (Q) d'environ 1,2 contre environ 34 pour la conception traditionnelle). Ces résultats mettent en évidence le potentiel de l'architecture de CMUT proposée pour des systèmes pulse–écho à haute résolution axiale.

Abstract: This paper presents a novel capacitive micromachined ultrasonic transducer (CMUT) fabricated with the MEMSCAP PolyMUMPs process and incorporating two new design elements: spring arms and rocker stems. The structure enables low-Q-factor, broadband operation in a commercial surface-micromachining technology, making it suitable for air-coupled applications. The device operates at a bias voltage as low as 26 V, which is advantageous for portable systems. Electrical characterization demonstrates a 6.5× reduction in bias voltage compared with traditional designs. Four CMUTs were fabricated to isolate and assess the influence of each design element. The frequency spectra showed that the device with the novel design features had the broadest bandwidth (a Q-factor of approximately 1.2 compared to approximately 34 for the traditional design). These results highlight the potential of the proposed CMUT architecture for high axial resolution pulse-echo systems.

Keywords: CMUT, broadband, low-voltage operation, spring arms, rocker supports, Ultrasound.

2.1 Introduction

Capacitive micromachined ultrasonic transducers (CMUTs) present a compelling alternative to traditional piezoelectric film-based transducers, offering advantages such as broader bandwidth, heightened sensitivity, improved performance, compatibility with integrated circuit fabrication, and flexible array configurations (Munir, Ain & Lee (2019)). There have been significant advancements in ultrasound applications using CMUT technology (Salim, Abd Malek, Heng, Juni & Sabri (2012)), particularly in the miniaturization of volumetric imaging devices for *in-vivo* applications, including intravascular imaging and surgical guidance (Demirci, Ergun, Oralkan, Karaman & Khuri-Yakub (2004); Oralkan, Ergun, Cheng, Johnson, Karaman, Lee & Khuri-Yakub (2003a)). For portable ultrasonic devices, keeping the bias voltage low is essential for safety, portability, and cost. A reduced pull-in voltage also lets the CMUT operate at its optimal pre-collapse bias with standard low-voltage electronics, maximizing transduction efficiency while remaining in the linear regime, because electromechanical coupling peaks just below collapse. In CMUTs, a fundamental design trade-off exists: reducing the bias voltage typically leads to a lower resonance frequency. However, because the resonance frequency must be tailored to meet the demands of specific ultrasonic applications, there is limited flexibility to adjust the bias voltage through design alone. This constraint is particularly evident in standard, commercially available surface-micromachining technologies such as MEMSCAP PolyMUMPs (Tawfik, Alsaiary, Elsayed, Nabki & El-Gamal (2019b)). Furthermore, to improve imaging resolution in pulse-echo mode, it is desirable to increase CMUT bandwidth as this narrows the transmitted pulse and, therefore, helps improve the achievable axial depth resolution. In recent years, there have not been many studies focused on fine-tuning CMUT bandwidth, which is generally not trivial to achieve through device geometry alterations (Liang, Li & Zhang (2020)). To address these two challenges, this study explores the design, fabrication and characterization of three novel CMUT topologies aiming to operate at extremely low bias voltage while exhibiting broad bandwidth. The proposed devices are compared with a control baseline (traditional) CMUT device.

2.2 Operating Principle

CMUT devices need to perform two primary functions: transmitting and receiving ultrasonic waves. In transmission, the plate vibrates due to the time-varying electrostatic force produced by an applied AC potential, generating an acoustic wave. In reception, the plate vibrates due to an incident acoustic wave, inducing a time-varying electric current at the terminals of the device. Both modes rely on the application of a DC bias voltage between the plate and bottom electrode to form an electrostatic field and thus pre-strain the plate downward. Indeed, the greater the DC bias, the stronger the device to both the transmited and the received acoustic signals. However, the plate collapses onto the bottom electrode if the DC bias voltage exceeds the pull-in voltage, which can be expressed as

$$V_{\text{pull-in}} = \sqrt{\frac{8k_{\text{eff}}g^3}{27\varepsilon A}}, \tag{2.1}$$

where g is the gap distance, A is the plate area, and k_{eff} is the effective stiffness. Reducing the pull-in voltage therefore requires decreasing either the structural stiffness or the initial size of the gap. However, lowering stiffness also reduces the resonant frequency, which can be expressed as

$$f_{\text{res}} = \frac{1}{2\pi}\sqrt{\frac{k_{\text{eff}}}{M_{\text{total}}}}, \tag{2.2}$$

where M_{total} is the mass of the plate. The ability to set f_{res} to a targeted value is crucial as it determines application suitability. The air gap separating the plate and the electrode influences power transduction efficiency and thus sensitivity. The Q-factor and the bandwidth (Δf) are related inversely proportional, such that

$$Q = \frac{f_{\text{res}}}{\Delta f}. \tag{2.3}$$

In the proposed CMUT designs of this work, k_{eff} reduction is achieved through the introduction of spring arms, to increase plate electrostatic displacement efficiency and allow for a significant reduction in resonant frequency for a similar footprint. Furthermore, the introduction of free

Table 2.1 CMUT topologies and characterization at 26 V_{pp}

Topology	Connecting Arm	Anchoring	Gap (µm)	V_{dc} (V)	Resonant Frequency (MHz)	Q Factor	Pull-in Voltage (V)
CMUT A	Spring arm	Rocker support	0.75	26	0.45	1.54 - 1.18 (10 V_{dc} - 26 V_{dc})	40
CMUT C	Straight arm			70	1.52	4.5 - 3.2 (10 V_{dc} - 70 V_{dc})	106
CMUT B	Spring arm	Fixed anchoring	2	70	0.88	11.2 - 8.9 (10 V_{dc} - 70 V_{dc})	160
CMUT D	Straight arm			70	4.5	36.9 - 34.9 (10 V_{dc} - 70 V_{dc})	260

rocker support stems allows for a Q-factor reduction, hence a larger bandwidth for the same device dimensions.

2.3 Methods

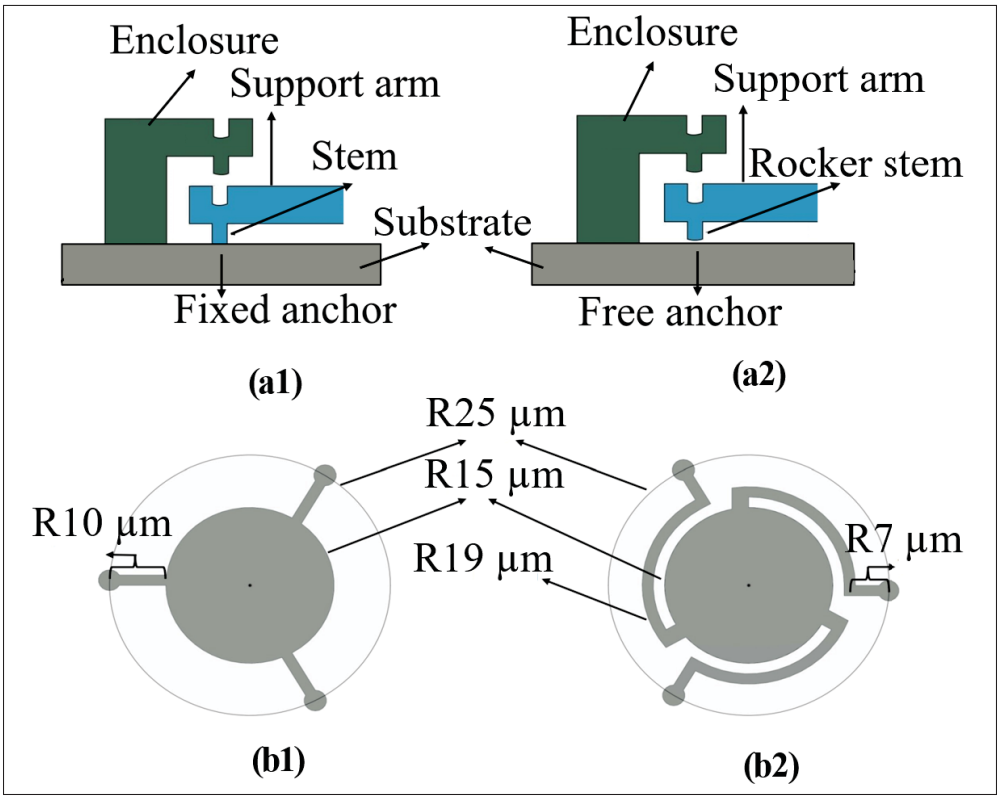

Figure 2.1 CMUT dimensions and design features

Three CMUT topology configurations are studied and compared to a control baseline to evaluate the effects of spring-arm geometry and anchoring method on device performance. As shown in Fig. 2.1, configuration types are determined both by the anchor type (either *fixed—configuration a1* or *free—configuration a2*) and the connecting arm type (*straight—configuration b1* or *spring—configuration b2*). As such, the device combining the two novel features (both free anchors and spring arms) is dubbed CMUT A. CMUT B features spring arms but fixed anchors, whereas CMUT C features free anchors but straight arms. The control baseline (traditional) device with fixed anchors and straight arms is called CMUT D. In Fig. 2.1, the sub-figures a1 and a2 represent the side view schematic of the device and b1 and b2 represent the top view.

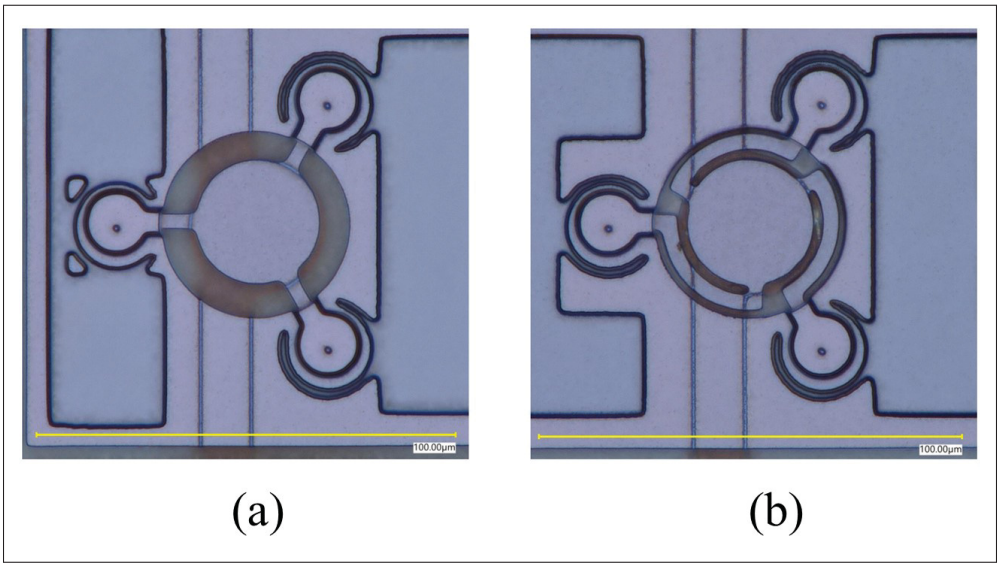

Figure 2.2 (A) Fabricated cell of CMUT A & B. (B) Fabricated cell of CMUT C & D.

When a DC bias is applied, the electrostatic force pulls the plate toward the electrode, causing the connecting arms to bend. It should be noted that the connecting arms and the anchors are just an extension of the plate fabricated with the same layer (Poly 1) with PolyMUMPS. The connecting arms and the plate is electrically connected to the electrode below by means of mechanical contact through the anchors (Rocker support and fixed anchoring). For CMUT A and C, the free rocking support stems may slide on the underlying layer and pivot about a small point or edge at their base, enabling a rocking motion. Static COMSOL simulations of CMUT A show that,

under a 40 V DC bias, the normal (vertical) reaction force F_{normal} and the radial outward force F_{radial} are 1.6 µN and 0.28 µN, respectively. With a minimum static friction coefficient μ of 0.2 between silicon compounds (Keren Deng & Wen (1992)), the frictional force μF_{normal} exceeds F_{radial}, ensuring that the rocker stem remains stationary and eliminating excessive energy loss through friction and wear during static operation. This configuration directs more energy into plate displacement than conventional fixed-stem designs. The reduced effective stiffness of the spring arms also lowers the resonance frequency for a comparable device footprint.

Rocker support as anchors allow for reduced gap compared to fixed anchoring because the feature is reactive ion etched partially into the first oxide layer unlike the fixed anchor which is completely etched through the oxide layer. The complete fabrication sequence of the devices with the MEMSCAP PolyMUMPs process is extensively explained in (Goel, Cicek & Robichaud (2022c)). Fig. 2.2 shows the top views of the fabricated CMUT devices. Fig. 2.2(a) depicts CMUT A and CMUT B, while Fig. 2.2(b) presents CMUT C and CMUT D.

2.4 Characterization and Results

Device operation was characterized at room temperature under air-coupled conditions using a Polytec MSV-300 Laser Doppler Vibrometer (LDV) (Polytec PI Inc., Auburn, MA), as shown in Fig. 2.3. It should be noted that the devices have non-sealed cavity. Velocity spectra were acquired for the four fabricated CMUT devices. CMUT A was biased from 10 V_{dc} to 26 V_{dc}, while CMUTs B, C, and D were biased from 10 V_{dc} to 70 V_{dc} in steps of 20 V. All CMUTs were excited with a sinusoidal signal ranging from 10 V_{pp} to 20 V_{pp}, sweeping frequencies from 200 kHz to 4 MHz, with a sampling frequency of 10.6 MHz. The velocity spectra were converted to Power Spectral Density (PSD) plots using MATLAB. For CMUTs B, C, and D, the bias voltage was limited to 70 V_{dc} to prevent pull-in. The measured frequency response of CMUTs A, B, C and D are shown in Figure 3.3.

For CMUT A, an increase in bias voltage resulted in a resonant frequency shift from 0.45 MHz at 10 V_{dc} to 0.442 MHz at 26 V_{dc}, attributed to spring softening. This was accompanied by a

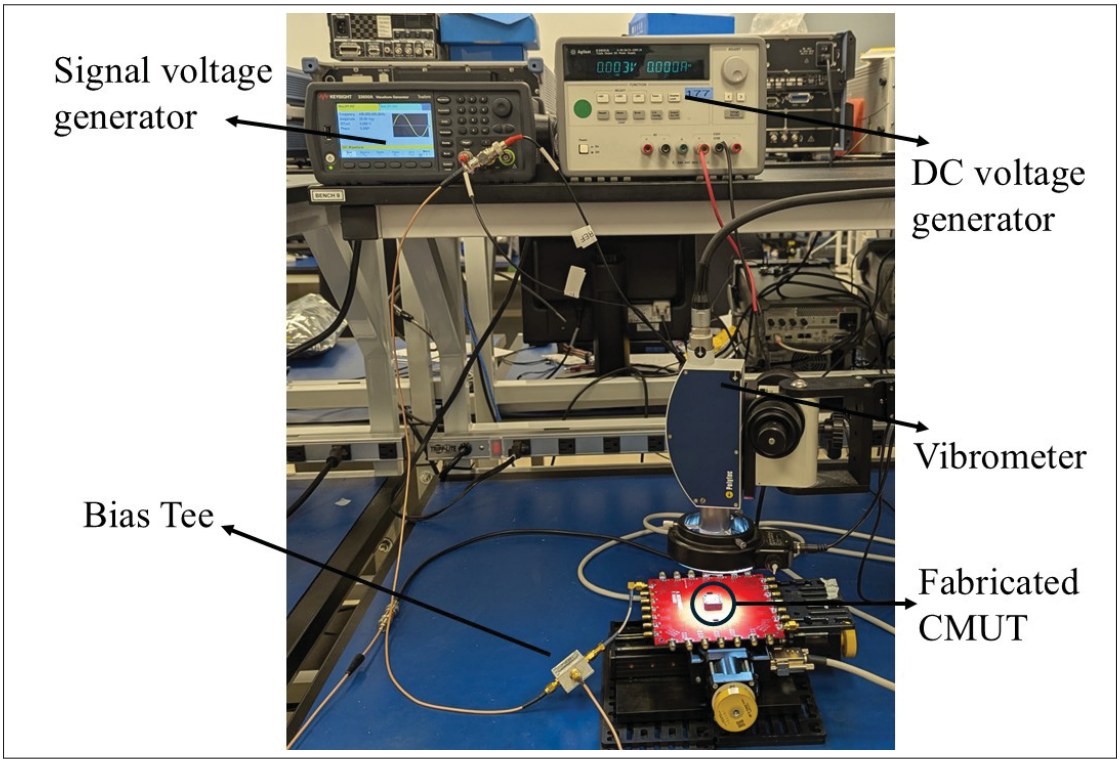

Figure 2.3 Vibrometer test setup

reduction in the Q-factor, from 1.54 to 1.18. The pull-in voltage was measured at around 40 V (Fig. 2.4a). CMUT B exhibited a sharp shift in resonant frequency from 0.66 MHz to 0.88 MHz as the signal voltage increased from 2 V_{pp} to 10 V_{pp}. This was accompanied by a significant decrease in Q-factor, from 11.2 to 8.9, with increasing bias voltage (Fig. 2.4b). CMUT C displayed prominent spring softening, with the resonant frequency increasing from 1.46 MHz at 10 V_{dc} to 1.39 MHz at 70 V_{dc}, alongside a slight decrease in Q-factor from 4.5 to 3.2 (Fig. 2.4c). Conversely, CMUT D showed stable resonant frequency at around 4.5 MHz across different bias voltages, accompanied by a slight decrease in Q-factor from 36.9 to 34.9 (Fig. 2.4d).

The frequency response of all CMUTs was measured at comparable bias voltages (Fig. 2.4e). The resonant frequency increased progressively from CMUT A to CMUT D. These results suggest that the spring arm design plays a more significant role in lowering the device's resonant frequency than the anchoring type.

The geometry of the connecting arms and the anchoring scheme strongly determine a CMUT's electro-mechanical behavior. Introducing compliant features—either rocker supports or spring arms—reduces the effective cavity gap, which lowers the pull-in voltage and enables low-voltage operation. Rocker supports typically achieve the larger gap reduction (0.75 µm vs 2 µm for traditional anchoring), so their impact on pull-in voltage is the greatest (Table 2.1). Similar observations were also made for the Q-factor of the CMUTs with CMUT A and C having significantly lower Q factor compared to CMUT B and D. This could be attributed to the elimination of anchor losses due to the rocker support, combined with a reduced gap that facilitates easier plate displacement. These factors significantly increase thin-film damping, which strongly influences the Q-factor (Bao & Yang (2007c)). Another factor could be the introduction of frictional losses due to dynamic rubbing of the rocker stems on the substrate. The broad The Q-factor tuning observed in CMUTs A and B originates from their spring-connecting arm, which introduce additional bend-related losses. These losses increase energy dissipation over a given bias-voltage range, resulting in greater Q-factor tunability. For comparison, CMUT A achieves a Q-factor of 1.2, significantly lower than the Q of 64 reported in (Tawfik et al. (2019b)) for similar-sized device fabricated using PolyMUMPS even achieving significantly lower pull-in voltage at 40 V compared to 163 V. Compared with piston CMUT (Merbeler, Wismath, Haubold, Bretthauer & Kupnik (2022c)) with 25 V and low-bias VOC CMUT (Park, Yoon, Lee, Kim, Seo, Chung, Unger, Kupnik & Lee (2018)) with 8 V pull-in voltage respectively; our PolyMUMPs device achieves low-voltage operation with substantially broader bandwidth by lowering effective stiffness via spring arms and rocker supports, suited for broadband pulse-echo.

2.5 Conclusion

This study has presented a novel capacitive micromachined ultrasonic transducer (CMUT) design incorporating spring arms and rocker supports, tailored for low-voltage and portable applications. Through extensive electrical characterization and simulations, this work's findings demonstrate significant enhancements in device performance in the context of ultrasonic transduction: for similar device footprint and acoustic power transmission level as a conventional CMUT, the

novel topologies proposed leverage flexible spring arms and free anchor rocker supports to yield a 6.5× bias voltage decrease, a 25× Q-factor reduction and a 10× lower resonant frequency. The improved operational parameters improve suitability for air-coupled applications.

Acknowledgment

The authors wish to acknowledge the importance of CMC Microsystems in providing access to the design and simulation tools as well as to the MEMSCAP PolyMUMPs technology. We also wish to thank Mr. Christophe Clement, Research Fellow, Polytechnique Montreal, for assistance with the MEMS release process. LaCIME testing and characterization facilities were also instrumental.

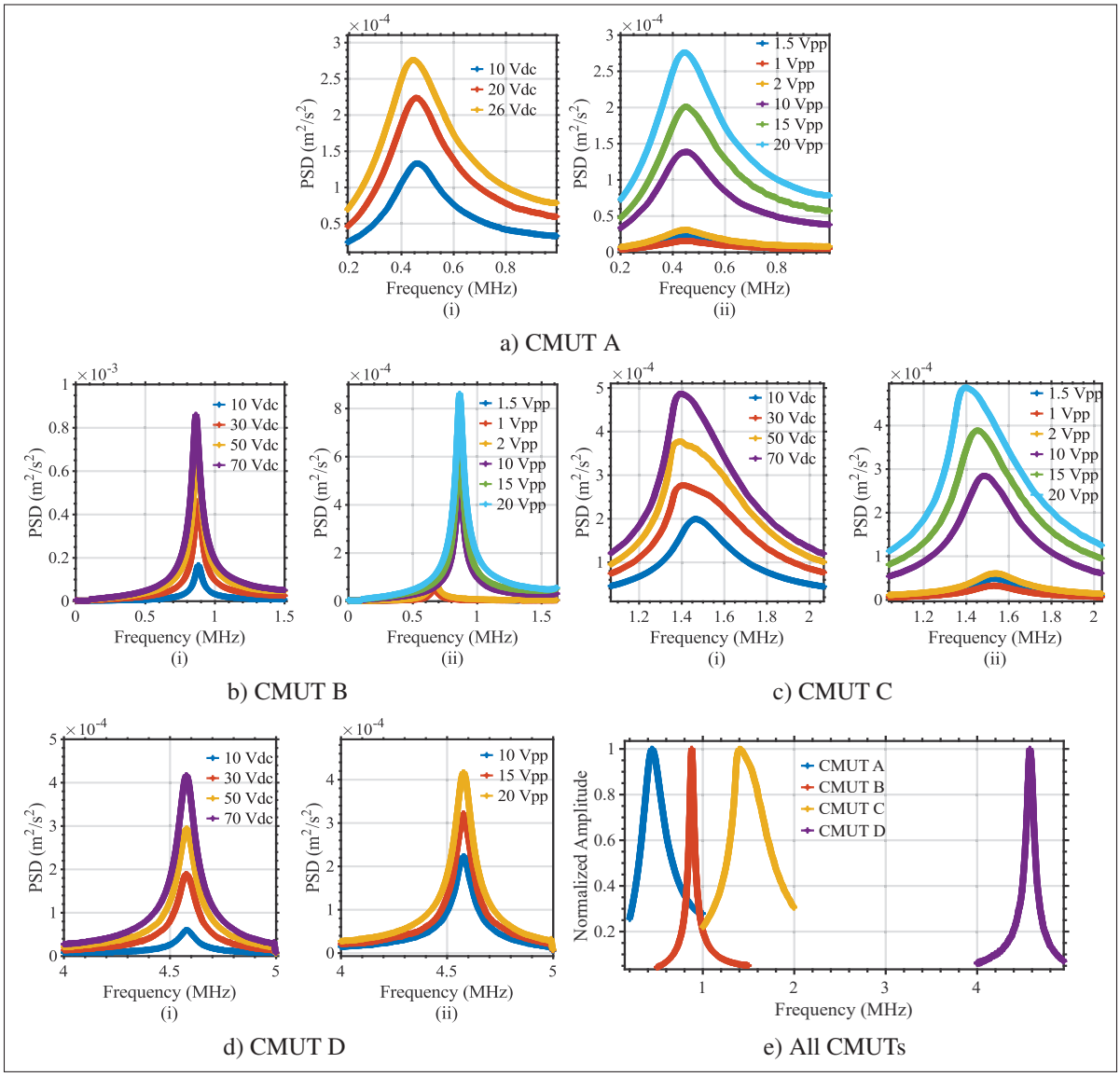

Figure 2.4 Acceleration PSDs of CMUTs vs Frequency: (a) CMUT A (i) different bias voltages (20 V_{pp}); (ii) different signal amplitudes (26 V_{dc}), (b) CMUT B (i) different bias voltages (20 V_{pp}); (ii) different signal amplitudes (70 V_{dc}), (c) CMUT C (i) different bias voltages (20 V_{pp}); (ii) different signal amplitudes (70 V_{dc}), (d) CMUT D (i) different bias voltages (20 V_{pp}); (ii) different signal amplitudes (70 V_{dc}), and (e) Acceleration PSD of CMUTs B, C, and D at 30 V_{dc} and 20 V_{pp}, and CMUT A at 26 V_{dc} and 20 V_{pp}

CHAPTER 3

DECOMPOSING INTRINSIC AND FLUIDIC LOSSES IN CMUT TOPOLOGIES: A COMPARATIVE STUDY OF ARM GEOMETRY, ANCHORING, AND ENVIRONMENT

3.1 Introduction

Ultrasound underpins a wide range of applications from medical imaging to non-destructive testing and ranging because it offers high frequencies and directivity. Imaging quality, however, is fundamentally tied to the transducer's bandwidth: broader fractional bandwidth shortens the emitted/received pulse, improving axial resolution, while resonant-frequency trade off resolution against penetration depth. Hence, ultrasound systems benefit from wideband operation to balance resolution and depth across a useful frequency span (Ma, Firouzi, Brenner & Khuri-Yakub (2019); Zhang, Liang, Wang, Ye, Rui & Zhang (2020b)).

Capacitive micromachined ultrasonic transducers (CMUTs) have emerged as a compelling platform for such wideband systems because they are batch-fabricated, in arrays, and well suited for co-integration with front-end electronics. Unlike many piezoelectric stacks, CMUTs can operate without impedance-matching layers and maintain broad bandwidth with good sensitivity, while offering a large operating frequency range and CMOS compatibility. These attributes have motivated significant structural and array-level strategies to widen bandwidth e.g., mixing cells of different sizes so that partially overlapping waveform superpose into a wider composite response; as well as layout choices (e.g., tighter pitch/higher fill factor) that support efficient radiation (Adelegan, Yamaner & Oralkan (2018a); Apte, Park, Nikoozadeh & Khuri-Yakub (2014a); Zhang et al. (2020b)). Process and plate-geometry innovations further enable low-voltage operation while preserving output, including reduced-gap stacks and piston-structured plates (Merbeler, Wismath, Haubold, Bretthauer & Kupnik (2022a); Tawfik, Alsaiary, Elsayed, Nabki & El-Gamal (2019a)), and recent system demonstrations extend to underwater arrays (Li, Zhang, Wang, Liu, Wang, Zeng, Zhao, Yilmaz, He, Jia, Zhang, Qin & Wang (2025)).

At a device level, bandwidth is linked to the mechanical quality factor Q; reducing Q increases bandwidth. Expressed in lumped form, $Q = \omega_0 M/R$, so broadening the response can be understood through how design and environment set the effective mass, stiffness, and mechanical loss. Prior literature primarily tunes Q structurally (e.g., membrane geometry) or via medium ((e.g., fluid loading), but direct comparison across devices and media remains difficult because raw trends versus V_{dc} and V_{pp} are device-specific and confounded by air-state viscous loss (Bao & Yang (2007a); Ma et al. (2019)). Moreover, device-to-device variation can perturb Q and spectral stability, underscoring the need for measurement-driven, comparable metrics (Ghavami, Sobhani & Zemp (2023); Kim, Lee, Park & Park (2023a)).

This work continues our previous research on characterizing two novel design elements for CMUTs in order to achieve (i) low actuation voltage to simplify electronics and improve safety/portability, and (ii) intentionally low Q for wideband, high-resolution pulse–echo operation (Goel, Cicek & Robichaud (2022a)).

We evaluate four topologies isolating two design elements— anchoring (rocker vs. fixed) and arm geometry (spring vs. straight arm). To enable fair, device comparison, we introduce a normalization of bias voltage and drive voltage to each device's pull-in to obtain a common operating point. By pairing matched operating points in air and vacuum, we separate squeeze-film damping from intrinsic dissipation and expose how design governs the Q-factor.

Rocker supports and spring arms reduce effective stiffness and thus pull-in voltage (supporting low-voltage operation) but concentrate strain on the arm curvature, predisposing devices to drive-induced softening and added energy loss. Conversely, fixed anchors and straight arm can distribute strain and can accumulate geometric tension under motion, favoring drive-induced stiffening and potential increase in Q. In order to do a quantitative analysis to understand how the change in bias and signal voltage effect the Q-factor and the resonant frequency, we measure the linear rate of change of the device properties against the input voltages.

Finally, the electrical properties of the novel devices in this study are compared to earlier studies on CMUTs based on multi-frequency arrays, reduced gaps, and piston-structured plates (Adelegan et al. (2018a); Apte et al. (2014a); Merbeler et al. (2022a); Tawfik et al. (2019a)).

3.2 Methods

This section details how we designed, modeled, and compared the four CMUT topologies. We first summarize the devices and the electromechanical and damping models governing their resonance in air and vacuum. We then construct a pull-in-normalized common operating point to enable fair cross-topology comparison, formulate an additive $1/Q$ decomposition at that point to separate arm- and anchor-related losses, and define the bias- and drive-sensitivities of f and Q.

3.2.1 Devices and prior work

Four CMUT topologies are studied: A (spring arm, rocker anchor), B (spring arm, fixed anchor), C (straight arm, rocker anchor), and D (straight arm, fixed anchor). Detailed geometries and fabrication are explained in prior work (Goel et al. (2022a); Goel, Gratuze, Robichaud, Izquierdo & Cicek (2025)).

3.2.2 Electromechanical model (spring softening)

Each CMUT cell is modeled as a lumped mass–spring–damper with parallel-plate electrostatic actuation. For small deflections $x \ll g$, linearization of the electrostatic force about the static operating point yields an effective negative (softening) stiffness given by eq. 3.1

$$k_{\text{elec}}(V_{\text{dc}}) = -\frac{\varepsilon_0 A}{g^3} V_{\text{dc}}^2 \tag{3.1}$$

, so that the biased resonance follows eq. 3.2

$$f(V_{\mathrm{dc}}) = \frac{1}{2\pi}\sqrt{\frac{k_{\mathrm{mech}} - k_{ele}(V_{\mathrm{dc}})}{m}}, \tag{3.2}$$

i.e., a downward tuning of f with increasing V_{dc} (electrostatic spring softening) (Khuri-Yakub & Oralkan (2011a); Senturia (2001a)).

3.2.3 Damping model: air vs. vacuum

In air, the dominant velocity-dependent loss is squeeze-film damping (SFD) between the membrane and substrate. In the thin-film regime, Reynolds-equation models give eq. 3.3

$$c_{\mathrm{sfd}} \sim \frac{\mu A}{g^3}\,\Phi(\mathrm{shape}, \omega, p_0, \mathrm{Kn}), \tag{3.3}$$

where μ is the gas viscosity, A the active area, and Φ a dimensionless factor accounting for geometry, frequency, ambient pressure and rarefaction effects (Bao & Yang (2007b)). The strong $1/g^3$ dependence explains the sensitivity of Q to gap, bias (via effective gap), and oscillation amplitude in air.

In vacuum, squeeze-film contributions vanish and Q is governed by structural channels (i): thermoelastic damping (TED), anchor/support losses, and internal material friction, combined as eq .3.4 Frangi, Cremonesi, Jaakkola & Pensala (2013); Lifshitz & Roukes (2000)

$$\frac{1}{Q_{total}} = \sum_i \frac{1}{Q_i}. \tag{3.4}$$

Where DC bias induces a small static sag and in-plane stress, a larger fraction of the stored energy can be tensile and nearly lossless; we interpret corresponding increases of Q with bias as a bias-assisted reduction of the effective structural loss (related to dissipation dilution in

strained resonators (Fedorov, Engelsen, Ghadimi, Bereyhi, Schilling, Wilson & Kippenberg (2019); Schmid, Villanueva & Roukes (2023)), without assuming ideal dilution.

3.2.4 Pull-in-normalized operating point for Q-factor comparison

Directly comparing Q_{air} and Q_{vac} for A–D at the same absolute $(V_{\mathrm{dc}}, V_{\mathrm{pp}})$ would be misleading, because resonance frequency and Q-factor, all vary with bias and drive, and each topology has a different pull-in voltage and accessible range. To enable a fair comparison, we normalize operating conditions to pull-in and interpolate each device to a common pull-in-normalized point.

We define eq. 3.5

$$\hat{V}_{\mathrm{dc}} = \frac{V_{\mathrm{dc}}}{V_{\mathrm{PI}}}, \qquad \hat{V}_{\mathrm{pp}} = \frac{(V_{\mathrm{pp}}/2)}{(V_{\mathrm{PI}} - V_{\mathrm{dc}})}, \tag{3.5}$$

where V_{PI} is the pull-in voltage of the corresponding device. Figure 3.1 shows the accessible normalized bias ranges for A–D. A common normalized bias and drive, $(\hat{V}^*_{\mathrm{dc}}, \hat{V}^*_{\mathrm{pp}}) = (0.269,\ 0.026)$, is chosen within the overlap of all four devices. For each CMUT, the corresponding physical $(V_{\mathrm{dc}}, V_{\mathrm{pp}})$ at $(\hat{V}^*_{\mathrm{dc}}, \hat{V}^*_{\mathrm{pp}})$ are obtained by linear interpolation on the measured $(V_{\mathrm{dc}}, V_{\mathrm{pp}})$ grid, and the associated Q_{air} and Q_{vac} values are extracted at that point. A detailed description of the interpolation and Q-extraction procedure is provided in Appendix I.

At any matched operating point, we separate environmental and intrinsic contributions using the additive-loss model by eq. 3.6

$$\frac{1}{Q_{\mathrm{air}}} = \frac{1}{Q_{\mathrm{vac}}} + \frac{1}{Q_{\mathrm{SFD}}}, \tag{3.6}$$

where Q_{SFD} denotes the effective squeeze-film damping. Two figures of merit are reported by eq. 3.7

$$R_Q = \frac{Q_{\mathrm{vac}}}{Q_{\mathrm{air}}}, \qquad \mathrm{SFD}\% = 100\left(1 - \frac{Q_{\mathrm{air}}}{Q_{\mathrm{vac}}}\right), \tag{3.7}$$

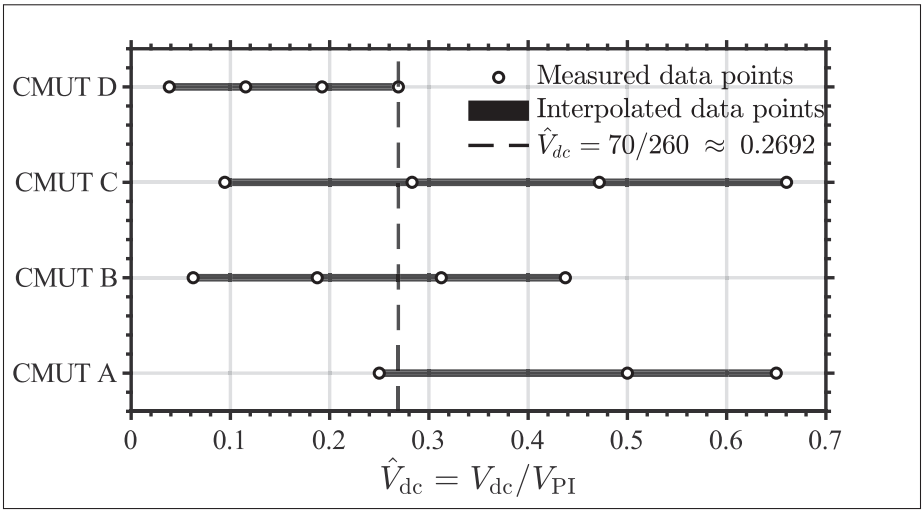

Figure 3.1 Normalized DC bias range $\hat{V}_{dc}$ for CMUTs A–D. Solid horizontal bars indicate the accessible $\hat{V}_{dc}$ interval per device, open circles mark all evaluated operating points, and the vertical dashed line denotes the selected common $\hat{V}_{dc}$ used for cross-device

which quantify, respectively, the recovery of Q in vacuum and the fraction of air-loaded loss attributable to the surrounding fluid.

3.2.5 Damping decomposition at the common operating point

At the common pull-in-normalized operating point, we assume that in vacuum the measured loss is dominated by structural mechanisms associated with the arms and the anchors given by eq. 3.8

$$\frac{1}{Q_{\mathrm{vac}}} \approx \frac{1}{Q_{\mathrm{arm}}} + \frac{1}{Q_{\mathrm{anchoring}}}, \tag{3.8}$$

for each topology. Here, Q_{arm} captures losses linked to the connecting arms (including TED and bending-related dissipation), and $Q_{\mathrm{anchoring}}$ captures losses related to the anchoring scheme (rocker vs. fixed), including anchor motion and interface/frictional effects.

Because the four designs differ only by arms and anchors, pairwise comparisons allow these contributions to be isolated:

- Comparing B (spring, fixed) and D (straight, fixed) isolates the arm contribution, since both share fixed anchors.
- Comparing A (spring, rocker) and B (spring, fixed) isolates the anchoring contribution, since both share spring arms.

The extracted effective $1/Q_{\text{arm}}$ and $1/Q_{\text{anchoring}}$ are then used to predict $Q_{\text{vac,C}}$ for topology C (straight, rocker) via equation (3.8) and to validate the consistency of the decomposition against measurement.

3.2.6 Voltage sensitivities of f and Q

To qualify how each topology responds to bias and drive beyond the single operating point, we sweep dc bias V_{dc} and ac drive amplitude V_{pp} in both air and vacuum. Out-of-plane vibration spectra are measured with a Laser Doppler Vibrometer, and the primary resonance is fitted with a Lorentzian profile to extract f and Q for each operating condition.

Although the underlying dependence may not be perfectly linear, the slope of a simple linear fit provides a convenient scalar measure of the overall trend and is used here for comparison between devices. Local sensitivities are then defined as the change in resonant frequency S^f and the Q-factor S^Q per unit change in bias and drive voltages, as specified in Tables 3.3–3.6).

3.3 Characterization and Results

3.3.1 Characterization Methodology

All measurements were performed at room temperature using a Polytec MSV-300 (Polytec PI Inc., Auburn, MA) Laser Doppler Vibrometer (LDV). Velocity spectra were acquired for the four fabricated CMUT topologies (A–D) in both air and vacuum.

In air and vacuum, the CMUTs were driven in the 200 kHz–4 MHz range with a sampling frequency of 10.6 MHz. CMUT A was biased from 10 V_{dc} to 26 V_{dc}, while CMUTs B–D were biased from 10 V_{dc} to 70 V_{dc} in 20 V_{dc} steps. For each bias condition, the devices were excited using a sinusoidal drive spanning 1 V_{pp} to 2 V_{pp} in 0.5 V_{pp} steps and 10 V_{pp} to 20 V_{pp} in 5 V_{pp} steps. For CMUTs B, C, and D, the maximum bias was limited to 70 V_{dc} to avoid pull-in.

Measured velocity spectra were converted to power spectral density (PSD) in MATLAB. The resulting acceleration PSDs in air and in vacuum for CMUTs A–D are compiled in Figs. 3.2 and 3.3, which form the basis for the extracted resonant frequency and quality factor trends are discussed in the following subsections. Table 3.1 represents a summary of the CMUT topologies along with their resonant frequency, quality factor and pull-in voltage at 20 V_{pp} and different V_{DC} in both air and vacuum environment.

Table 3.1 CMUT topologies and characterization at 20 V_{pp}

Topology	Connecting Arm	Anchoring	Gap (μm)	Vdc (V)	Resonant Frequency (MHz)	Q Factor (Air)	Q Factor (Vacuum)	Pull-in Voltage (V)
CMUT A	Spring arm	Rocker support	0.75	26	0.45	1.12–0.75 (10 Vdc–26 Vdc)	19.4	40
CMUT C	Straight arm			70	1.52	3.96–4.11 (10 Vdc–70 Vdc)	22.6	106
CMUT B	Spring arm	Fixed anchoring	2	70	0.88	11.21–8.88 (10 Vdc–70 Vdc)	543.3	160
CMUT D	Straight arm			70	3.17	35.49–34.46 (10 Vdc–70 Vdc)	174.6	260

3.3.2 Air-coupling

Figure 3.2 summarizes the air-coupled acceleration PSDs for the four devices under systematic bias and drive sweeps. CMUT A exhibits a slight downward shift of the resonance from 0.45 MHz at 10 V_{dc} to 0.442 MHz at 26 V_{dc}, with Q decreasing from 1.54 to 1.18 before pull-in at 40 V. CMUT B shows a modest upward shift from 0.66 MHz to 0.88 MHz with drive, with Q decreasing from 11.2 to 8.9. CMUT C softens from 1.46 MHz to 1.39 MHz, with Q decreasing from 4.5 to 3.2. CMUT D remains near 4.5 MHz with a small change in Q (36.9 to 34.9). At comparable operating conditions (Fig. 3.2(e)), the resonance frequencies increase monotonically from A to D.

These air-coupled measurements already highlight clear differences between topologies in terms of bandwidth and effective stiffness. A detailed interpretation in terms of electrostatic tuning, nonlinearity, and damping mechanisms is deferred to Sections 3.3.5 - 3.3.4.

3.3.3 Vacuum-coupling

Figure 3.3 shows the acceleration PSDs for CMUTs A–D measured under vacuum for dc-bias sweeps (i) and ac-drive sweeps (ii). In vacuum, the resonances are significantly sharper and taller than in air, reflecting the suppression of viscous squeeze-film damping.

CMUT A develops a broadened, left-skewed peak with increasing V_{pp}, together with a drive-dependent decrease of the resonance, indicative of a spring softening. CMUT B remains narrow and nearly invariant with both bias and drive within the explored range. CMUT C exhibits weak softening and mild broadening, while CMUT D remains effectively unchanged in resonant frequency, consistent with its stiff, straight-arm design. These spectral signatures are quantified in terms of frequency tuning and Q-factor evolution in Sections 3.3.5 and 3.3.6.

3.3.4 Quality-Factor Comparison and Damping Decomposition Across CMUT Topologies

All results are summarized in table 3.2. At the common operating point, we assume that the dominant intrinsic loss channels are approximately independent and additive in $1/Q$. In this framework, each topology has an (i) arm-related loss $1/Q_{\text{Arm}}$, and (ii) rocker-anchor loss $1/Q_{\text{Anchoring}}$.

Table 3.2 Pairwise results at a common pull–in–margin operating point, $\hat{V}_{\text{dc}} = 0.269$ and $\hat{V}_{\text{pp}} = 0.026316$. Values are obtained by linear interpolation at the operating point

Pair & device	V_{dc}	V_{pp}	Q_{vac}	Q_{air}	R_Q	SFD (%)
A (spring, rocker)	10.76	1.539	6.36	1.46	4.36	77.1
B (spring, fixed)	43.04	6.156	140.14	9.95	14.09	92.9
C (straight, rocker)	28.51	4.07	6.40	4.44	1.44	30.66
D (straight, fixed)	69.94	10.003	167.07	36.22	4.61	78.3

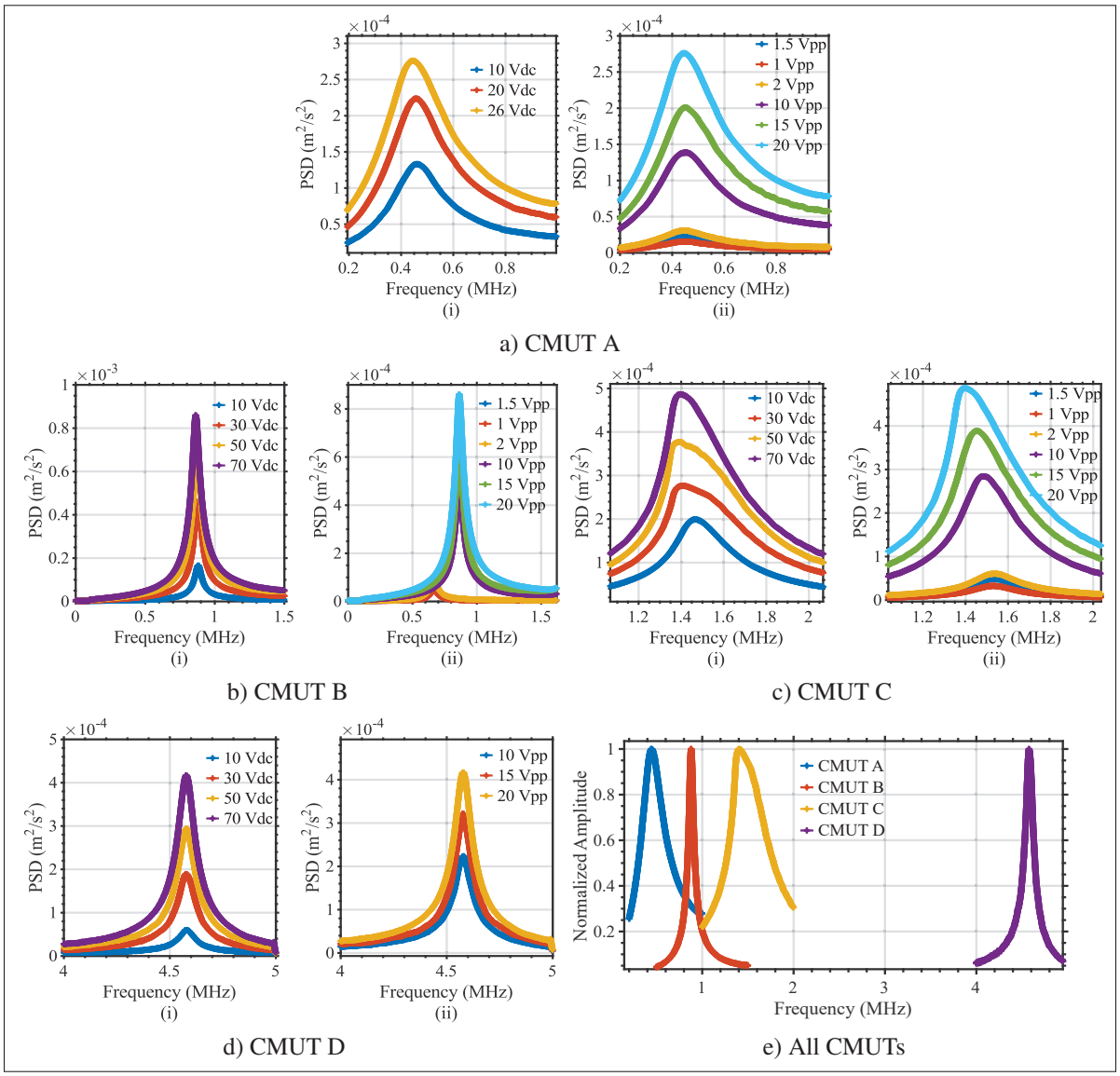

Figure 3.2 Acceleration PSDs of CMUTs vs. frequency in air: (a) CMUT A: (i) different bias voltages at 20 V_{pp}; (ii) different drive amplitudes at 26 V_{dc}; (b) CMUT B: (i) different bias voltages at 20 V_{pp}; (ii) different drive amplitudes at 70 V_{dc}; (c) CMUT C: (i) different bias voltages at 20 V_{pp}; (ii) different drive amplitudes at 70 V_{dc}; (d) CMUT D: (i) different bias voltages at 20 V_{pp}; (ii) different drive amplitudes at 70 V_{dc}; (e) comparison of CMUTs at a common operating condition (CMUT B, C, D at 30 V_{dc}, 20 V_{pp}; CMUT A at 26 V_{dc}, 20 V_{pp})

1. **Comparing A (spring arm, rocker anchor) to B (spring arm, fixed anchor).**

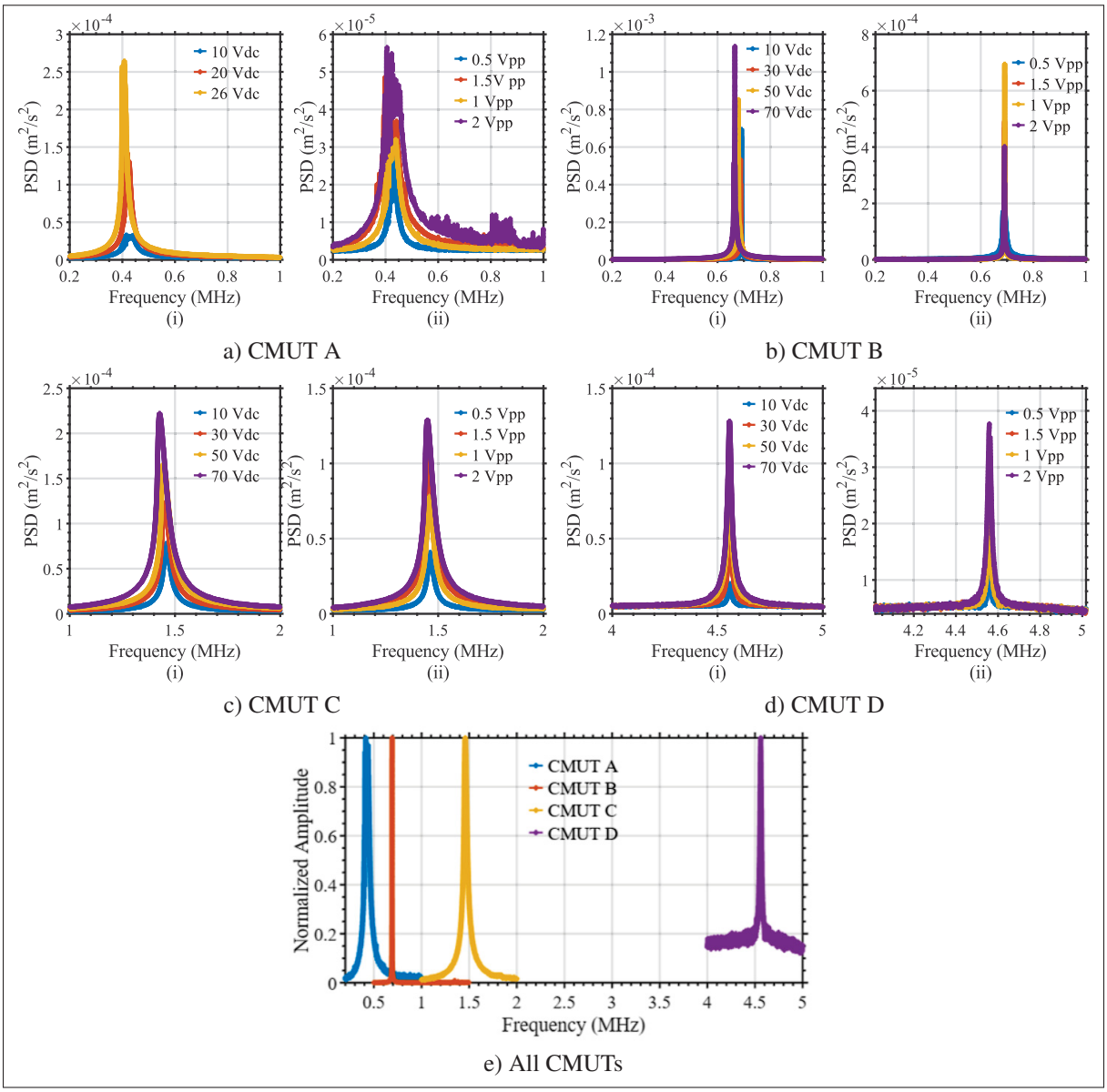

Figure 3.3 Acceleration PSDs of CMUTs vs. frequency in vacuum: (a)–(d) CMUTs A–D under (i) dc-bias sweeps at fixed 1 V_{pp} and (ii) drive sweeps at fixed 10 V_{dc}; (e) comparison of CMUTs A–D at 10 V_{dc} and 1 V_{pp}

For A and B, the arm design is identical, so the difference in $1/Q_{vac}$ is attributed to anchoring:

$$\frac{1}{Q_{\text{Anchoring}}} \approx \frac{1}{Q_{\text{vac,A}}} - \frac{1}{Q_{\text{vac,B}}} . \tag{3.9}$$

Moving from rocker to fixed anchoring (A $\rightarrow$ B) raises Q_{vac} from 6.36 to 140.14 and increases the squeeze-film damping fraction SFD from 77.1% to 92.9%. This indicates that in A, boundary rotation and acoustic/elastic radiation through the rocker stem constitute a dominant intrinsic loss pathway, while B is much less limited by intrinsic (non-gas) damping and therefore appears more gas-damping dominated.

2. **Comparing B (spring, fixed) to D (straight, fixed).**

For B and D, the anchoring is identical (fixed), so the difference isolates the arm contribution:

$$\frac{1}{Q_{\text{Arm}}} \approx \frac{1}{Q_{\text{vac,B}}} - \frac{1}{Q_{\text{vac,D}}} . \tag{3.10}$$

Under fixed anchoring, straight arms (D) exhibit lower intrinsic losses than spring arms (B): Q_{vac} increases from 140.14 to 167.07, while SFD decreases from 92.9% to 78.3%. Consistently, Q_{air} improves by a factor of ~ 3.6 (9.95 $\rightarrow$ 36.22). This behavior is compatible with reduced hinge/edge dissipation (e.g., thermoelastic and anchor-coupled losses) and weaker thin-film damping in the straighter arm design.

3. **Relating A (spring/rocker) to D (straight/fixed).**

Topology D (straight, fixed) is treated as the low-loss baseline:

$$\frac{1}{Q_0} \approx \frac{1}{Q_{\text{vac,D}}} . \tag{3.11}$$

Topology A (spring, rocker) then includes all three contributions:

$$\frac{1}{Q_{\text{vac,A}}} \approx \frac{1}{Q_0} + \frac{1}{Q_{\text{Arm}}} + \frac{1}{Q_{\text{Anchoring}}} . \tag{3.12}$$

Combining the expressions yields

$$\frac{1}{Q_{\text{Arm}}} + \frac{1}{Q_{\text{Anchoring}}} \approx \frac{1}{Q_{\text{vac,A}}} - \frac{1}{Q_{\text{vac,D}}} . \tag{3.13}$$

Table 3.3 Air: raw and normalized $\Delta f / f_0$ sensitivities. Slopes are fit in the raw voltage domain; normalized S^f use V_{PI} (A–D: 40, 160, 106, 260 V)

Device	**Bias** (fixed V_{pp} = 20 V)				**Drive** (fixed V_{dc})			
	V_{pp} (V)	a^f_{dc} (%/V^2)	S^f_{dc} (%/unit)	R^2	V_{dc} (V)	a^f_{pp} (%/V^2)	S^f_{pp} (%/unit)	R^2
CMUT A	20	-6.747×10^{-3}	-1.0795×10^{1}	0.889	26	-9.233×10^{-3}	-1.8097×10^{0}	0.955
CMUT B	20	-4.465×10^{-4}	-1.1430×10^{1}	1.000	30	3.666×10^{-4}	6.1955×10^{0}	0.874
CMUT C	20	-7.467×10^{-4}	-8.390×10^{0}	0.433	30	-2.212×10^{-2}	-1.2777×10^{2}	0.964
CMUT D	20	2.601×10^{-7}	1.758×10^{-2}	0.000	30	-4.253×10^{-4}	-2.2498×10^{1}	0.966

The large increase of Q_{vac} from 6.36 (A) to 167.07 (D), together with similar SFD values (77–78%), confirms that the combination of spring arms and rocker anchors in A introduces substantial intrinsic loss, while gas damping scales comparably once intrinsic losses are reduced.

4. **Estimating C (straight arm, rocker anchor) via piecewise loss superposition.**

Topology C (straight, rocker) combines the straight-arm behavior of D with the rocker-anchor penalty extracted from A vs. B. Under the additive-loss assumption,

$$\frac{1}{Q_{\mathrm{vac,C}}} \approx \frac{1}{Q_0} + \frac{1}{Q_{\mathrm{Anchoring}}} \,. \tag{3.14}$$

Substituting $\frac{1}{Q_0} \approx \frac{1}{Q_{\mathrm{vac,D}}}$ and $\frac{1}{Q_{\mathrm{Anchoring}}} \approx \frac{1}{Q_{\mathrm{vac,A}}} - \frac{1}{Q_{\mathrm{vac,B}}}$ gives

$$\frac{1}{Q_{\mathrm{vac,C}}} \approx \frac{1}{Q_{\mathrm{vac,D}}} + \left(\frac{1}{Q_{\mathrm{vac,A}}} - \frac{1}{Q_{\mathrm{vac,B}}}\right), \tag{3.15}$$

which, using $Q_{\mathrm{vac,A}} = 6.36$, $Q_{\mathrm{vac,B}} = 140.14$, $Q_{\mathrm{vac,D}} = 167.07$, yields $Q_{\mathrm{vac,C}} \approx 6.4$.

The predicted intrinsic Q of topology C is therefore essentially as low as that of topology A and From Fig.I-1 (i), the measured $Q_{\mathrm{air}} \approx 4.44$ of CMUT C at the same operating point further supports this conclusion.

Table 3.4 Vacuum: raw and normalized $\Delta f/f_0$ sensitivities. Slopes are fit in the raw voltage domain; normalized S^f use V_{PI} (A–D: 40, 160, 106, 260 V)

Device	**Bias** (fixed V_{pp} = 1 V)				**Drive** (fixed V_{dc} = 10 V)			
	V_{pp} (V)	a^f_{dc} (%/V^2)	S^f_{dc} (%/unit)	R^2	V_{dc} (V)	a^f_{pp} (%/V^2)	S^f_{pp} (%/unit)	R^2
CMUT A	1	-2.962×10^{-3}	-4.739×10^{0}	0.366	10	-9.566×10^{-1}	-8.609×10^{2}	0.495
CMUT B	1	-7.538×10^{-4}	-1.930×10^{1}	0.999	10	-2.510×10^{-2}	-5.647×10^{2}	0.981
CMUT C	1	-4.221×10^{-4}	-4.743×10^{0}	0.955	10	-2.280×10^{-1}	-2.101×10^{3}	0.942
CMUT D	1	-1.417×10^{-5}	-9.579×10^{-1}	0.912	10	1.947×10^{-3}	1.2169×10^{2}	0.035

Table 3.5 Air: raw and normalized $\Delta Q/Q_0$ sensitivities. Slopes are fit in the raw voltage domain; normalized S^Q use V_{PI} (A–D: 40, 160, 106, 260 V)

Device	**Bias** (fixed V_{pp} = 20 V)				**Drive** (fixed V_{dc})			
	V_{pp} (V)	a_{dc} (%/V^2)	S_{dc} (%/unit)	R^2	V_{dc} (V)	a_{pp} (%/V^2)	S_{pp} (%/unit)	R^2
CMUT A	20	-4.070×10^{-2}	-6.512×10^{1}	0.999	26	-3.396×10^{-2}	-6.656×10^{0}	0.962
CMUT B	20	-4.249×10^{-3}	-1.0877×10^{2}	0.916	30	-1.407×10^{-2}	-2.3778×10^{2}	0.988
CMUT C	20	-1.755×10^{-3}	-1.9719×10^{1}	0.095	30	-1.085×10^{-1}	-6.267×10^{2}	0.979
CMUT D	20	4.238×10^{-4}	2.8649×10^{1}	0.868	30	-8.164×10^{-3}	-4.3188×10^{2}	0.442

Table 3.6 Vacuum: raw and normalized $\Delta Q/Q_0$ sensitivities. Slopes are fit in the raw voltage domain; normalized S^Q use V_{PI} (A–D: 40, 160, 106, 260 V)

Device	**Bias** (fixed V_{pp} = 1 V)				**Drive** (fixed V_{dc} = 10 V)			
	V_{pp} (V)	a_{dc} (%/V^2)	S_{dc} (%/unit)	R^2	V_{dc} (V)	a_{pp} (%/V^2)	S_{pp} (%/unit)	R^2
CMUT A	1	3.316×10^{-1}	5.3056×10^{2}	0.993	10	-1.399×10^{1}	-1.2591×10^{4}	0.548
CMUT B	1	-5.688×10^{-4}	-1.4561×10^{1}	0.013	10	-1.044×10^{1}	-2.3490×10^{5}	1.000
CMUT C	1	-5.038×10^{-3}	-5.6607×10^{1}	0.877	10	-7.184×10^{0}	-6.6208×10^{4}	0.942
CMUT D	1	1.350×10^{-3}	9.1260×10^{1}	0.442	10	3.103×10^{0}	1.9394×10^{5}	0.914

3.3.5 Resonant frequency dependence on bias and drive

We report the relative change of resonant frequency

$$\frac{\Delta f}{f_0} \equiv \frac{f(V_{\mathrm{dc}}, V_{\mathrm{pp}}) - f_0}{f_0}, \tag{3.16}$$

where f_0 is the value at the lowest bias and drive. Figure 3.4(c) and Fig. 3.4(d) summarize the behavior for CMUTs A–D in air and in vacuum.

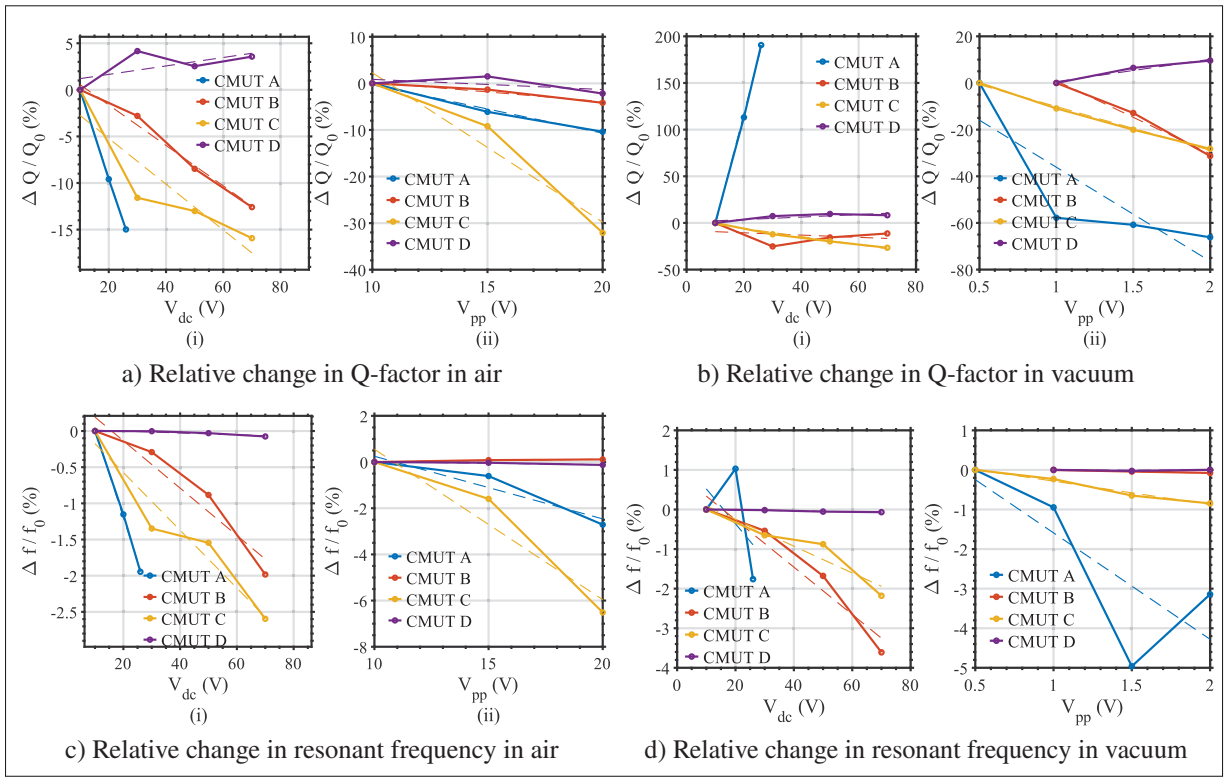

Figure 3.4 Bias- and drive-induced changes in (a,b) quality factor and (c,d) resonant frequency for CMUTs A–D in air and vacuum. Dashed lines are least-squares fits used to extract the sensitivities reported in Tables 3.3–3.4 and 3.5–3.6

Across all four CMUTs, the resonant frequency softens with dc bias as expected from electrostatic spring softening: the negative electrostatic curvature reduces the effective stiffness and lowers f_r. The magnitude of this softening follows the devices' mechanical compliance and gap, giving a consistent ranking

$$A \text{ (spring, rocker, } 0.75\mu\text{m)} > C \text{ (straight, rocker, } 0.75\mu\text{m)} >$$

$$B \text{ (spring, fixed, } 2\mu\text{m)} > D \text{ (straight, fixed, } 2\mu\text{m)}.$$

Rocker anchors add boundary compliance and therefore steepen the fractional tuning relative to fixed clamps; smaller gaps further amplify the effect through the approximate $1/g^3$ dependence.

These same design levers also govern the drive-amplitude response at fixed bias: a small softening with V_{pp} is visible in the more compliant, small-gap devices (clearly in A and weakly in C), but is negligible in B and D, whose fixed anchors, larger gaps, and higher stiffness limit motion.

Measurements in vacuum reproduce the same dc-bias softening order because the effect is purely electrostatic, while the absence of air makes the V_{pp} induced softening uniformly smaller. Thus, frequency tuning with V_{dc} dominates in both media, with air versus vacuum mainly affecting Q rather than the sign or ordering of the softening in f_r.

3.3.6 Quality factor dependence on bias and drive

We report the relative change of quality factor

$$\frac{\Delta Q}{Q_0} \equiv \frac{Q(V_{\mathrm{dc}}, V_{\mathrm{pp}}) - Q_0}{Q_0}, \tag{3.17}$$

where Q_0 is the value at the lowest bias and drive. Figure 3.4(a) and Figure 3.4(b) summarizes the behavior for CMUTs A–D in air and in vacuum.

3.3.6.1 Observations in air

In air, with increasing bias V_{dc} and V_{pp}, CMUTs A, B and C show a monotonic decrease in Q (typically 5–15 % over the explored range), whereas CMUT D exhibits a small increase. The bias induced reduction of the effective gap $g(V)$ raises squeeze film damping approximately $\propto 1/g(V)^3$, which explains the negative slopes of A, B and C as CMUT A and CMUT C have a gap of 0.75 μm which combined with compliance of rocker stem allows it move more, whereas CMUT B has spring arms which reduces its stiffness and increasing its displacement causing them to lose more energy through SFD. Another phenomenon that causes Q to drop steeper in CMUT A and CMUT C with increase in V_{pp} is the micro-slipping at the base of rocker anchoring, causing it to lose energy from the anchors to the substrate through friction and is amplitude dependent.

CMUT D which is much stiffer and has 10x less displacement at the same bias and signal voltage, causes it to have it has a weak increase in Q with bias as bias introduces in-plane tension that offsets air damping.

A DC bias (and a small rectified component of the AC drive) produces a slight static sag and in–plane tensile stress in the plate consistent with dissipation dilution. This stress stores lossless tensile energy W_{tens}, while the dissipated energy per cycle remains tied mainly to bending W_{bend}. As the ratio $W_{\text{tens}}/W_{\text{bend}}$ increases with bias/drive, the effective loss fraction is diluted and Q rises, even if the resonance softens slightly due to electrostatic spring.

3.3.6.2 Observations in vacuum

After removing the surrounding fluid, the trends separate cleanly and the intrinsic loss mechanisms are amplified. With V_{dc}, CMUT A shows a large increase in Q (order $10^2\%$), D a moderate increase, and CMUT B and CMUT C remain weakly negative. The Q increase with V_{dc} and V_{pp} for D is consistent with dissipation dilution as reported in the air.

Unlike the other CMUTs, which exhibit a single Lorentzian resonance over the entire bias range, CMUT A develops a bias-dependent doublet. This is attributed to bias-induced multimode coupling between the fundamental flexural mode and a nearby rocking/spring arm mode. Whereas with increasing V_{pp}, amplitude dependent anchor micro-slipping is reported as in the air, this is the same for CMUT C. The slope of change in Q with V_{pp} is steeper because absence of air allows a larger displacement of membrane and therefore the rocker anchoring. The absence of air also allows for the spring arms to displace more leading to more losses through TED compared to when in air for CMUT B.

3.4 Discussion

The four CMUT topologies form a structured design set in which only two elements are varied—arm geometry (spring vs. straight) and anchoring (rocker vs. fixed). This allows us to (i)

normalize performance to pull-in margin, (ii) distinguish fluidic from intrinsic damping using air/vacuum data, and (iii) apply a modular $1/Q$ model to separate the roles of arms and anchors.

3.4.1 Anchors vs. Arms: Who Sets Q?

The pairwise analysis at the common pull-in-normalized operating point (Section 3.3.4) shows a clear hierarchy.

Comparing CMUT A (spring, rocker) and CMUT B (spring, fixed) isolates anchoring: replacing the rocker with a fixed arm increases Q_{vac} from 6.36 to 140.14 and raises the squeeze-film fraction SFD from 77.1% to 92.9%. Thus the rocker support introduces a dominant intrinsic loss channel via boundary rotation, leakage into the substrate, and frictional effects.

Comparing CMUT B (spring, fixed) and CMUT D (straight, fixed) isolates arms: switching from spring to straight arms yields a smaller but measurable improvement in Q_{vac} (140.14 to 167.07) and a $\sim 3.6\times$ increase in Q_{air}. Spring arms therefore contribute additional structural loss, while straight arms define the lowest-loss baseline in this process.

Using these extracted terms to predict CMUT C (straight, rocker) gives $Q_{\text{vac,C}} \approx 6.4$, in excellent agreement with measurement. This confirms that once a rocker is introduced, anchoring loss dominates and largely suppresses the effects of straighter arms.

3.4.2 Frequency Tuning and Controlled Nonlinearity

Resonant frequency tuning across all designs is governed primarily by electrostatic spring softening, with the expected ordering $A > C > B > D$: small gaps and compliant supports yield stronger $1/g^3$-scaled softening; fixed arms and larger gaps reduce it. This ordering is identical in air and vacuum, confirming its electrostatic origin and decoupling it from fluid damping.

Nonlinearity is strongly topology dependent. CMUT A, combining spring arms, rocker anchors, and a reduced gap, exhibits softening Duffing behavior and a bias-dependent doublet in vacuum, signaling strong mode coupling and amplitude-dependent losses. CMUT C shows weaker

versions of the same trends, consistent with rocker compliance but stiffer rims. CMUTs B and D, with fixed anchors, remain nearly linear over the explored range; CMUT D in particular shows minimal drive-induced resonant shift, matching its role as the stiff, low-loss reference. Thus, the same structural elements that control Q also govern the onset of nonlinear dynamics.

3.4.3 Air vs. Vacuum: Fluidic vs. Structural Damping

Air/vacuum measurements convert these trends into a clean separation between squeeze-film and intrinsic losses.

For CMUTs B and D, large recovery factors $R_Q = Q_{\text{vac}}/Q_{\text{air}}$ and high SFD indicate that their dominant loss in air is fluidic; once in vacuum, they approach the structural baseline set by their anchors and arms. For CMUTs A and C, smaller R_Q and lower SFD confirm substantial intrinsic damping that persists without air, in agreement with the strong rocker-related term obtained from the $1/Q$ decomposition. In vacuum, the larger amplitudes at a given drive make amplitude-dependent friction and anchor motion in rocker-based designs even more apparent.

CMUT D again behaves as the reference: its modest increase in Q with bias in both media is consistent with mild dissipation dilution in a stiff, single-mode plate, and the absence of additional nonlinear or anchor-related penalties.

3.4.4 Applicability of the Common Operating Point and $1/Q$ Decomposition Framework

The analysis framework developed here consists of two conceptually separate elements:

1. a pull-in-normalized common operating point is used to compare devices at the same relative electrostatic loading,

2. a modular $1/Q$ decomposition that attributes changes in damping to specific structural elements (arms, anchors) within a co-designed family.

The first element is broadly applicable. By expressing V_{dc} and V_{pp} in normalized form (e.g. $V_{dc/pp}/V_{\mathrm{PI}}$) and evaluating Q at a common normalized operating point, one obtains a fair comparison metric for different CMUTs of similar size and actuation principle, even if their layer stacks or fabrication routes differ. Provided that: (i) devices are operated in the same medium and mode, (ii) pull-in (or an equivalent stability limit) is known or well estimated, and (iii) the chosen normalized point lies within a quasi-linear, single-mode regime, the pull-in-normalized comparison allows meaningful ranking of bandwidth, tunability, and damping across designs.

The second element, which is the additive decomposition for A–D relies on a structurally related design set, where only one feature (arms or anchors) is changed at a time. In that context, the system of pairwise comparisons is sufficiently constrained to back out effective contributions for arms and anchors and to predict the behavior of intermediate topologies (e.g. C from A/B/D).

For arbitrary CMUTs that are not constructed as such a modular family (e.g. different plate shapes, electrode layouts, stack materials, support schemes), the same algebra cannot uniquely separate $1/Q_{\mathrm{Arm}}$, and $1/Q_{\mathrm{Anchoring}}$ without additional measurements or detailed modeling.

3.4.5 Positioning Relative to Reported CMUT/PMUT Designs

Table 3.7 situates the present devices within representative CMUT and PMUT implementations and clarifies what is distinctive about the proposed topologies. Wafer-bonded CMUTs with relatively large gaps and thicker plates typically report mid-to-high Q-factors in the sub-MHz to low-MHz range, but at pull-in or operating voltages on the order of $\sim$ 100 V up to several hundred volts and with larger lateral dimensions, as seen for example in Apte, Park, Nikoozadeh & Khuri-Yakub (2014b); Kupnik, Ho, Vaithilingam & Khuri-Yakub (2011); Mukhiya, Aditi, Prabakar, Raghuramaiah, Jayapandian, Gopal, Khanna & Shekhar (2015); Wang, Yu & Ning (2016b); Zhang, Liang, Wang, Ye, Rui & Zhang (2020a). Large-aperture, low-frequency concepts aimed at tens to hundreds of kilohertz similarly rely on millimeter-scale membranes and target different regimes than the compact MHz-class cells considered here (Guldiken, Zahorian, Yamaner & Degertekin (2009); Peller, Bierl & Hagelauer (2024);

Unlugedik, Atalar & Koymen (2013); Ünlügedik, Tasdelen, Atalar & Köymen (2014)). At the other end of the spectrum, several studies achieve ultra-low-voltage operation or aggressive miniaturization using specialized surface micromachining or tailored material stacks—for example, sub-10 V pull-in with ~0.12 µm gaps or engineered coatings in Gerardo et al. (2018); Merbeler, Wismath, Haubold, Bretthauer & Kupnik (2022b), or extremely high-Q beam resonators in Zega, Langfelder, Falorni & Comi (2019) but these usually depend on custom processes rather than widely accessible foundry flows.

In contrast, the four CMUT topologies reported here are implemented in an unmodified PolyMUMPs process, similar in spirit to earlier foundry-based CMUT demonstrations (Moshrefi, Ali, Gratuze & Nabki (2025); Moshrefi, Moghaddam, Jafarsadeghi Pournaki, Ali & Nabki (2024); Tawfik et al. (2019b)), but extended to a systematically co-designed family in which arm geometry and anchoring are used as explicit knobs to set both Q and pull-in-normalized operating range. Within this commercial platform, the devices cover resonant frequencies from the few-hundred-kHz to multi-MHz range with compact apertures, and achieve structurally tunable Q-factors that are intentionally positioned below those of many wafer-bonded devices when broadband response and fast ring-down are desired. In particular, the rocker/spring configurations provide low-to-moderate Q at relatively small normalized biases, enabling short pulses, wide fractional bandwidth, and reduced ringing without relying on lossy backing layers or external damping; this is advantageous for high-resolution imaging, and miniature or battery-powered systems. At the same time, the straight, fixed arm topology recovers higher Q and more efficient operation when sensitivity or transmit efficiency is prioritized, while maintaining moderate effective pull-in voltages compatible with standard on-board drivers, low-voltage ASICs, and safety constraints that are difficult to meet with the higher-bias designs in Table 3.7.

Viewed through the common operating point and air/vacuum normalization framework developed in this work, these results show that anchors and connecting arms can be exploited as clean, process-compatible levers to navigate the trade-off between bias, size, bandwidth, and dissipation: low pull-in and modest drive voltages reduce system complexity and power, while deliberately lowered Q in selected topologies yields broadband, rapidly settling transducers without resorting

to exotic materials or custom fabrication. The proposed designs therefore demonstrate that competitive, tunable CMUT performance with application-relevant low-voltage drive and controllable Q is achievable in a compact, commercially fabricated platform.

Table 3.7 Summary of CMUT and PMUT characteristics from different studies

#	Reference	MUT Type	Resonant Freq. (MHz)	Gap (μm)	Pull-in V (V)	Membrane Radius (μm)	Fabrication	Bandwidth	Q Factor
1	Tawfik et al. (2019b)	CMUT	3.33	0.75	163	30	POLYMUMPS	–	64
		CMUT	3.85	0.75	163	30	POLYMUMPS	–	1 (1.5 μm Parylene-C)
		CMUT	4.55	0.75	163	30	POLYMUMPS	–	1 (2.5 μm Parylene-C)
2	Robichaud, Cicek, Deslandes & Nabki (2018)	PMUT	1.41	–	–	100	PIEZOMUMPS	–	10.6
		PMUT	1.40	–	–	100	PIEZOMUMPS	–	8.7 (1 μm Parylene-C)
3	Ünlügedik et al. (2014)	CMUT	0.073	6.4	172	2050	Anodic bonding	–	120
4	Zhang et al. (2020a)	CMUT	0.215	5	456	400	Wafer bonding	–	6.37
5	Kupnik et al. (2011)	CMUT	0.3–0.5	2	< 100	270–310	Wafer bonding	-6 dB FBW (1–2.5%)	56.5–141.4
6	Apte et al. (2014b)	CMUT	0.129–0.196	5.3	206	162.5	Wafer bonding	FBW (19–36%)	2.77–5.56
7	Adelegan, Yamaner & Oralkan (2018b)	CMUT	0.087	14.75	–	–	Anodic bonding	-6 dB FBW (12%)	–
8	Joseph, Singh & Vanjari (2018)	CMUT	1.8–5.2	0.8	56.5 (54 μm)	30–54	SU-8 based	FBW (4.23%)	23.41
9	Unlugedik et al. (2013)	CMUT	0.03	–	–	2890	–	–	–
10	Kim, Lee, Park & Park (2023b)	CMUT	9.7–10.4 (parallel)	0.295	50	23	Si-plate-based	–	50–220
11	Moshrefi et al. (2024)	CMUT	0.606	2	< 50	99	POLYMUMPS	–	2.23
12	Zega et al. (2019)	Beam	0.027 (hardening)	–	–	–	–	–	6951
		Beam	0.024 (softening)	–	–	–	–	–	6134
		Beam	0.028 (linear)	–	–	–	Thelma micromachining	–	6593
13	Wang, Huang, Yu, Ding, Zhang, He & Zhang (2021)	CMUT	2.45–3.66	2.6	–	50–70	–	-6 dB FBW (49.7%)	–
14	Wang et al. (2016b)	CMUT	2.06	0.6	–	60	Wafer bonding	–	187
15	Mukhiya et al. (2015)	CMUT	1.5	2.5	< 100	50	Wafer bonding	–	28
16	Merbeler et al. (2022b)	CMUT	6.43	0.12	7.4	22	Surface micromachining	–	81
		CMUT	5.11	–	13.4	22	–	–	106
		CMUT	6.34	–	25	22	–	–	254
17	Peller et al. (2024)	CMUT	0.276	1.5	55.1	475	Surface micromachining	–	72.9
18	Guldiken et al. (2009)	CMUT	0.084	1.65	10.2	430	DBP MEMS	FBW (29%)	–
19	Gerardo et al. (2018)	CMUT	2.83	0.30	65	50	SU-8 based	–	40
20	Moshrefi et al. (2025)	CMUT	0.65–2.91	2	100	42.5–100	POLYMUMPS	-6 dB FBW (75–92%)	2–40

3.5 Conclusion

This work experimentally maps how two simple structural degrees of freedom, the arm geometry and the anchoring govern resonance, damping, and nonlinearity in CMUTs fabricated in a standard PolyMUMPs process. By designing four related topologies (spring/rocker, spring/fixed, straight/rocker, straight/fixed) and characterizing them systematically in air and vacuum under controlled bias and drive sweeps, The results show that anchors and arms are primary levers that set the achievable trade-off between pull-in voltage, bandwidth, and quality factor.

A pull-in-normalized common operating point, combined with air/vacuum measurements, provides a consistent basis for fair comparison across these devices and with prior literature. Within this framework, a simple additive $1/Q$ model applied to the co-designed family reveals that rocker supports introduce the dominant intrinsic loss channel, spring arms contribute a secondary but measurable penalty, and straight fixed arms define the effective low-loss baseline. The successful prediction of the straight/rocker topology from the other three confirms the internal consistency of this decomposition and demonstrates that intrinsic damping can be engineered, not merely observed.

The same structural choices that set Q also control frequency tuning and nonlinearity. Rocker/spring configurations yield strong electrostatic tuning, low or moderate Q, and pronounced nonlinear features, offering inherently broadband, fast-settling behavior at relatively low normalized bias without resorting to lossy backing layers or exotic stacks. In contrast, the straight, fixed arm topology remains stiff, nearly linear, and high-Q, and thus serves as a practical reference when transmit efficiency or sensitivity is paramount. Together, these results show that low pull-in voltage and application-tailored Q are achievable in a compact, commercially fabricated platform, rather than being exclusive to custom or high-bias voltage designs.

CHAPTER 4

HYBRID SURFACE MICROMACHINED AND SCREEN PRINTED CMUT FABRICATION PROCESS

4.1 Introduction

Capacitive micromachined ultrasonic transducers (CMUTs) are an attractive platform for medical imaging, non-invasive hemodynamic monitoring, and integrated ultrasonic sensing, offering wide bandwidth, scalability, and compatibility with standard microfabrication (Biriukov & Zelenina (2024); Jiménez et al. (2024); Khuri-Yakub & Oralkan (2011b); Oralkan, Ergun, Cheng, Johnson, Karaman, Lee & Khuri-Yakub (2002a); Rey (2024)). However, most reported CMUT technologies rely on CMOS-grade surface micromachining or wafer bonding, implemented on silicon with multiple vacuum, lithography, and etch steps. These flows are precise but expensive: each functional layer typically requires deposition, resist coating, exposure, development, etching, resist stripping, and intermediate cleans, incurring significant tool time, mask cost, and process complexity (Biriukov & Zelenina (2024); Khuri-Yakub & Oralkan (2011b)). Such infrastructure is often inaccessible in early-stage labs or for rapid design iterations, and is poorly matched to emerging applications on flexible or large-area substrates (Joshi, Moghimi et al. (2024))

In contrast, additive manufacturing techniques such as screen printing can define conductive and dielectric layers in as few as two steps (printing and curing), without full lithographic pattern transfer. For simple interconnect and electrode levels, this reduces the process complexity by an order of magnitude compared to a conventional surface-micromachined stack, with corresponding savings in time, consumables, and capital requirements (Khan, Thielens, Muja & Arias (2016)). Printed electronics technologies are already being adopted for wearable, conformal, and large-area sensors; extending these methods to CMUTs opens a path toward monolithic integration of ultrasonic transducers with printed routing, passives, and front-end circuitry on the same substrate, at substantially lower cost per design cycle (Joshi et al. (2024); Rogers, Someya & Huang (2010)).

This motivates the development of a hybrid CMUT fabrication strategy that combines the geometric control of surface micromachining (for cavity and membrane definition) with the simplicity and scalability of screen-printed electrodes and dielectrics. The goals of this chapter is therefore to: (i) realize functional CMUT structures using a reduced, low-cost toolset and relaxed thermal budgets; (ii) minimize the number of subtractive microfabrication steps by exploiting additive printing wherever possible; (iii) ensure compatibility between printed inks, sacrificial layers, and structural films so that multiple CMUT topologies can be implemented within a single flow; and (iv) establish a process platform that is fast enough for iterative topology optimization.

The remainder of this chapter formalizes this hybrid approach. Section 4.2 provides background on MEMS ultrasonic device fabrication. Section 4.3 introduces the device concept and the material and integration constraints that govern the process design. Subsequent sections describe the screen-printing and surface-micromachining modules, assemble them into a complete step-by-step flow, and assess the resulting structural quality and suitability for CMUT arrays implemented on both rigid and potentially flexible substrates.

4.2 MEMS Fabrication Strategies for Ultrasonic Devices

4.2.1 Conventional Silicon MEMS Platforms

Early MEMS ultrasonic devices were fabricated on rigid silicon substrates using high-temperature processes. Monocrystalline silicon remains widely used due to its high mechanical quality factor, stability, and compatibility with DRIE and wafer bonding Senturia (2001b).

Standardized platforms such as PolyMUMPs provide predefined film stacks (silicon nitride, multiple polysilicon layers, sacrificial oxides) and design rules that enable suspended beams, membranes, and electrodes with good reproducibility Cowen, Benidt, Hardy & Smith (1992). These technologies established much of the foundation for CMUTs, but they are less suitable

for wearable devices because of rigid wafers, high thermal budgets, multi-mask flows, and packaging complexity.

4.2.2 Polymer and Flexible MEMS

To address these limitations, polymer MEMS have been developed in which materials such as polyimide, SU-8, parylene-C, and PDMS act as substrates, structural layers, and encapsulants Kaltenbrunner, Sekitani et al. (2013); Lorenz, Despont, Fahrni, Brugger, Renaud & de Rooij (1997); Rogers et al. (2010). Polymers enable low-temperature processing, mechanical flexibility, and potential biocompatibility, making them attractive for conformal and wearable ultrasound devices. SU-8, in particular, is widely used as a structural membrane material in CMUT-like devices because it can form thick, patterned films with good mechanical stiffness Lorenz et al. (1997).

However, polymer MEMS also introduce challenges in solvent compatibility, moisture uptake, adhesion, and long-term stability of sealed cavities—issues that are critical for reliable CMUT operation and stable gaps.

4.2.3 Hybrid and Additive Approaches

Printing technologies (screen printing, inkjet, aerosol jet) have been combined with MEMS to deposit conductive and dielectric inks directly onto rigid or flexible substrates Myny (2012). Printed films can reach micron-scale thickness in one or few passes, which is attractive for electrodes, redistribution lines, and simple sensors. Screen-printed silver on polymer foils is already used in low-cost flexible electronics.

Printed layers, however, typically have higher resistivity, higher roughness, and more variable adhesion than sputtered or evaporated films. When integrated with sacrificial-layer processes, these issues can compromise gap uniformity and release yield. Hybrid flows therefore combine vacuum deposition (for critical, planar layers such as bottom electrodes) with printed conductors where large-area or low-cost patterning is desired (e.g. top electrodes and routing).

A comparison of fabrication strategies relevant to ultrasonic devices, retained from the original text, is given in Table 4.1.

Table 4.1 Comparison of MEMS fabrication strategies relevant to ultrasonic devices

Approach	**Materials / Processes**	**Advantages**	**Limitations**
Conventional MEMS (e.g., PolyMUMPs, SOI) (Cowen et al. (1992))	Silicon, polysilicon, SiO_2, SiN_x, DRIE, bonding	High precision, CMOS compatibility, mature	Rigid, high-temperature, multi-mask, costly
Polymer MEMS (Rogers et al. (2010))	Polyimide, SU-8, parylene, PDMS	Flexible, low-temperature, conformal, biocompatible	Solvent/moisture sensitivity, stability, lower stiffness
Hybrid Printing + MEMS (Myny (2012))	Printed Ag/Cu, dielectrics + micromachining	Low-cost, maskless, scalable, flexible-substrate compatible	Roughness, adhesion, reliability of printed films

These trends directly motivate the hybrid CMUT development. Next chapter introduces the design concept and constraints in the development of this new fabrication process.

4.3 Device Concept and Process Integration Constraints

The hybrid process developed in this work must (i) realize mechanically robust capacitive CMUT cells with well-defined gaps and membranes, and (ii) remain compatible with printable inks, reduced thermal budgets, and a limited set of cleanroom tools. This section outlines the target CMUT architecture and the integration constraints that shape the material stack and process sequence.

The CMUTs are based on a conventional parallel-plate cavity structure: a compliant top membrane carrying the upper electrode is suspended above a bottom electrode by a sealed vacuum (or low-pressure) gap. An applied DC bias V_{DC} establishes the electrostatic operating point, while a small ac excitation V_{ac} drives out-of-plane vibration at the fundamental resonance.

We focus on plate-type cells and arrays suitable for low-to-mid MHz operation on rigid or potentially flexible polymeric substrates. The fabrication flow must therefore:

- define cavity depths and membrane thicknesses in the micron range with uniformity;
- ensure robust overlap and insulation between bottom electrode, cavity region, and top electrode within realistic alignment tolerances; and
- support integration with printed routing and contact pads on the same substrate.

4.4 Hybrid Process Development and Concept

4.4.1 Seed Materials and Target

The hybrid process was built around three practical choices that are compatible with standard laboratory fabrication capabilities : (i) a screen-printable silver ink, chosen for its printability and low sheet resistance; (ii) AZ 5214E, used as the sacrificial photoresist because it was readily available and well-characterized; and (iii) a glass substrate, providing dimensional stability and surface smoothness.

Additional layers and materials were introduced after a series of trial-and-error experiments in formulating the recipe. The target was to realize CMUT structures by combining printed conductors with surface micromachining: a bottom electrode on the substrate, a resist-defined sacrificial gap, a structural membrane, and a printed top electrode, under a modest thermal and chemical budget and with a flow that can ultimately be transferred to flexible substrates (e.g., Kapton).

4.4.2 Iterative Development: From Printed Stack to Hybrid Flow

4.4.2.1 Trial 1: Printed bottom / PR / printed top

The first experiments used a fully printed metal stack: a printed bottom silver electrode on glass, an AZ 5214E positive photoresist based sacrificial layer, and a printed top silver electrode. This was a simple “test capacitor” to check printability, gap formation, and basic chemistry.

Two coupled issues appeared: (1) the silver ink required a cure around ~ 175°C to become chemically and mechanically robust, but at that temperature AZ 5214E became extremely difficult or impossible to remove; and (2) if the cure temperature was limited to keep AZ 5214E removable, the top printed electrode was under-cured and degraded during sacrificial removal. In addition, the ink solvent attacked the photoresist when printed directly on it.

4.4.2.2 Trial 2: (Lift-off resist) LOR buffer under AZ 5214E

To solve the issues observed in Trial 1, the second process introduced an LOR underlayer beneath AZ 5214E so that LOR would provide extra sacrificial thickness and a more soluble underlayer.

This improved the available sacrificial thickness but did not resolve the core issues: photoresist removal still left residue, and the rough interface between the printed top electrode and the resist stack led to non-uniform gaps and frequent shorting between the top and bottom electrodes. The underlying thermal conflict between the top-ink cure and PR removability also remained.

4.4.2.3 Trial 3: Sputtered Al bottom / LOR+AZ / printed top

The third trial replaced the printed bottom electrode with a sputtered aluminum (Al) bottom electrode. The aim was to eliminate the large step height and surface texture of the printed bottom conductor and thereby obtain a smoother, more uniform gap plane. LOR and AZ 5214E were again used to form the sacrificial stack, and the top electrode was printed silver.

This change significantly improved gap uniformity but revealed two remaining limitations: (1) the top printed electrode still had to be cured at a temperature that was not compatible with keeping AZ 5214E/LOR fully removable—hard bakes made the PR effectively non-strippable, whereas softer bakes left the ink under-cured and vulnerable during stripping; and (2) the printed top electrode above a sacrificial cavity was mechanically fragile and tended to deform or collapse during wet processing.

4.4.2.4 Trial 4 (final): Sputtered Al bottom / LOR sacrificial / SU-8 membrane / printed top

The final configuration introduced a structural SU-8 membrane between the sacrificial layer and the printed top electrode:

a) A sputtered Aluminum (Al) bottom electrode was patterned on glass to define a smooth, uniform gap plane.

b) LOR and AZ 5214E were deposited and patterned so that LOR formed the main sacrificial layer; AZ 5214E was used to pattern and then removed, leaving LOR in the cavity region.

c) SU-8 was coated over the structure and patterned to form the membrane, with etch holes exposing LOR in selected regions.

d) The top silver (Ag) electrode was screen-printed on the SU-8 membrane and cured at the high temperature required by the ink; SU-8 and LOR tolerated this thermal step.

e) Finally, LOR was released through the SU-8 etch holes using a developer. The soak time was kept short so that LOR was removed while any attack on the sputtered Al bottom electrode remained limited.

This sequence provided a mechanically supported printed top electrode that could be fully cured, a smooth bottom plane for the gap, and a sacrificial layer that could be removed cleanly under the SU-8 membrane.

4.4.2.5 Release-chemistry development

In parallel with the layer stack and sequencing, the removal of the sacrificial layer was refined through several iterations. The initial plan was to use a commercial NMP-based photoresist stripper (AZ 400T) to dissolve the sacrificial resist. Although the stripper effectively removed the resist, the long soaks required for complete undercut visibly attacked the printed top electrode; under these conditions the silver ink degraded and lost continuity.

To avoid damaging the printed layer, the next trials used MF 319 as an LOR-compatible developer for release. MF 319 removed LOR reliably, but extended exposure led to noticeable attack of the sputtered Al bottom electrode. This imposed a tight timing window and made the process sensitive to small variations in soak time and agitation.

The final solution to release the CMUTs adopted in this work is by etching the sacrificial layer using AZ developer 1:1 (AZ developer diluted 1:1 with deionized water). In this formulation, the developer removes the LOR at a practical rate while leaving both the fully cured printed silver and the sputtered Al essentially unaffected over the soak times used. This provided a more robust release step with a wider process window than the stripper or MF 319 options.

4.4.3 Temperature compatibility

Table 4.2 describes the temperature compatibility between different materials. It is clear that the glass substrate and sputtered Al bottom electrode do not impose any practical thermal limitations for the process temperatures used here; both simply follow the bakes and cures required by the polymer and ink layers. The main constraints come from the sacrificial LOR and the photoresist AZ 5214E. LOR is baked at 180 °C but must remain soluble in the diluted AZ developer used for release, so its maximum temperature is kept below 190 °C. AZ 5214E is only taken to 110 °C and is always stripped before any higher-temperature steps, which prevents it from becoming difficult to remove.

In contrast, SU-8 and the printed silver ink define the upper end of the usable temperature window. SU-8 is ramp-baked to 95 °C and hard-baked at 150 °C, and is chosen specifically because it tolerates the subsequent high-temperature cure of the printed silver. The silver ink itself requires curing around 175 °C–180 °C to achieve good adhesion and conductivity; under-cured films were observed to fail during the wet release step. These combined limits justify the chosen sequencing: all AZ 5214E is removed before the top-electrode cure, LOR is protected under SU-8 during that cure, and no later process step exceeds the cure temperature of the printed silver.

Table 4.2 Temperature windows for materials in the hybrid flow

#	Material	Soft / pre-bake	Post exposure bake / hard-bake	Max Temperature seen	Temperature limit	Constraint / comment
1	Glass substrate	-	-	LOR & Printed Ag curing steps	200°C	-
2	Sputtered Al	-	-	LOR & Printed Ag curing steps	-	-
3	LOR	180°C	-	Printed Ag curing step	190°C	Must remain releasable in diluted AZ developer.
4	AZ 5214E	110°C	-	110°C	120°C before hard-backed	Always stripped before high-T steps.
5	SU-8	Ramp from 65°C to 95°C	150°C	Printed Ag curing step	250°C	Chosen to tolerate high-T cure.
6	Printed Ag	120°C	180°C	180°C	275°C	Under-cured films fail during release. Minimum cure temperature is 175°C for good adhesion and conductivity.

4.4.4 Chemical compatibility

Table 4.3 summarizes the chemical compatibility of the different materials used in the hybrid flow, restricted to combinations actually used.

The glass substrate is essentially inert to all solvents used, and the sputtered Al bottom electrode is stable in standard organic cleans and in the diluted AZ developer used for release. In early trials, however, long MF 319 soaks were found to attack exposed Al, so MF 319 was removed from the final release step.

LOR 7B is, by design, the chemically weakest layer in the stack: it is soluble in alkaline developers and NMP-based strippers, which makes it suitable as the sacrificial material. In the finalized flow, this solubility is exploited using a diluted AZ developer 1:1 for release, while more aggressive stripper-based releases were abandoned because they degraded the printed silver. AZ 5214E is used only as a temporary patterning resist on top of LOR and is stripped before it encounters any ink solvent or high-pH chemistry; direct contact with ink solvent and strong developers in early experiments led to residue and instability.

SU-8, in contrast, is chemically robust after cross-linking and tolerates all subsequent developers and solvents used in this work, including the diluted AZ developer during LOR release, with only minimal swelling under extreme conditions. Finally, the printed silver ink is stable under short,

process-level exposures to acetone, IPA, and the diluted AZ developer once it is fully cured, but it is progressively damaged by long immersion in NMP-based strippers, strong solvents, or repeated alkaline exposure. These observations motivated the choice of a mild, diluted developer for release and limited wet-process times in the final hybrid CMUT recipe.

Table 4.3 Chemical compatibility summary (qualitative, based on this work)

#	Material	Solvent base	Chemical compatibility (after curing)	Sensitive to
1	Glass substrate	–	Standard cleaning (acetone, IPA), diluted AZ developer 1:1, NMP-based stripper	–
2	Sputtered Al	–	Standard cleaning (acetone, IPA), diluted AZ developer 1:1	Long soaks in MF 319 or other strong alkaline developers (attack observed in early trials)
3	LOR 7B	Cyclopentanone	Acetone, IPA, PGMEA, cyclopentanone	Diluted AZ developer 1:1, other alkaline developers, NMP-based strippers (used intentionally for release in trials)
4	AZ 5214E	PGMEA	IPA	Acetone, strong developers, NMP-based stripper, butyl carbitol, cyclopentanone and other ink-related solvents
5	SU-8	Cyclopentanone	Standard cleaning (acetone, IPA), diluted AZ developer 1:1, NMP-based stripper, cyclopentanone, PGMEA, butyl carbitol	Very long immersion in NMP-based strippers leads to slight swelling
6	Printed Ag	Butyl carbitol	Short process exposures to acetone, IPA, diluted AZ developer 1:1 do not cause visible chemical attack or corrosion of the fully cured printed silver film.	NMP-based strippers and butyl carbitol (prolonged), as well as repeated or extended immersion in strong solvents and alkaline developers, which progressively degrade the printed silver layer and weaken its adhesion

4.5 Final Hybrid Fabrication Process

4.5.1 Materials and Equipment

Table 4.4 lists the main materials used in the finalized hybrid CMUT process, together with their roles in the stack. The detailed temperature and chemical compatibility for these layers were discussed in Sec. 4.4 and summarized in Tables 4.2–4.3.

The main fabrication tools are listed in Table 4.5. Only standard university-cleanroom equipment is required; no wafer bonding or deep reactive-ion etching (DRIE) tools are used.

Table 4.4 Materials used in the hybrid CMUT process

#	Material	Supplier / type	Function in process
1	Glass wafer	*United Scientific, 5 inch borosilicate*	Rigid substrate for CMUT array
2	Al film	*Al target*	Bottom electrode and routing layer.
3	LOR 7B	*MicroChem*	Sacrificial layer defining the gap height.
4	AZ 5214E	*MicroChemicals*	Photoresist used to pattern the LOR and the bottom Al.
5	SU-8 2002	*Kayaku*	Structural membrane with etched vent / release holes.
6	Silver screen-printing ink	*NovaCentrix, HPS-FG32*	Printed top electrode and external contact pads.
7	AZ developer 1:1	*MicroChemicals*	Release chemistry for LOR through SU-8 etch holes.
8	MF 319	*Kayaku*	Developer for AZ 5214E and LOR
9	AZ-400T stripper	*MicroChemicals*	Stripper used to remove AZ 5214E after patterning Al.

Table 4.5 Equipment used for the hybrid CMUT process

#	Tool	Use in process
1	*Plasmionique SPT-330H*	Deposition of the Al bottom electrode.
2	*Laurell WS-400BZ-6NPP/LITE*	Spin coating of AZ 5214E, LOR 7B and SU-8 2002.
3	*OAI 800MBA*	UV exposure for AZ 5214E and SU-8 lithography.
4	Hotplates / oven	Soft-bake, PEB and hard-bake of LOR, AZ 5214E and SU-8.
5	*Keko P200S*	Screen printing of the silver top electrodes and contact pads.
6	*Branson 5510*	Substrate cleaning in acetone and IPA prior to processing.
7	*KLA P-17*	Thickness measurements of printed silver lines and film steps.
8	*Polytec MSV-300*	Measurement of CMUT resonance frequency and collapse voltage.
9	*Autosamdri-815B*	Stiction-free drying after sacrificial release.

4.5.2 Baseline process flow

All steps below are carried out on 4-inch alkali-free glass wafers unless otherwise noted. Process temperatures are chosen to remain within the compatibility window. Fig. 4.1 represents the schematic cross-section and the top view of the designed cell, each process step (A-F) from the figure is associated with the steps below

1. **Substrate preparation and bottom Al electrode (AZ 5214E + Al etch) - Fig. 4.1 (A)**

   The process begins with substrate cleaning and Al patterning for the bottom electrode. Glass substrates are first solvent-cleaned in sequential ultrasonic baths of acetone (5 min) and isopropanol (5 min), followed by a DI-water rinse and N_2 blow-drying. A dehydration bake is then performed on a hotplate at approximately 150 °C for 5–10 min. After dehydration, a blanket Al layer is deposited by sputtering: the wafer is loaded into the sputter system and Al is deposited to a target thickness of 350 nm.

The bottom electrodes are defined photolithographically using AZ 5214E. The resist is spin-coated to a thickness of 2 μm at 2000 rpm for 45 s and soft-baked on a hotplate at 110 °C for 60 s. The wafer is then aligned and exposed with the bottom-electrode mask using an exposure dose consistent with the AZ 5214E datasheet and the lithography tool. After exposure, the resist is developed in MF-319 for approximately 40 s, rinsed in DI water, and dried with N_2.

The exposed Al is removed in a wet etch step using Al etchant Type A maintained at $\sim$ 40 °C. The wafer is left in the etchant until the Al is completely cleared down to the glass substrate in the exposed regions (typically about 4 min), followed by a thorough DI-water rinse and N_2 drying. Finally, the remaining AZ 5214E is stripped in AZ-400T stripper, and the wafer is rinsed in IPA and DI water and dried with N_2, leaving patterned Al bottom electrodes on the glass.

2. **Sacrificial layer definition (LOR / AZ 5214E) - Fig. 4.1 (B), (C), (D)**

   The CMUT cavities are then defined using an LOR/AZ 5214E sacrificial stack. The wafer undergoes a dehydration bake at approximately 150 °C for 5–10 min, after which LOR 7B is spin-coated at 1000 rpm for 45 s to obtain a target sacrificial thickness of 1.2 μm. The LOR is soft-baked on a hotplate following the manufacturer's guidelines, for example 180 °C for 10 min, to drive off residual solvent and stabilize the film. This is represented by fig. 4.1 (B).

   A top imaging layer of AZ 5214E, with a thickness of 2 μm, is then coated by spinning at 2000 rpm for 45 s, followed by a soft-bake at 110 °C for 60 s. This is represented by fig. 4.1 (C). The cavity pattern is transferred by aligning the wafer with the cavity mask and exposing at the appropriate dose. The exposed resist is developed in MF-319 for approximately 40 s, opened regions are rinsed in DI water, and the wafer is dried with N_2. In this step the developer also transfers the pattern into the underlying LOR, thereby defining the sacrificial features. The AZ 5214E imaging layer is then completely stripped in acetone, followed by rinsing and drying, leaving patterned LOR features on the Al bottom electrodes that define the future CMUT cavities. This is represented by fig. 4.1 (D).

3. **SU-8 membrane and etch holes - Fig. 4.1 (E).**

The structural membrane and etch holes are formed in a thin SU-8 layer. Prior to SU-8 coating, the wafer is dehydrated at ~ 150 °C for 5–10 min to promote adhesion and reduce residual moisture. If required, an SU-8-compatible adhesion promoter can be applied to the glass surface outside the LOR features. SU-8 2002 is then spin-coated at approximately 1000 rpm to achieve a target membrane thickness of 2.2 μm. The coated wafer undergoes a soft-bake on a hotplate using a stepwise temperature profile at 65 °C and 95 °C for 1 min each, followed by a return to room temperature.

The membrane and etch-hole pattern is defined by aligning and exposing the wafer with the SU-8 membrane mask, which simultaneously specifies the plate area and the distributed etch holes above the sacrificial regions. After exposure, a post-exposure bake (PEB) is performed at the same temperature levels as the soft-bake, 65/95 °C for 1 min each, followed by cooling to room temperature. The exposed SU-8 is then developed in SU-8 developer for approximately 1 min, rinsed in IPA, and dried with N_2. A final hard-bake at 150 °C for about 10 min fully cross-links the SU-8 and stabilizes the membrane. At this stage, a continuous SU-8 membrane spans the LOR sacrificial cavities, with etched openings that will later serve as release holes.

4. **Top electrode screen printing and cure This is represented by fig. 4.1 (F).**

The top electrodes are formed by screen-printing an Ag ink onto the SU-8 membrane. Before printing, the SU-8 surface is lightly cleaned with an IPA rinse and N_2 dry to remove any particulates or residues. The wafer is then mounted on the vacuum chuck of the screen printer and aligned to on-wafer fiducials. A stainless-steel screen with an emulsion thickness of 1 mil and a 325-mesh count is used, chosen to achieve the desired printed Ag thickness and feature resolution.

The Ag ink is printed through the screen onto the SU-8 membrane, with squeegee speed, pressure, and snap-off distance adjusted to obtain uniform, well-defined electrode lines; these parameters are tuned for the specific ink and screen combination. After printing, the wafer is pre-dried at a relatively low temperature (60–80 °C for approximately 30 min) to remove volatile solvents, minimizing bubble formation and ink redistribution. The printed Ag is

then cured at $\sim 180\,^{\circ}\mathrm{C}$ for about 30 min to sinter the ink and achieve stable conductivity. The wafer is allowed to cool slowly back to room temperature to limit thermal stress on the SU-8 membrane. Printed electrodes are inspected for alignment, edge definition, and electrical continuity.

5. **Sacrificial release and gap formation - Fig. 4.1 (G).**

   Finally, the sacrificial LOR layer is removed to form the CMUT cavities and release the membranes. The wafer is immersed in a diluted AZ developer solution (e.g., 1:1 dilution) under mild agitation. The release time is established from dedicated test structures to ensure that the LOR is fully removed across the wafer while leaving the Al and cured Ag layers unaffected. Once release is complete, the wafer is transferred through several DI-water baths to remove developer residues, followed by an IPA displacement rinse to reduce surface tension prior to drying.

   To avoid membrane collapse and stiction during drying, the wafer is dried using critical-point drying. After drying, the devices are inspected by optical microscopy. The inspection confirms that the etch holes are open, the cavities beneath the SU-8 are successfully formed, and the membranes remain intact and suspended above the bottom electrodes.

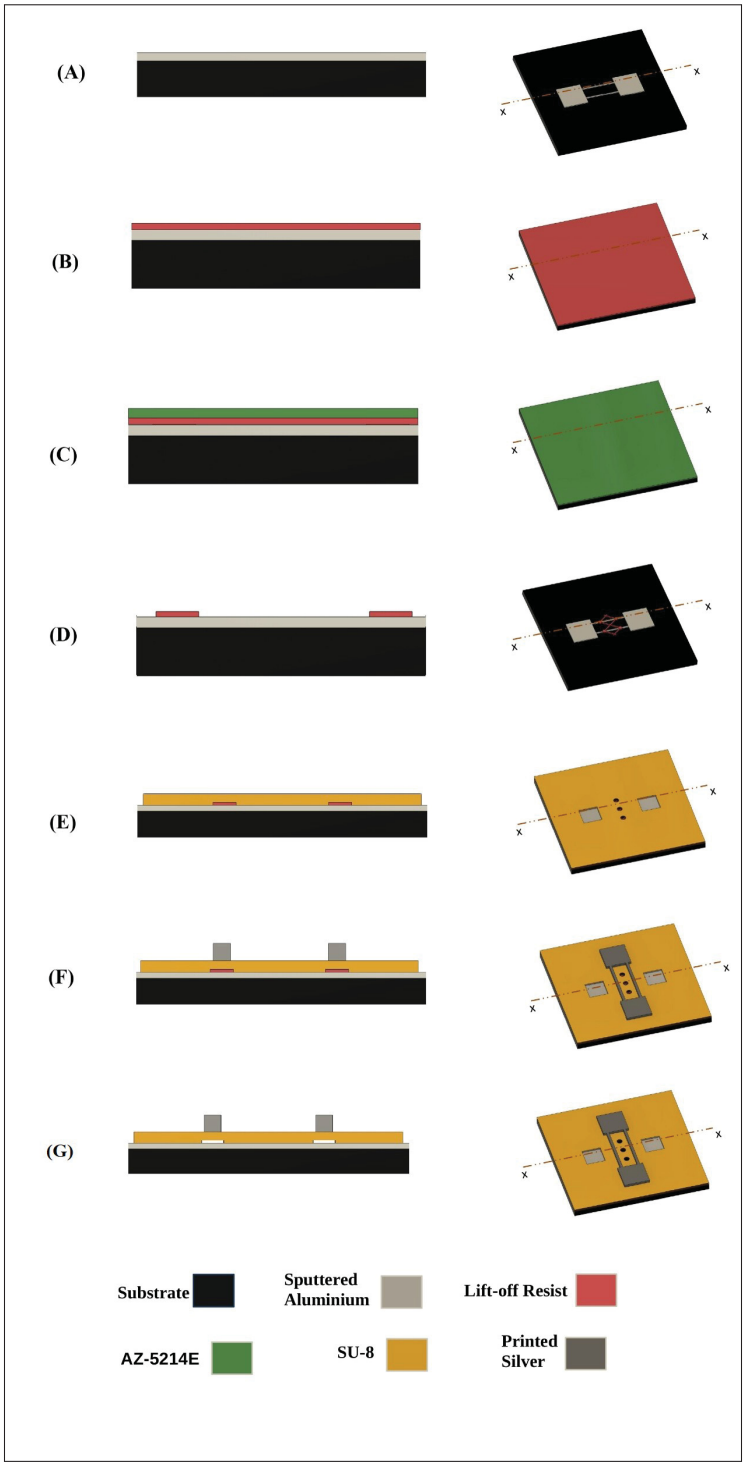

Figure 4.1 Schematic cross-section and plan view of the hybrid CMUT cell

4.6 Unit-Cell Topology and Array Layout

Each CMUT element consists of a parallel-plate cell in which an SU-8 membrane carries a printed top electrode and is suspended above a sputtered Al bottom electrode by an LOR-defined cavity. After release, the cavity forms the electrostatic gap between the two electrodes.

The baseline unit cell is a circular SU-8 plate of diameter 200 µm, spanning a cavity of thickness $g \approx 1.2$ µm, with:

- a continuous bottom Al electrode on glass defining the active area;
- a top printed silver electrode overlapping the central region of the membrane, inset from the rim by a guard band to reduce the risk of edge shorting; and
- an array of etch holes in SU-8 that expose the LOR during the release step.

The main geometric parameters are summarized in Table 4.6. Optical microscope images of the fabricated structures in fig. 4.2 confirm that the realized devices follow the intended layout with SU-8 membranes, printed silver top electrodes, and the designed etch-hole pattern.

Table 4.6 Geometric parameters of the hybrid CMUT design

Parameter	**Value** (µm)
Membrane diameter D	200
SU-8 thickness t_{SU8}	2.2
Gap height g	1.2
LOR thickness t_{LOR}	1.2
Bottom electrode thickness t_{Al}	0.350
Bottom electrode length L_{bot}	2000
Bottom electrode width W_{bot}	75
Printed Ag (top electrode) thickness t_{Ag}	9.2
Top electrode length L_{top}	3500
Top electrode width W_{top}	125
Etch-hole diameter d_h	240
Etch-hole pitch p_h	750
Cell pitch in x, p_x	1000
Cell pitch in y, p_y	750
Array size $N_x \times N_y$	2×2

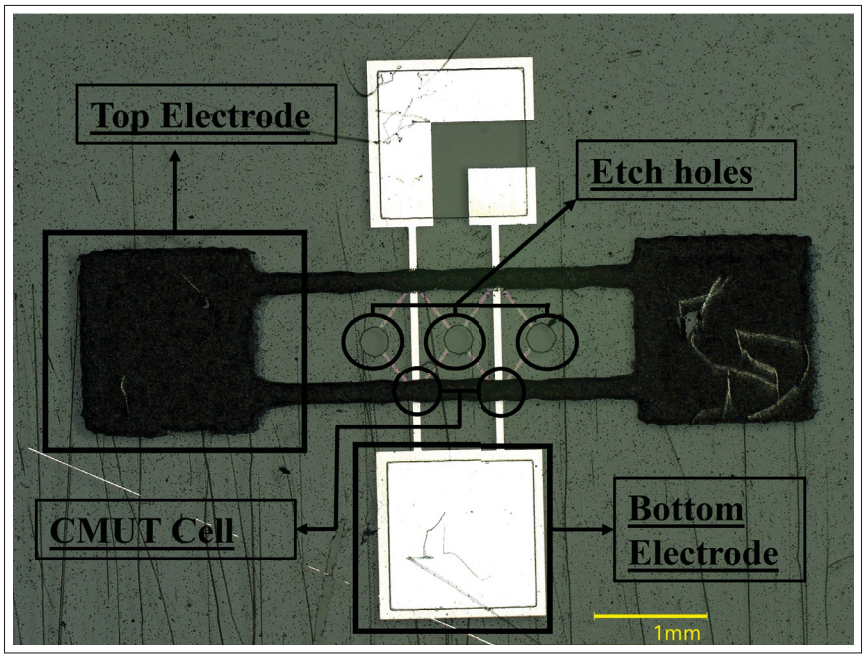

Figure 4.2 Optical microscope image of fabricated hybrid CMUT cell, bottom aluminum electrode, printed silver top electrodes, and etch-hole pattern

4.7 Thickness and Structural Verification

Two simple measurements were performed to verify that the fabricated hybrid CMUTs are close to the intended design.

First, the thickness of the printed silver top electrode was measured using a stylus profilometer on dedicated test lines printed with the same screen and cure conditions as the devices. From several such scans, the printed silver thickness was found to be approximately 9.2 µm, and this value is used in Table 4.6.

Second, the mechanical resonance and operating bias range were checked with laser Doppler vibrometer (LDV). The LDV was focused at the center of a CMUT cell and the out-of-plane vibration was measured while sweeping the drive frequency in air at a DC bias of 3 V and an AC excitation of 8 V_{pp}. Two clear resonance peaks are observed in the spectrum around 1 MHz and 1.41 MHz are shown in fig. 4.3. Lorentzian fits to these two modes yield mechanical quality factors of $Q_1 \approx 171$ and $Q_2 \approx 235$ for the 1 MHz and 1.41 MHz resonances, respectively. It should be noted that the broad bump was under the Peak 1 was not taken into consideration for lorentzian fits. By slowly increasing the dc bias during similar measurements, the membrane was observed to collapse at a bias of approximately 20 V, which is taken as the collapse (pull-in) voltage V_{PI} for the baseline cell. This confirms that the fabricated CMUTs operate in a practical voltage range.

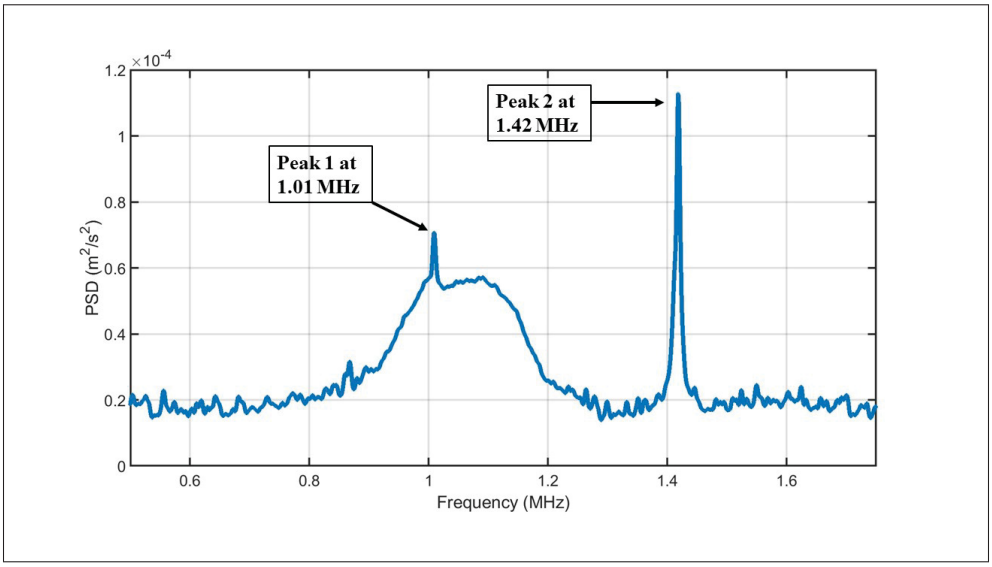

Figure 4.3 Acceleration PSD of a single hybrid CMUT cell in air at 3 V dc bias and 8 V_{pp} ac drive, showing two clear mechanical resonance around 1 MHz and 1.41 MHz

4.8 Summary and Outlook

This chapter has presented the design and implementation of a hybrid CMUT fabrication process that combines surface-micromachined cavity and membrane formation with screen-printed top electrodes. Starting from practical constraints in a university cleanroom and the availability of specific materials (glass substrates, AZ 5214E, LOR, SU-8, and a screen-printable silver ink), the process was developed through a series of trials that exposed the key limitations of fully printed stacks and direct printing on photoresist. These experiments motivated the transition to a smooth sputtered Al bottom electrode, a LOR-based sacrificial layer patterned with AZ 5214E, a SU-8 membrane with etch holes, and a fully cured printed silver top electrode released in a diluted AZ developer.

The resulting flow operates within a well-defined thermal and chemical window, summarized in the compatibility tables, and is compatible with glass substrates and screen printing. The final device architecture, consisting of an SU-8 membrane spanning a LOR-defined gap above a sputtered Al bottom electrode with a printed silver top electrode, was documented through

geometric tables, layout schematics, and photographs of the fabricated structures. Simple profilometer measurements confirmed the printed silver thickness used in the design, and LDV measurements in air showed two clear mechanical resonances around 1.01 MHz and 1.42 MHz, with quality factors of approximately $Q_1 \approx 171$ and $Q_2 \approx 235$ extracted using the half-power bandwidth method, as well as a collapse voltage of approximately 20 V, indicating a practical operating range for the printed CMUT cells.

Overall, this hybrid process provides a reproducible route to CMUT-like capacitive structures using a reduced toolset, limited mask count, and a relaxed thermal budget. It is directly applicable to CMUTs on glass and can be adapted to flexible substrates with appropriate adjustments to fixturing and thermal ramps, offering a platform for future work on low-cost, printed-and-micromachined ultrasonic transducers.

CONCLUSION AND RECOMMENDATIONS

The overarching goal of this thesis was to contribute to the development of micromachined ultrasonic transducers (MUTs) for non-invasive blood-pressure (BP) waveform monitoring. The work was structured around three complementary axes:

- understanding how CMUT topology and anchoring affect quality factor, damping, and nonlinear behavior in a well-controlled silicon MEMS platform;
- critically reviewing the state of the art in ultrasonic BP-waveform sensing, with emphasis on device architectures and performance trade-offs; and
- developing a hybrid fabrication flow that integrates screen-printed conductors with surface-micromachined cavities and membranes, as a low-cost route toward CMUTs on glass and, ultimately, flexible substrates.

Together, this thesis provides both physical insight into CMUT loss mechanisms and a practical process platform for future BP-waveform sensors. In the next sections, the contributions are summarized.

5.1 Summary of contributions

5.1.1 Impact of CMUT Topology on Q-Factor and Damping Mechanisms

Using the PolyMUMPs silicon MEMS process, four CMUT topologies were designed and fabricated with identical active areas but different combinations of arm geometry (spring vs. straight arm) and anchoring (rocker vs. fixed). Laser Doppler vibrometer (LDV) measurements in air and vacuum, under controlled dc bias and ac drive, were used to extract resonance frequency, quality factor, and their dependence on operating point.

A pull-in-normalized common operating point was introduced so that devices with different pull-in voltages could be compared fairly. At this operating point, paired air/vacuum data were analyzed with an additive $1/Q$ model to separate fluidic damping from intrinsic losses. Under vacuum, the four topologies formed a structured set of permutations that allowed the dominant intrinsic loss channels to be decomposed into contributions associated with arm geometry and anchoring.

The main findings can be summarized as follows:

- Rocker anchoring introduces strong intrinsic losses, limiting Q even in vacuum. In the studied devices, moving from rocker to fixed anchoring increased the vacuum quality factor by more than an order of magnitude, indicating that anchor rotation and stem radiation dominate the intrinsic loss budget for rocker designs.
- Under fixed anchoring, straight arms exhibit lower intrinsic losses than spring arms. This is reflected both in higher Q_{vac} and in a reduced thin-film damping share, consistent with reduced bending and hinge losses.
- Combining fixed anchoring with straight arms (topology D) yields the highest Q and the most linear response among the four topologies, whereas the rocker/spring combination (topology A) is deliberately low-Q and strongly nonlinear.

These results provide concrete design guidelines: rocker anchors can be exploited when broad bandwidth and strong tuning are desired, but fixed straight arms are preferable when high Q, quasi-linear response, and efficient transmit/receive operation are required.

5.1.2 Ultrasonic devices for non-invasive BP waveform monitoring

A dedicated literature review analyses ultrasonic sensors for continuous non-invasive BP waveform monitoring. The survey covered:

- the clinical and technical motivation for beat-to-beat BP waveform measurement;
- the basic ultrasound time-of-flight principle and signal-processing models used to recover arterial diameter and pressure from wall motion
- the main transducer families employed to date, including bulk piezoelectric probes, PMUT arrays, and emerging CMUTs; and
- the measurement geometries, packaging strategies, and electronic front-ends used in reported systems.

The review confirms that most existing BP-waveform systems still rely on bulk piezoelectric transducers or PMUTs, often in rigid or semi-rigid probes. CMUT-based solutions remain comparatively rare, and very few works attempt a systematic comparison of CMUT and PMUT architectures for this specific application. There is also limited literature on truly wearable, conformal ultrasonic BP sensors, despite growing interest in flexible substrates for continuous monitoring.

This gap motivates the CMUT-centric approach taken in this thesis and highlights the need for fabrication strategies that can bridge from silicon to polymer platforms without sacrificing device performance.

5.1.3 Hybrid surface-micromachined and screen-printed CMUT process

Building on the insights from silicon CMUTs and the application requirements for BP-waveform sensing, a hybrid fabrication process was developed that combines surface-micromachined cavities and membranes with screen-printed silver electrodes on glass.

The final process flow uses:

- a glass substrate for dimensional stability and compatibility with sputtering, spin coating, and printing;
- a sputtered Al bottom electrode, patterned by AZ 5214E lithography and Al wet etch to define a smooth reference plane for the gap;
- a LOR sacrificial layer patterned using AZ 5214E, with LOR providing the main cavity thickness and remaining soluble in diluted AZ developer;
- a SU-8 membrane spanning the LOR cavity and patterned with etch holes to access the sacrificial layer; and
- a fully cured screen-printed silver top electrode on SU-8, which tolerates the required cure temperature.

Temperature and chemical compatibility were studied in detail, leading to a process window in which AZ 5214E is always stripped before high-temperature steps, LOR remains releasable under SU-8, and the printed silver ink withstands the final developer-based release without degradation. A diluted AZ developer (1:1) was ultimately selected to release the devices, after stripper and MF-319 based releases were found to attack the printed silver and sputtered Al, respectively.

A 2×2 array of circular CMUT-like cells was fabricated on glass. Stylus profilometer on dedicated test lines confirmed a printed silver thickness of approximately $9.2\,\mu\text{m}$, while SU-8 and LOR thicknesses were kept in the $2.2\,\mu\text{m}$ and $1.2\,\mu\text{m}$ range, respectively. LDV measurements in air on a baseline cell biased at 3 V with an ac drive of $8\,V_{pp}$ revealed two clear mechanical resonances at 1.01 MHz and 1.42 MHz, with quality factors of approximately $Q_1 \approx 171$ and $Q_2 \approx 235$ extracted using the half-power bandwidth method. By increasing the dc bias under similar conditions, the membrane was observed to collapse at approximately 20 V, confirming

both the structural integrity of the hybrid devices and their suitability for MHz-range ultrasound operation at practical voltages.

Taken together, this work demonstrates that CMUT-like structures can be realized using a reduced toolset that integrates printing and micromachining, providing a stepping stone toward low-cost or flexible CMUT arrays.

5.2 Limitations

Several limitations of the present work should be noted:

- The CMUT topology study was performed on a specific PolyMUMPs design set, with fixed membrane dimensions and gap thickness. While the trends in Q and damping decomposition are expected to generalize, absolute values and optimal choices will depend on geometry and operating frequency.
- The ultrasonic BP-waveform review, although broad, is necessarily constrained by the available literature and does not include a head-to-head experimental comparison of different transducer families on the same platform.
- The hybrid process was demonstrated on glass substrates with a relatively small array and primarily mechanical characterization. Electrical, acoustic, and long-term reliability testing, as well as in-liquid operation, remain to be explored.
- The hybrid CMUT structures fabricated in this work were not yet integrated into a full BP-waveform measurement chain, and no in-vitro or in-vivo BP experiments were performed within the scope of the thesis.

These limitations motivate several directions for future research. In the following sections we make the recommendations for future works.

5.3 Recommendations and Future work

5.3.1 CMUT design and damping engineering

- Extend the damping decomposition framework to a broader range of CMUT geometries (different radii, aspect ratios, and cell pitches) and to operation in liquid or tissue-mimicking phantoms, where fluidic losses and radiation into the load become more complex.
- Incorporate more detailed anchor-loss and thermoelastic damping models into the design flow, using finite-element methods calibrated by systematic measurements across bias, drive, and environment.
- Explore intermediate anchoring schemes like partial compliance to deliberately trade off Q and bandwidth for specific imaging or sensing tasks.

5.3.2 Hybrid process and materials

- Transfer the hybrid process to flexible polymer substrates (e.g. kapton or PET), with attention to thermal ramps, adhesion promotion, and wafer handling. This will enable conformal CMUT arrays for wearable BP sensing.
- Investigate alternative printed conductors and dielectrics with lower curing temperatures and improved chemical stability, potentially relaxing the process window and widening material choices.
- Integrate other printing technologies like inkjet and micro-dispensing to be able to decrease feature size and minimum thickness of layers.

5.4 Broader perspectives

Beyond BP-waveform monitoring, the tools and concepts developed in this thesis could be applied to other ultrasonic sensing problems where low-cost, conformal CMUT arrays are advantageous, such as vascular access guidance, respiratory monitoring, or structural health monitoring on curved surfaces. The combination of damping-aware CMUT design and hybrid printed–micromachined fabrication offers a flexible foundation for such future developments.

APPENDIX I

COMMON OPERATING POINT AND Q-FACTOR EXTRACTION

To enable a fair comparison of the quality factor across CMUT topologies with different pull-in voltages V_{PI} and non-identical $(V_{\mathrm{pp}}, V_{\mathrm{dc}})$ measurement grids in air and vacuum, we impose a unified normalization procedure. We (i) fix a common reduced dc bias relative to V_{PI}, (ii) normalize the AC drive by the remaining pull-in margin, (iii) restrict the analysis to the strict intersection of the feasible $(V_{\mathrm{pp}}, V_{\mathrm{dc}})$ windows in both environments, and (iv) use only bracketed linear interpolation of measured Q values within this intersection. The following subsections detail the construction of this operating point and the corresponding Q-factor extraction.

1. Q Figures of Merit and Partition

We adopt the additive-loss model represented by eq. A I-1, A I-2 and A I-3

$$\frac{1}{Q_{\mathrm{air}}} = \frac{1}{Q_{\mathrm{vac}}} + \frac{1}{Q_{\mathrm{SFD}}}, \tag{A I-1}$$

$$R_Q = \frac{Q_{\mathrm{vac}}}{Q_{\mathrm{air}}}, \tag{A I-2}$$

$$\mathrm{SFD}\% = 100\left(1 - \frac{Q_{\mathrm{air}}}{Q_{\mathrm{vac}}}\right). \tag{A I-3}$$

where $\frac{1}{Q_{\mathrm{air}}}$ is the total damping in the system in air, $\frac{1}{Q_{\mathrm{vac}}}$ is the intrinsic damping component and $\frac{1}{Q_{\mathrm{SFD}}}$ is the squeeze film damping component.

For visualization we use the partition $1/Q_{\mathrm{vac}}$ (intrinsic) and $1/Q_{\mathrm{SFD}} = 1/Q_{\mathrm{air}} - 1/Q_{\mathrm{vac}}$.

2. Normalizations

We perform the normalization of the bias voltages and signal voltages for each device as shown in eq. A I-4, A I-5, A I-6 and A I-7. All the terms are defined in the table I-1.

$$\hat{V}_{\mathrm{DC}} = \frac{{V_{\mathrm{DC}}}^{\star}}{V_{\mathrm{PI}}}, \tag{A I-4}$$

$${V_{\mathrm{DC}}}^{\star} = \hat{V}_{\mathrm{DC}}\, V_{\mathrm{PI}}, \tag{A I-5}$$

$$\hat{V}_{\mathrm{pp}} = \frac{(V_{\mathrm{pp}}/2)}{V_{\mathrm{PI}} - V_{\mathrm{dc}}^{\star}} = \frac{V_{\mathrm{pp}}}{2\,(V_{\mathrm{PI}} - V_{\mathrm{DC}}^{\star})}, \tag{A I-6}$$

$$V_{\mathrm{pp}} = 2\,\hat{V}_{\mathrm{pp}}\,(V_{\mathrm{PI}} - V_{\mathrm{DC}}^{\star}). \tag{A I-7}$$

Thus $\hat{V}_{\mathrm{pp}}$ is the fraction of the remaining pull-in margin used by the AC peak amplitude; it is dimensionless and comparable across devices.

Table-A I-1 Symbols used in the normalization and Q analysis.

Symbol	Meaning	Units
V_{PI}	Pull-in voltage of the device (measured per CMUT)	V
V_{dc}	Applied DC bias during a sweep (measured per CMUT)	V
$\hat{V}_{\mathrm{dc}}$	Normalized DC bias, $V_{\mathrm{dc}}/V_{\mathrm{PI}}$	–
$V_{\mathrm{dc}}^{\dagger}$	DC bias operating point	–
$V_{\mathrm{dc}}^{\star}$	Target DC bias at common operating point	V
V_{pp}	AC drive, peak-to-peak amplitude	V
$\hat{V}_{\mathrm{pp}}$	Normalized AC drive, $\frac{(V_{\mathrm{pp}}/2)}{V_{\mathrm{PI}} - V_{\mathrm{dc}}^{\star}}$ (Equation (A I-6))	–
$V_{\mathrm{pp}}^{\dagger}$	Signal voltage operating point	–
$V_{\mathrm{pp}}^{\star}$	Target signal voltage at common operating point	V
Q_{air}	Quality factor measured in air at $(\hat{V}_{\mathrm{dc}}, \hat{V}_{\mathrm{pp}})$	–
Q_{vac}	Quality factor measured in vacuum at the same point	–
Q_{SFD}	Squeeze-film damping Q (from additive model)	–
R_Q	Vacuum-recovery ratio, $Q_{\mathrm{vac}}/Q_{\mathrm{air}}$	–
SFD%	Air-loss share, $100\left(1 - \frac{Q_{\mathrm{air}}}{Q_{\mathrm{vac}}}\right)$	%
f_0 (optional)	Resonant frequency at the operating point	Hz
Env. $\in$ {air, vac}	Measurement environment indicator	–
Device $\in$ {A, B, C, D}	CMUT label / topology (arms, anchor)	–

3. Data Conditioning

1. Parse $(V_{\mathrm{pp}}, V_{\mathrm{dc}})$ from the CSV file with columns "V_{pp}" and V_{dc}.

2. Remove obvious off-resonance points using a pre-registered rule (e.g., $Q_{\mathrm{vac}} < 5$).

4. Bias Alignment (Interpolation in V_{dc})

We fix $\hat{V}_{\mathrm{dc}} = 0.269$ for all devices and compute $V_{\mathrm{dc}}^{\star}$ from (A I-5). For each device k and environment $e \in \{\mathrm{air}, \mathrm{vac}\}$ and each measured V_{pp}:

$$Q(V_{\mathrm{dc}}^{\star} \mid V_{\mathrm{pp}}) = Q_0 + \frac{Q_1 - Q_0}{V_{\mathrm{dc},1} - V_{\mathrm{dc},0}} \left(V_{\mathrm{dc}}^{\star} - V_{\mathrm{dc},0}\right),$$

using the two nearest V_{dc} neighbors that bracket $V_{\mathrm{dc}}^{\star}$. Then convert the measured V_{pp} points across the dataset for each device to $\hat{V}_{\mathrm{pp}}$ with Equation (A I-6). The result is a set $\{(\hat{V}_{\mathrm{pp}}, Q)\}$ at a common reduced bias for each device and environment.

5. Window Intersection and Target Selection

For each device k and environment, compute its feasible normalized-drive range $[\hat{V}_{\mathrm{pp},k}^{\min}, \hat{V}_{\mathrm{pp},k}^{\max}]$. For a device set $\mathcal{K}$ (e.g., A–B–D), the admissible comparison window is the intersection

$$\left[\hat{V}_{pp}^{\mathrm{low}},\ \hat{V}_{pp}^{\mathrm{high}}\right] = \left(\bigcap_{k\in\mathcal{K}} \left[\hat{V}_{pp,k,\mathrm{air}}^{\min},\ \hat{V}_{pp,k,\mathrm{air}}^{\max}\right]\right) \tag{A I-8}$$

$$\cap \left(\bigcap_{k\in\mathcal{K}} \left[\hat{V}_{pp,k,\mathrm{vac}}^{\min},\ \hat{V}_{pp,k,\mathrm{vac}}^{\max}\right]\right). \tag{A I-9}$$

In Figure I-1, X-axis represents the normalized bias voltages (V_{dc}) across the measurement range for each device. A common normalized bias was chosen within the overlap of all devices normalized measurement ranges. At this common normalized bias we set the operating point for the DC bias given by $V_{\mathrm{dc}}^{\dagger}$. We choose a target $\hat{V}_{\mathrm{pp}}$ inside this interval. In our dataset, a strict common window exists for A–B–D; we selected the low end $V_{\mathrm{pp}}^{\dagger} = 0.026$ to remain in the deepest small-signal regime. A four-way (A–B–C–D) intersection is not available at this bias; pairwise results including C are reported separately.

6. Q Extraction at the target operating point

Interpolate Q vs. $\hat{V}_{\text{pp}}$ at $V_{\text{dc}}^{\star}$ to $V_{\text{pp}}^{\dagger}$ with two nearest neighbors for all CMUT devices.

We then extract Q_{vac} and Q_{SFD} % using Equation (A I-1) and compute R_Q and SFD%.

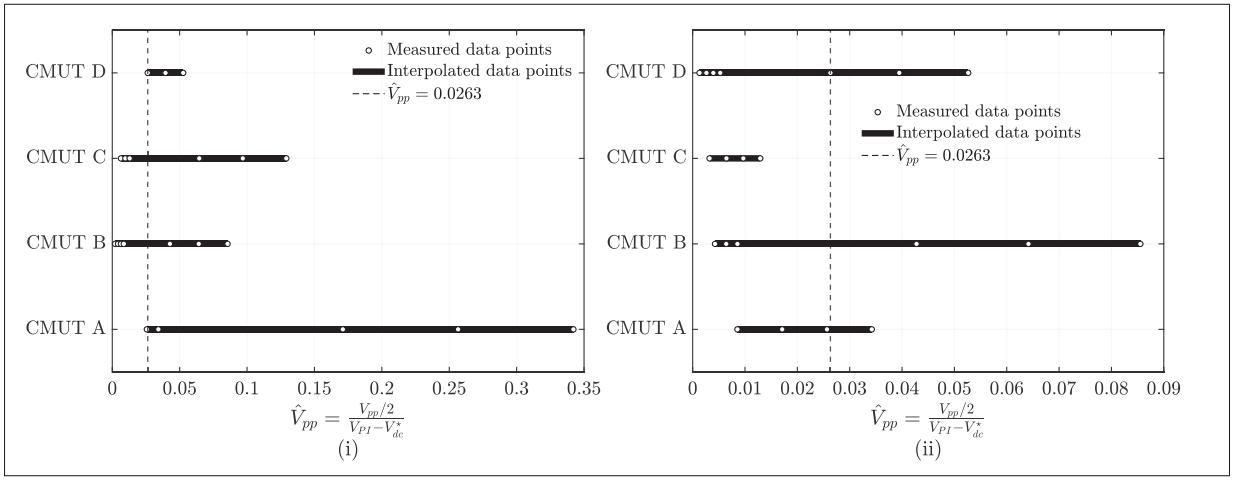

Figure-A I-1 Normalized AC drive range $\hat{V}_{pp}$ for CMUTs A–D in (i) air and (ii) vacuum at a common normalized bias $\hat{V}_{dc}$ = 0.2692. Solid horizontal bars indicate the accessible $\hat{V}pp$ interval per device, open circles mark all evaluated operating points, and the vertical dashed line denotes the selected common $\hat{V}_{pp}$ used for cross-device

LIST OF BIBLIOGRAPHIC REFERENCES

Regulation - 2017/745 - EN - Medical Device Regulation - EUR-Lex. Consulted at https://eur-lex.europa.eu/eli/reg/2017/745/oj.

(2021). Cardiovascular diseases (CVDs). World Health Organization. Consulted at https://www.who.int/news-room/fact-sheets/detail/cardiovascular-diseases-(cvds).

Adelegan, O. J., Yamaner, F. Y. & Oralkan, O. (2018a). Design and Implementation of Wideband CMUTs for Airborne Applications—Preliminary Results. Proc. IEEE Int. Ultrasonics Symposium (IUS), pp. 1–4. doi: 10.1109/ULTSYM.2018.8579680.

Adelegan, O. J., Yamaner, F. Y. & Oralkan, (2018b). Design and Implementation of Wideband CMUTs for Airborne Applications - Preliminary Results. IEEE International Ultrasonics Symposium, IUS, 2018-October. doi: 10.1109/ULTSYM.2018.8579680.

Akasheh, F., Myers, T., Fraser, J. D., Bose, S. & Bandyopadhyay, A. (2004). Development of piezoelectric micromachined ultrasonic transducers. Sensors and Actuators, A: Physical, 111(2-3), 275–287. doi: 10.1016/j.sna.2003.11.022.

Algamili, A. S., Khir, M. H. M., Dennis, J. O., Ahmed, A. Y., Alabsi, S. S., Ba Hashwan, S. S. & Junaid, M. M. (2021). A Review of Actuation and Sensing Mechanisms in MEMS-Based Sensor Devices. Nanoscale Research Letters, 16(1), 1–21. doi: 10.1186/S11671-021-03481-7/TABLES/1.

Amado-Rey, A. B., GoncalvesSeabra, A. C. & Stieglitz, T. (2024). Towards ultrasound wearable technology for cardiovascular monitoring: from device development to clinical validation. IEEE Reviews in Biomedical Engineering. doi: 10.1109/RBME.2024.3410399.

Apte, N., Park, K. K., Nikoozadeh, A. & Khuri-Yakub, B. T. (2014a). Bandwidth and Sensitivity Optimization in CMUTs for Airborne Applications. Proc. IEEE Int. Ultrasonics Symposium (IUS), pp. 166–169. doi: 10.1109/ULTSYM.2014.0042.

Apte, N., Park, K. K., Nikoozadeh, A. & Khuri-Yakub, B. T. (2014b). Bandwidth and sensitivity optimization in CMUTs for airborne applications. IEEE International Ultrasonics Symposium, IUS, 166–169. doi: 10.1109/ULTSYM.2014.0042.

Athaya, T. & Choi, S. (2022). A Review of Noninvasive Methodologies to Estimate the Blood Pressure Wav Sensors. MDPI. doi: 10.3390/s22103953.

Badry, R., Ibrahim, A., Gamal, F., Shehata, D., Ezzat, H. & Elhaes, H. (2020). Electronic Properties of Polyvinyl Alcohol/ TiO 2 /SiO 2 Nanocomposites. doi: 10.33263/BRIAC105.64276435.

Bank, A. J., Kaiser, D. R., Rajala, S. & Cheng, A. (1999). In vivo human brachial artery elastic mechanics: Effects of smooth muscle relaxation. Circulation, 100(1), 41–47. doi: 10.1161/01.CIR.100.1.41,.

Bao, M. & Yang, H. (2007a). Squeeze Film Air Damping in MEMS. Sensors and Actuators A: Physical, 136(1), 3–27. doi: 10.1016/j.sna.2007.01.008.

Bao, M. & Yang, H. (2007b). Squeeze Film Air Damping in MEMS. Sensors and Actuators A: Physical, 136(1), 3–27. doi: 10.1016/j.sna.2007.01.008.

Bao, M. & Yang, H. (2007c). Squeeze film air damping in MEMS. Sensors and Actuators A: Physical, 136(1), 3–27. doi: 10.1016/j.sna.2007.01.008.

Bayda, S., Adeel, M., Tuccinardi, T., Cordani, M. & Rizzolio, F. (2019). The history of nanoscience and nanotechnology: From chemical-physical applications to nanomedicine. U.S. National Library of Medicine. Consulted at https://www.ncbi.nlm.nih.gov/pmc/articles/PMC6982820/.

Bayram, B., Oralkan, , Ergun, A. S., Hæggström, E., Yaralioglu, G. G. & Khuri-Yakub, B. T. (2005). Capacitive micromachined ultrasonic transducer design for high power transmission. IEEE Transactions on Ultrasonics, Ferroelectrics, and Frequency Control, 52(2), 326–338. doi: 10.1109/TUFFC.2005.1406558.

Belgacem, B., Calame, F. & Muralt, P. (2005). Design, modeling and fabrication of piezoelectric Micromachined Ultrasonic Transducers.

Benetos, A., Laurent, S., Hoeks, A. P., Boutouyrie, P. H. & Safar, M. E. (1993). Arterial alterations with aging and high blood pressure. A noninvasive study of carotid and femoral arteries. Arteriosclerosis, Thrombosis, and Vascular Biology, 13(1), 90–97. doi: 10.1161/01.ATV.13.1.90,.

Beyaz, M. (2021). An acoustic blood pressure sensing scheme using time of flight and shear wave elastography techniques. Sensors and Actuators A: Physical, 330, 112865. doi: 10.1016/J.SNA.2021.112865.

Biriukov, A. E. & Korsunsky, A. M. (2024). Methods of fabrication and modeling of CMUTs – A review. Sensors and Actuators A: Physical, 379, 115914. doi: 10.1016/J.SNA.2024.115914.

Biriukov, S. V. & Zelenina, N. K. (2024). Methods of fabrication and modeling of CMUTs. Sensors and Actuators A: Physical, 366, 115914. doi: 10.1016/j.sna.2024.115914.

Birjis, Y., Swaminathan, S., Nazemi, H., Raj, G. C. A., Munirathinam, P., Abu-Libdeh, A. & Emadi, A. (2022). Piezoelectric Micromachined Ultrasonic Transducers (PMUTs): Performance Metrics, Advancements, and Applications. Sensors 2022, Vol. 22, Page 9151, 22(23), 9151. doi: 10.3390/S22239151.

Brenner, K., Ergun, A. S., Firouzi, K., Rasmussen, M. F., Stedman, Q. & Khuri-Yakub, B. (2019). Advances in Capacitive Micromachined Ultrasonic Transducers. Micromachines 2019, Vol. 10, Page 152, 10(2), 152. doi: 10.3390/MI10020152.

Brown, J., Sharma, S., Leadbetter, J., Cochran, S. & Adamson, R. (2014). Mass-spring matching layers for high-frequency ultrasound transducers: A new technique using vacuum deposition. IEEE Transactions on Ultrasonics, Ferroelectrics, and Frequency Control, 61(11), 1911–1921. doi: 10.1109/TUFFC.2014.006480.

C Bramwell, M. J., Hill, A. V., Crighton B ram ell, B. J. & H ill, A. V. (1922). The velocity of pulse wave in man. Proceedings of the Royal Society of London. Series B, Containing Papers of a Biological Character, 93(652), 298–306. doi: 10.1098/RSPB.1922.0022.

Caliano, G., Matrone, G. & Savoia, A. S. (2017). Biasing of capacitive micromachined ultrasonic transducers. IEEE Transactions on Ultrasonics, Ferroelectrics, and Frequency Control, 64(2), 402–413. doi: 10.1109/TUFFC.2016.2623221.

Chen, J., Fei, C., Lin, D., Gao, P., Zhang, J., Quan, Y., Chen, D., Li, D. & Yang, Y. T. (2022). A Review of UltraHigh Frequency Ultrasonic Transducers. Frontiers in Materials, 8, 733358. doi: 10.3389/FMATS.2021.733358/BIBTEX.

Cho, S. A., Jang, Y. E., Ji, S. H., Kim, E. H., Lee, J. H., Kim, H. S. & Kim, J. T. (2021). Ultrasound-guided arterial catheterization. Anesthesia and Pain Medicine, 16(2), 119. doi: 10.17085/APM.21012.

Chorsi, M. T., Curry, E. J., Chorsi, H. T., Das, R., Baroody, J., Purohit, P. K., Ilies, H. & Nguyen, T. D. (2019). Piezoelectric Biomaterials for Sensors and Actuators. Advanced Materials, 31(1). doi: 10.1002/ADMA.201802084.

Chow, C. K., Teo, K. K., Rangarajan, S., Islam, S., Gupta, R., Avezum, A., Bahonar, A., Chifamba, J., Dagenais, G., Diaz, R., Kazmi, K., Lanas, F., Wei, L., Lopez-Jaramillo, P., Fanghong, L., Ismail, N. H., Puoane, T., Rosengren, A., Szuba, A., Temizhan, A., Wielgosz, A., Yusuf, R., Yusufali, A., McKee, M., Liu, L., Mony, P. & Yusuf, S. (2013). Prevalence, awareness, treatment, and control of hypertension in rural and urban communities in high-, middle-, and low-income countries. JAMA, 310(9), 959–968. doi: 10.1001/JAMA.2013.184182.

Cinthio, M., Jansson, T., Ahlgren, R., Lindström, K. & Persson, H. W. (2010). A method for arterial diameter change measurements using ultrasonic B-mode data. Ultrasound in Medicine and Biology, 36(9), 1504–1512. doi: 10.1016/j.ultrasmedbio.2010.05.022.

Cochran, S. (2012). Piezoelectricity and basic configurations for piezoelectric ultrasonic transducers. Ultrasonic Transducers: Materials and Design for Sensors, Actuators and Medical Applications, 3–35. doi: 10.1533/9780857096302.1.3.

Cootney, R. W. & Coatney, R. W. (2001). Ultrasound Imaging: Principles and Applications in Rodent Research. ILAR Journal, 42(3), 233–247. doi: 10.1093/ILAR.42.3.233.

Cowen, A., Benidt, G. H., Hardy, B. & Smith, B. W. (1992). PolyMUMPs: A standard surface-micromachining process for MEMS. Proceedings of SPIE, 2639, 76–83.

Demirci, U., Ergun, A., Oralkan, O., Karaman, M. & Khuri-Yakub, B. (2004). Forward-viewing CMUT arrays for medical imaging. IEEE Transactions on Ultrasonics, Ferroelectrics and Frequency Control, 51(7), 887–895. doi: 10.1109/tuffc.2004.1320749.

Ding, Q., Wang, H., Zhang, H., Huang, X., Sun, X., Qin, Z., Ren, R., Zhu, J., He, C. & Zhang, W. (2021). Research on Novel CMUTs for Detecting Micro-Pressure with Ultra-High Sensitivity and Linearity. Micromachines 2021, Vol. 12, Page 1340, 12(11), 1340. doi: 10.3390/MI12111340.

Dohi, K., Onishi, K., Gorcsan, J., López-Candales, A., Takamura, T., Ota, S., Yamada, N. & Ito, M. (2008). Role of Radial Strain and Displacement Imaging to Quantify Wall Motion Dyssynchrony in Patients With Left Ventricular Mechanical Dyssynchrony and Chronic Right Ventricular Pressure Overload. The American Journal of Cardiology, 101(8), 1206–1212. doi: 10.1016/J.AMJCARD.2007.11.077.

Domagała, Z., Grzelak, J., Pospiech, N., Hunter, N., Klekowski, J., Lach, A., Stój, K., Kurc-Darak, B. & Trzaska, M. (2021). Ultrasound evaluation of the radial artery in young adults — A pilot study. Annals of Anatomy, 238. doi: 10.1016/j.aanat.2021.151763.

Drinkwater, B. W. & Wilcox, P. D. (2006). Ultrasonic arrays for non-destructive evaluation: A review. NDT & E International, 39(7), 525–541. doi: 10.1016/J.NDTEINT.2006.03.006.

Ergun, A. S., Yaralioglu, G. G. & Khuri-Yakub, B. T. (2003). Capacitive Micromachined Ultrasonic Transducers: Theory and Technology. Journal of Aerospace Engineering, 16(2), 76–84. doi: 10.1061/(ASCE)0893-1321(2003)16:2(76).

Fedorov, S. A., Engelsen, N. J., Ghadimi, A. H., Bereyhi, M. J., Schilling, R., Wilson, D. J. & Kippenberg, T. J. (2019). Generalized dissipation dilution in strained mechanical resonators. Phys. Rev. B, 99, 054107. doi: 10.1103/PhysRevB.99.054107.

Fernandez, L. J. (2024). Renal Ultrasound in Arterial Systemic Hypertension. Journal of Radiological Science, 49(1), 26–32. doi: 10.4103/JRADIOLSCI.JRADIOLSCI-D-23-00036.

Foiret, J., Cai, X., Bendjador, H., Park, E. Y., Kamaya, A. & Ferrara, K. W. (2022). Improving plane wave ultrasound imaging through real-time beamformation across multiple arrays. Scientific Reports, 12(1), 1–14. doi: 10.1038/S41598-022-16961-2;SUBJMETA=166,25,3927,639,766,985;KWRD=ACOUSTICS,BIOMEDICAL+ENGINEERING.

Forouzanfar, M. H. & Alexander, e. a. (2015). Global, regional, and national comparative risk assessment of 79 behavioural, environmental and occupational, and metabolic risks or clusters of risks in 188 countries, 1990-2013: A systematic analysis for the Global Burden of Disease Study 2013. The Lancet, 386(10010), 2287–2323. doi: 10.1016/S0140-6736(15)00128-2.

Frangi, A., Cremonesi, M., Jaakkola, A. & Pensala, T. (2013). Analysis of anchor and interface losses in piezoelectric MEMS resonators. Sens. Actuators A, 190, 28–35. doi: 10.1016/j.sna.2012.10.022.

Gaudin, V. (2019). Receptor-based electrochemical biosensors for the detection of contaminants in food products. Electrochemical Biosensors, 307–365. doi: 10.1016/B978-0-12-816491-4.00011-5.

Gavish, B. & Izzo, J. L. (2016). Arterial Stiffness: Going a Step Beyond. American Journal of Hypertension, 29(11), 1223–1233. doi: 10.1093/AJH/HPW061.

Gerardo, C. D., Cretu, E. & Rohling, R. (2018). Fabrication and testing of polymer-based capacitive micromachined ultrasound transducers for medical imaging. Microsystems and Nanoengineering, 4(1), 1–12. doi: 10.1038/S41378-018-0022-5;SUBJMETA=166,350,511,639,925,927,987;KWRD=ELECTRICAL+AND+ELECTRONIC+ENG

Ghavami, M., Sobhani, M. R. & Zemp, R. (2023). Transparent Dual-Frequency CMUT Arrays for Photoacoustic Imaging. IEEE Transactions on Ultrasonics, Ferroelectrics, and Frequency Control, 70(12), 1621–1630. doi: 10.1109/TUFFC.2023.3331356.

Giannattasio, C., Cesana, F., Maestroni, S., Salvioni, A., Maloberti, A., Nava, S., Cairo, M., Madotto, F., Zerboni, F., Sironi, S., Grassi, G. & Mancia, G. (2011). Comparison of Echotracking and Magnetic Resonance Assessment of Abdominal Aorta Distensibility and Relationships with Pulse Wave Velocity. Ultrasound in Medicine & Biology, 37(12), 1970–1976. doi: 10.1016/J.ULTRASMEDBIO.2011.09.009.

Giudici, A., Palombo, C., Morizzo, C., Kozakova, M., Cruickshank, J. K., Wilkinson, I. B. & Khir, A. W. (2021). Transfer-function-free technique for the noninvasive determination of the human arterial pressure waveform. Physiological Reports, 9(18), e15040. doi: 10.14814/PHY2.15040.

Goel, C., Cicek, P.-V. & Robichaud, A. (2022a). Design and Implementation of Low-Voltage Tunable Capacitive Micro-Machined Transducers (CMUT) for Portable Applications. Micromachines, 13(10), 1598. doi: 10.3390/mi13101598.

Goel, C., Cicek, P. V. & Robichaud, A. (2022b). Design and Implementation of Low-Voltage Tunable Capacitive Micro-Machined Transducers (CMUT) for Portable Applications. Micromachines 2022, Vol. 13, Page 1598, 13(10), 1598. doi: 10.3390/MI13101598.

Goel, C., Cicek, P.-V. & Robichaud, A. (2022c). Design and implementation of low-voltage tunable capacitive micro-machined transducers (CMUT) for portable applications. Micromachines, 13(10), 1598. doi: 10.3390/mi13101598.

Goel, C., Gratuze, M., Robichaud, A., Izquierdo, R. & Cicek, P.-V. (2025). A Method for Expanding the Bandwidth and Decreasing the Actuation Voltage of CMUT Devices. IEEE Sensors Letters, 9(10), 1-4. doi: 10.1109/LSENS.2025.3603120.

Goncalves Seabra, A. C., Silva, A. F. D., Stieglitz, T. & Amado-Rey, A. B. (2022). In Silico Blood Pressure Models Comparison. IEEE Sensors Journal, 22(23), 23486–23493. doi: 10.1109/JSEN.2022.3215597.

Goss, S. A., Johnston, R. L. & Dunn, F. (1978). Comprehensive compilation of empirical ultrasonic properties of mammalian tissues. The Journal of the Acoustical Society of America, 64(2), 423–457. doi: 10.1121/1.382016.

Granata, A., Fiorini, F., Andrulli, S., Logias, F., Gallieni, M., Romano, G., Sicurezza, E. & Fiore, C. E. (2009). Doppler ultrasound and renal artery stenosis: An overview. Journal of Ultrasound, 12(4), 133. doi: 10.1016/J.JUS.2009.09.006.

Guldiken, R. O., Zahorian, J., Yamaner, F. Y. & Degertekin, F. L. (2009). Dual-electrode CMUT with non-uniform membranes for high electromechanical coupling coefficient and high bandwidth operation. IEEE Transactions on Ultrasonics, Ferroelectrics, and Frequency Control, 56(6), 1270–1276. doi: 10.1109/TUFFC.2009.1169.

Gurun, G., Tekes, C., Zahorian, J., Xu, T., Satir, S., Karaman, M., Hasler, J. & Degertekin, F. L. (2014). Single-chip CMUT-on-CMOS front-end system for real-time volumetric IVUS and ICE imaging. IEEE Transactions on Ultrasonics, Ferroelectrics, and Frequency Control, 61(2), 239–250. doi: 10.1109/TUFFC.2014.6722610,.

Hanya, S. (2013). Validity of the Water Hammer Formula for Determining Regional Aortic Pulse Wave Velocity: Comparison of One-Point and Two-Point (Foot-to-Foot) Measurements Using a Multisensor Catheter in Human. Annals of vascular diseases, 6(2), 150–158. doi: 10.3400/AVD.OA.13-00046.

He, Y., Wan, H., Jiang, X. & Peng, C. (2022). Piezoelectric micromachined Ultrasound Transducer Technology: Recent advances and applications. Biosensors, 13(1), 55. doi: 10.3390/bios13010055.

Herrera-May, A. L., Soler-Balcazar, J. C., Vázquez-Leal, H., Martínez-Castillo, J., Vigueras-Zuñiga, M. O. & Aguilera-Cortés, L. A. (2016). Recent advances of MEMS resonators for Lorentz force based magnetic field sensors: Design, applications and challenges. Sensors (Switzerland), 16(9). doi: 10.3390/S16091359.

Hoeks, A. P. G. (1993). Non-invasive study of the local mechanical arterial characteristics in humans. 119–134. doi: 10.1007/978-94-011-0900-0{_}9.

Hu, H., Huang, H., Li, M. et al. (2023). A wearable cardiac ultrasound imager. Nature, 613, 667–675. Consulted at https://www.nature.com/articles/s41586-022-05498-z.

Huang, L., Zhao, P., Liang, F. & Wang, W. (2018). Single-cell 3D electro-rotation. Methods in Cell Biology, 148, 97–116. doi: 10.1016/BS.MCB.2018.06.013.

Huang, X., Wang, H. & Yu, L. (2021). Investigation on Design Theory and Performance Analysis of Vacuum Capacitive Micromachined Ultrasonic Transducer. Micromachines 2021, Vol. 12, Page 1127, 12(9), 1127. doi: 10.3390/MI12091127.

Ichinose, D., Shimizu, T., Sakata, O., Yamada, T., Ehara, Y. & Funakubo, H. (2021). Domain structure transition in compressively strained (100)/(001) epitaxial tetragonal PZT film. Journal of Applied Physics, 129(2), 24101. doi: 10.1063/5.0031803/1025605.

Jiang, X., Kim, K., Zhang, S., Johnson, J. & Salazar, G. (2014). High-Temperature Piezoelectric Sensing. Sensors, 14, 144–169. doi: 10.3390/s140100144.

Jiang, X., Tang, H. Y., Lu, Y., Ng, E. J., Tsai, J. M., Boser, B. E. & Horsley, D. A. (2017). Ultrasonic Fingerprint Sensor with Transmit Beamforming Based on a PMUT Array Bonded to CMOS Circuitry. IEEE Transactions on Ultrasonics, Ferroelectrics, and Frequency Control, 64(9), 1401–1408. doi: 10.1109/TUFFC.2017.2703606.

Jiménez, N. et al. (2024). Resonance sonomanometry for noninvasive, continuous blood pressure measurement. PNAS Nexus. doi: 10.1093/pnasnexus/pgae252.

José Horst, D., Paulo Andrade Junior, P., De Almeida Vieira, R., Paulo de Andrade Junior, P., Adriano Duvoisin, C. & de Almeida Vieira, R. (2020). Fabrication of Conductive Filaments for 3D-printing: Polymer Nanocomposites Gestão do conhecimento e da inovação em organizações View project Metal alloys View project Fabrication of Conductive Filaments for 3D-printing: Polymer Nanocomposites. doi: 10.33263/BRIAC106.65776586.

Joseph, J., Nabeel, P. M., Shah, M. I. & Sivaprakasam, M. (2016). Arterial compliance probe for calibration free pulse pressure measurement. 2016 IEEE International Symposium on Medical Measurements and Applications, MeMeA 2016 - Proceedings. doi: 10.1109/MEMEA.2016.7533810.

Joseph, J., Singh, S. G. & Vanjari, S. R. K. (2018). Fabrication and characterization of SU-8-based capacitive micromachined ultrasonic transducer for airborne applications. Journal of Micro/Nanolithography, MEMS, and MOEMS, 17(01), 1. doi: 10.1117/1.jmm.17.1.015003.

Joseph, J., Ma, B. & Khuri-Yakub, B. T. (2022). Applications of Capacitive Micromachined Ultrasonic Transducers: A Comprehensive Review. IEEE Transactions on Ultrasonics, Ferroelectrics, and Frequency Control, 69(2), 456–467. doi: 10.1109/TUFFC.2021.3112917,.

Joshi, S. V., Moghimi, S. et al. (2024). Flexible micromachined ultrasound transducers (MUTs) for biomedical applications. Microsystems & Nanoengineering. doi: 10.1038/s41378-024-00783-5.

Joshi, S. V., Sadeghpour, S., Kuznetsova, N., Wang, C. & Kraft, M. (2025). Flexible micromachined ultrasound transducers (MUTs) for biomedical applications. Microsystems and Nanoengineering, 11(1), 1–21. doi: 10.1038/S41378-024-00783-5;SUBJMETA=166,511,639,925,927,987;KWRD=ELECTRICAL+AND+ELECTRONIC+ENGINEERING,SE

Judy, J. W. (2001). Microelectromechanical systems (MEMS):
}fabrication, design and applications. Smart Materials and Structures, 10(6), 1115. doi: 10.1088/0964-1726/10/6/301.

Jung, S. Y., Han, D. H., Ning, R., Kim, M. S., Choi, H. J., Jang, H. W. & Baek, S. H. (2024). Extreme sputtering: Epitaxy of multifunctional oxides heterostructures. Journal of Advanced Ceramics, 13(12), 1919–1930. doi: 10.26599/JAC.2024.9220988.

Kachuee, M., Kiani, M. M., Mohammadzade, H. & Shabany, M. (2017). Cuffless Blood Pressure Estimation Algorithms for Continuous Health-Care Monitoring. IEEE Transactions on Biomedical Engineering, 64(4), 859–869. doi: 10.1109/TBME.2016.2580904,.

Kaltenbrunner, M., Sekitani, T. et al. (2013). An ultra-lightweight design for imperceptible plastic electronics. Nature, 499, 458–463.

Kavallaris, N. I. & Suzuki, T. (2018). Micro-Electro-Mechanical-Systems (MEMS). Springer, Cham. doi: 10.1007/978-3-319-67944-0{_}1.

Keçili, R., Büyüktiryaki, S. & Hussain, C. M. (2020). Micro total analysis systems with nanomaterials. Handbook of Nanomaterials in Analytical Chemistry: Modern Trends in Analysis, 185–198. doi: 10.1016/B978-0-12-816699-4.00008-6.

Kemmochi, M., Nawa, Y., Ohno, S., Sawashita, Y., Terada, H. & Oba, K. (2022). Analysis of the radial and ulnar arteries using ultrasound and a vascular visualization device in children. Pediatric Anesthesia, 32(6), 747–753. doi: 10.1111/PAN.14434.

Kenawy, S. H. & Khalil, A. M. (2020). Advanced ceramics and relevant polymers for environmental and biomedical applications. Biointerface Research in Applied Chemistry, 10(4), 5747–5754. doi: 10.33263/BRIAC104.747754.

Keren Deng & Wen, H. k. (1992). A study of static friction between silicon and silicon compounds. Journal of Micromechanics and Microengineering, 2(1), 14. doi: 10.1088/0960-1317/2/1/004.

Khan, Y., Thielens, A., Muja, N. & Arias, A. C. (2016). Flexible and stretchable electronics for wearable health monitoring: Printed and organic devices. Advanced Healthcare Materials, 5(6), 709–735. doi: 10.1002/adhm.201500680.

Khuri-Yakub, B. T. & Oralkan, O. (2011a). Capacitive micromachined ultrasonic transducers for medical imaging and therapy. Journal of Micromechanics and Microengineering, 21(5), 054004. doi: 10.1088/0960-1317/21/5/054004.

Khuri-Yakub, B. T. & Oralkan, O. (2011b). Capacitive micromachined ultrasonic transducers for medical imaging and therapy. Journal of Micromechanics and Microengineering, 21(5), 054004. doi: 10.1088/0960-1317/21/5/054004.

Kim, B. J. & Meng, E. (2015). Review of polymer MEMS micromachining. Journal of Micromechanics and Microengineering, 26(1). doi: 10.1088/0960-1317/26/1/013001.

Kim, J. H., Lee, C. H., Park, B. H. & Park, K. K. (2023a). The Effect of Cell-to-Cell Variation in CMUTs on Quality Factor and Frequency Noise. Proc. IEEE Int. Ultrasonics Symposium (IUS). doi: 10.1109/IUS51837.2023.10307600.

Kim, J. H., Lee, C. H., Park, B. H. & Park, K. K. (2023b). The effect of cell-to-cell variation in CMUTs on quality factor and frequency noise. IEEE International Ultrasonics Symposium, IUS. doi: 10.1109/IUS51837.2023.10307600.

Klotz, S., Hay, I., Dickstein, M. L., Yi, G. H., Wang, J., Maurer, M. S., Kass, D. A. & Burkhoff, D. (2006). Single-beat estimation of end-diastolic pressure-volume relationship: A novel method with potential for noninvasive application. American Journal of Physiology - Heart and Circulatory Physiology, 291(1), 403–412. doi: 10.1152/AJPHEART.01240.2005,.

Ko, S. H., Bandyk, D. F., Hodgkiss-Harlow, K. D., Barleben, A. & Lane, J. (2015). Estimation of brachial artery volume flow by duplex ultrasound imaging predicts dialysis access maturation. Journal of Vascular Surgery, 61(6), 1521–1528. doi: 10.1016/j.jvs.2015.01.036.

Kremkau, F. W. & Taylor, K. J. (1986). Artifacts in ultrasound imaging. Journal of Ultrasound in Medicine, 5(4), 227–237. Consulted at https://onlinelibrary.wiley.com/doi/abs/10.7863/jum.1986.5.4.227.

Kupnik, M., Ho, M. C., Vaithilingam, S. & Khuri-Yakub, B. T. (2011). CMUTs for air coupled ultrasound with improved bandwidth. IEEE International Ultrasonics Symposium, IUS, 592–595. doi: 10.1109/ULTSYM.2011.0143.

Lee, C., Kim, J. Y. & Kim, C. (2018). Recent progress on photoacoustic imaging enhanced with microelectromechanical systems (MEMS) technologies. Micromachines, 9(11). doi: 10.3390/MI9110584.

Lee, Y. C., Kong, M. & Zhang, Y. (2016). Microelectromechanical systems and packaging. Materials for Advanced Packaging, Second Edition, 697–731. doi: 10.1007/978-3-319-45098-8{_}16/FIGURES/30.

Lei, Y., Gao, Z., Gan, G., Bai, W., Wei, Y., Wang, B., Yuan, X., Hou, Z., Hong, J. & Dong, S. (2025). A High-Sensitivity, Broadband (1A,1B)-3 Single-Crystal Composite Ultrasonic Transducer. Advanced Functional Materials, 35(11), 2417084. doi: 10.1002/ADFM.202417084;WEBSITE:WEBSITE:ADVANCED;CTYPE:STRING:JOURNAL.

Leslie, S. W. & Sajjad, H. (2023). Anatomy, Abdomen and Pelvis, Renal Artery. StatPearls. Consulted at https://www.ncbi.nlm.nih.gov/books/NBK459158/.

Lethiecq, M., Berson, M., Feuillard, G. & Patat, F. (1996). Principles and Applications of High-Frequency Medical Imaging. Advances in Acoustic Microscopy, 39–102. doi: 10.1007/978-1-4615-5851-4{_}2.

Li, A., Lin, J., Li, H., Yang, Q., Liu, X., Jiang, B., Zhang, Y. & Wang, K. (2022a). A robust and flexible pulse wave sensory array enabling real-time non-invasive blood pressure monitoring. Flexible and Printed Electronics, 7(1), 014014. doi: 10.1088/2058-8585/AC5E0D.

Li, B., Wang, T., Luo, D., Peng, P., Wang, Y., Liu, L., Wang, H. & Liu, H. (2023). Fabric-based ultrasonic sensor with integrated piezoelectric composite for Blood Pressure Monitoring. Advanced Materials Technologies, 8(13). doi: 10.1002/admt.202201814.

Li, H. et al. (2008). Fabrication of single crystal based phased array medical imaging ultrasonic transducers.

Li, J., Ma, Y., Zhang, T., Shung, K. K. & Zhu, B. (2022b). Recent Advancements in Ultrasound Transducer: From Material Strategies to Biomedical Applications. BME Frontiers, 2022. doi: 10.34133/2022/9764501.

Li, J., Ma, Y., Zhang, T., Shung, K. K. & Zhu, B. (2022c). Recent Advancements in Ultrasound Transducer: From Material Strategies to Biomedical Applications. BME Frontiers, 2022. doi: 10.34133/2022/9764501.

Li, Q. & Wang, L. V. (2021). Quantitative ultrasound imaging of soft biological tissues. Ultrasonics, 116, 106521. Consulted at https://www.ncbi.nlm.nih.gov/pmc/articles/PMC8429541/.

Li, Z., Zhang, W., Wang, Z., Liu, S., Wang, J., Zeng, X., Zhao, C., Yilmaz, M., He, C., Jia, L., Zhang, G., Qin, L. & Wang, R. (2025). Fabrication and Testing of a 64-Element CMUT Ring Array for Underwater Ultrasound Imaging. IEEE Transactions on Instrumentation and Measurement, 74, 4512212. doi: 10.1109/TIM.2025.3583366.

Liang, L., Li, Y. & Zhang, P. (2020). Modelling and analysis of bandwidth on CMUTS for medical imaging. IOP Conference Series: Materials Science and Engineering, 768(5), 052102. doi: 10.1088/1757-899x/768/5/052102.

Liang, Z., Guo, J. & Fan, D. (2019). Manipulation, assembling, and actuation of nanomotors by electric tweezers. Robotic Systems and Autonomous Platforms, 3–28. doi: 10.1016/B978-0-08-102260-3.00001-9.

Lifshitz, R. & Roukes, M. L. (2000). Thermoelastic damping in micro- and nanomechanical systems. Phys. Rev. B, 61, 5600–5609. doi: 10.1103/PhysRevB.61.5600.

Liu, J. Y., BA, Xu, J., MD, Forsberg, F., PhD, MD, J.-B. L. & FAIUM. (2019). CMUT/CMOS-based Butterfly iQ – A Portable Personal Sonoscope. ADVANCED ULTRASOUND IN DIAGNOSIS AND THERAPY, 3(3), 115–118. doi: 10.37015/AUDT.2019.190819.

Liu, Z., Yoshida, S., Horsley, D. A. & Tanaka, S. (2022). Fabrication and characterization of row-column addressed pMUT array with monocrystalline PZT thin film toward creating ultrasonic imager. Sensors and Actuators A: Physical, 342, 113666. doi: 10.1016/J.SNA.2022.113666.

Lorenz, H., Despont, M., Fahrni, N., Brugger, J., Renaud, P. & de Rooij, N. (1997). SU-8: a low-cost negative resist for MEMS. Journal of Micromechanics and Microengineering, 7(3), 121–124.

Lyshevski, S. E. (2002). MEMS and NEMS : systems, devices, and structures. CRC Press. Consulted at https://www.routledge.com/MEMS-and-NEMS-Systems-Devices-and-Structures/Lyshevski/p/book/9780849312625.

Ma, B., Firouzi, K., Brenner, K. & Khuri-Yakub, B. T. (2019). Wide Bandwidth and Low Driving Voltage Vented CMUTs for Airborne Applications. IEEE Transactions on Ultrasonics, Ferroelectrics, and Frequency Control, 66(11), 1777–1785. doi: 10.1109/TUFFC.2019.2928170.

Mallegni, N., Molinari, G., Ricci, C., Lazzeri, A., La Rosa, D., Crivello, A. & Milazzo, M. (2022). Sensing devices for detecting and processing acoustic signals in Healthcare. Multidisciplinary Digital Publishing Institute. Consulted at https://www.mdpi.com/2079-6374/12/10/835.

Martinez-Rivas, A., González-Quijano, G. K., Proa-Coronado, S., Séverac, C. & Dague, E. (2017). Methods of micropatterning and manipulation of cells for biomedical applications. Micromachines, 8(12). doi: 10.3390/MI8120347.

Meinders, J. M. & Hoeks, A. P. (2004). Simultaneous assessment of diameter and pressure waveforms in the carotid artery. Ultrasound in Medicine & Biology, 30(2), 147–154. doi: 10.1016/J.ULTRASMEDBIO.2003.10.014.

Merbeler, F., Wismath, S., Haubold, M., Bretthauer, C. & Kupnik, M. (2022a). Ultra-Low-Voltage Capacitive Micromachined Ultrasonic Transducers with Increased Output Pressure Due to Piston-Structured Plates. Micromachines, 13(5), 676. doi: 10.3390/mi13050676. Open access.

Merbeler, F., Wismath, S., Haubold, M., Bretthauer, C. & Kupnik, M. (2022b). Ultra-Low-Voltage Capacitive Micromachined Ultrasonic Transducers with Increased Output Pressure Due to Piston-Structured Plates. Micromachines, 13(5), 676. doi: 10.3390/MI13050676.

Merbeler, F., Wismath, S., Haubold, M., Bretthauer, C. & Kupnik, M. (2022c). Ultra-Low-Voltage High-Efficiency CMUTs with Piston-Structured Plates for Fill Level Sensing. IEEE International Ultrasonics Symposium, IUS, 2022-October. doi: 10.1109/IUS54386.2022.9957501.

Mi, X., Qin, L., Liao, Q. & Wang, L. (2017). Electromechanical coupling coefficient and acoustic impedance of 1-1-3 piezoelectric composites. Ceramics International, 43(9), 7374–7377. doi: 10.1016/J.CERAMINT.2017.02.148.

Moisello, E., Novaresi, L., Sarkar, E., Malcovati, P., Costa, T. L. & Bonizzoni, E. (2024). PMUT and CMUT Devices for Biomedical Applications: A Review. IEEE Access, 12, 18640–18657. doi: 10.1109/ACCESS.2024.3359906.

Montalvão, D. (2015). Sensors and Signal Processing - Draft version (unedited and before final revision) o Consulted at https://www.routledge.com/Mechatronics-Fundamentals-and-Applications/Silva-Khoshnoud-Li-Halgamuge/p/book/9781482239317.

Moshrefi, A., Ali, A., Gratuze, M. & Nabki, F. (2025). Design and Fabrication of Multi-Frequency and Low-Quality-Factor Capacitive Micromachined Ultrasonic Transducers. Micromachines, 16(7), 797. doi: 10.3390/mi16070797.

Moshrefi, A., Moghaddam, M. K., Jafarsadeghi Pournaki, I., Ali, A. & Nabki, F. (2024). Advanced Design of Capacitive Micromachined Ultrasonic Transducers with Ultra-Low Quality Factor. IEEE Ultrasonics, Ferroelectrics, and Frequency Control Joint Symposium, UFFC-JS 2024 - Proceedings. doi: 10.1109/UFFC-JS60046.2024.10793970.

Moten. Modelling of a miniature piezoelectric ultrasonic transducer.

Mukhiya, R., Aditi, Prabakar, K., Raghuramaiah, M., Jayapandian, J., Gopal, R., Khanna, V. K. & Shekhar, C. (2015). Fabrication of Capacitive Micromachined Ultrasonic Transducer Arrays with Isolation Trenches Using Anodic Wafer Bonding. IEEE Sensors Journal, 15(9), 5177–5184. doi: 10.1109/JSEN.2015.2437394.

Munir, J., Ain, Q. & Lee, H. J. (2019). Reliability issue related to Dielectric Charging in capacitive micromachined Ultrasonic Transducers: A Review. Microelectronics Reliability, 92, 155–167. doi: 10.1016/j.microrel.2018.12.005.

Myny, K. (2012). The development of flexible integrated circuits based on thin-film transistors. Microelectronic Engineering, 98, 1–6.

Nag, T. & Ghosh, A. (2013). Cardiovascular disease risk factors in Asian Indian population: A systematic r Journal of Cardiovascular Disease Research. Medknow Publications. doi: 10.1016/j.jcdr.2014.01.004.

Nathani, M. U., Nazemi, H., Love, C., Lopez, Y. B., Swaminathan, S. & Emadi, A. (2020). Capacitive Based Micromachined Resonators for Low Level Mass Detection. Micromachines 2021, Vol. 12, Page 13, 12(1), 13. doi: 10.3390/MI12010013.

Newnham, R. E., Safari, A., Giniewicz, J. & Fox, B. H. (1984). Composite piezoelectric sensors. Ferroelectrics, 60(1), 15–21. doi: 10.1080/00150198408017505;WGROUP:STRING:PUBLICATION.

Ng, A. & Swanevelder, J. (2011). Resolution in ultrasound imaging. Continuing Education in Anaesthesia, Critical Care and Pain, 11(5), 186–192. doi: 10.1093/bjaceaccp/mkr030.

Ng, V., Leo, H. L. & Wong, Y.-R. (2023). Development of a non-invasive ultrasound-based blood pressure measurement system. doi: 10.2139/ssrn.4654226.

Nguyen, Y. & Bora, V. (2023). StatPearls. Consulted at https://www.ncbi.nlm.nih.gov/books/NBK556127/.

Nielsen, T. H., Iversen, H. K., Tfelt-Hansen, P. & Olesen, J. (1993). Small arteries can be accurately studied in vivo, using high frequency ultrasound. Ultrasound in Medicine & Biology, 19(9), 717–725. doi: 10.1016/0301-5629(93)90089-7.

Ogbonna, V. E., Popoola, A. P. & Popoola, O. M. (2022). Piezoelectric ceramic materials on transducer technology for energy harvesting: A review. Frontiers in Energy Research, 10, 1051081. doi: 10.3389/FENRG.2022.1051081/BIBTEX.

Omidvar, A., Gerardo, C. D., Rohling, R., Cretu, E. & Hodgson, A. J. (2021). Flexible Polymer-based Capacitive Micromachined Ultrasound Transducers (polyCMUTs): Fabrication and Characterization. IEEE International Ultrasonics Symposium, IUS. doi: 10.1109/IUS52206.2021.9593645.

Oralkan, O., Ergun, A. S., Cheng, C. H., Johnson, J. A., Karaman, M., Lee, T. H. & Khuri-Yakub, B. T. (2002a). Capacitive micromachined ultrasonic transducers: next-generation arrays for medical imaging. IEEE Transactions on Ultrasonics, Ferroelectrics, and Frequency Control, 49(11), 1596–1610. doi: 10.1109/TUFFC.2002.1049742.

Oralkan, O., Ergun, A., Cheng, C.-H., Johnson, J., Karaman, M., Lee, T. & Khuri-Yakub, B. (2003a). Volumetric ultrasound imaging using 2-D CMUT arrays. IEEE Transactions on Ultrasonics, Ferroelectrics and Frequency Control, 50(11), 1581–1594. doi: 10.1109/tuffc.2003.1251142.

Oralkan, , Ergun, A. S., Johnson, J. A., Karaman, M., Demirci, U., Kaviani, K., Lee, T. H. & Khuri-Yakub, B. T. (2002b). Capacitive micromachined ultrasonic transducers: Next-generation arrays for acoustic imaging? IEEE Transactions on Ultrasonics, Ferroelectrics, and Frequency Control, 49(11), 1596–1610. doi: 10.1109/TUFFC.2002.1049742.

Oralkan, , Ergun, A. S., Cheng, C. H., Johnson, J. A., Karaman, M., Lee, T. H. & Khuri-Yakub, B. T. (2003b). Volumetric ultrasound imaging using 2-D CMUT arrays. IEEE Transactions on Ultrasonics, Ferroelectrics, and Frequency Control, 50(11), 1581–1594. doi: 10.1109/TUFFC.2003.1251142.

Pan, P., Wang, W., Ru, C., Sun, Y. & Liu, X. (2017). MEMS-based platforms for mechanical manipulation and characterization of cells. Journal of Micromechanics and Microengineering, 27(12). doi: 10.1088/1361-6439/AA8F1D.

Papaioannou, T. G., Protogerou, A. D., Vrachatis, D., Konstantonis, G., Aissopou, E., Argyris, A., Nasothimiou, E., Gialafos, E. J., Karamanou, M., Tousoulis, D. & Sfikakis, P. P. (2016). Mean arterial pressure values calculated using seven different methods and their associations with target organ deterioration in a single-center study of 1878 individuals. Hypertension Research 2016 39:9, 39(9), 640–647. doi: 10.1038/hr.2016.41.

Pappalardo, M., Caliano, G., Savoia, A. S. & Caronti, A. (2008). Micromachined ultrasonic transducers. Piezoelectric and Acoustic Materials for Transducer Applications, 453–478. doi: 10.1007/978-0-387-76540-2{_}22/COVER.

Park, S., Yoon, I., Lee, S., Kim, H., Seo, J. W., Chung, Y., Unger, A., Kupnik, M. & Lee, H. J. (2018). CMUT-based resonant gas sensor array for VOC detection with low operating voltage. Sensors and Actuators B: Chemical, 273, 1556–1563. doi: 10.1016/J.SNB.2018.07.043.

Parker, K. J. (2022). Power laws prevail in ultrasound-tissue interactions. Frontiers in Physics, 10, 854. Consulted at https://www.ncbi.nlm.nih.gov/pmc/articles/PMC9118335/.

Pattanaik, P. & Ojha, M. (2023). Review on challenges in MEMS technology. Materials Today: Proceedings, 81, 224–226. doi: 10.1016/J.MATPR.2021.03.142.

Peller, S., Bierl, R. & Hagelauer, A. (2024). Designing Capacitive Micromachined Ultrasonic Transducer (CMUT) Based Sensors for Low Frequency Airborne Applications. Proceedings of IEEE Sensors. doi: 10.1109/SENSORS60989.2024.10785117.

Pen, Y., Pala, S., Shao, Z., Ding, H., Xie, J. & Lin, L. (2022). Subcutaneous and Continuous Blood Pressure Monitoring by PMUTs in an Ambulatory Sheep. Proceedings of the IEEE International Conference on Micro Electro Mechanical Systems (MEMS), 2022-January, 416–419. doi: 10.1109/MEMS51670.2022.9699550.

Peng, C., Chen, M., Sim, H. K., Zhu, Y. & Jiang, X. (2021a). Noninvasive and Nonocclusive Blood Pressure Monitoring via a Flexible Piezo-Composite Ultrasonic Sensor. IEEE Sensors Journal, 21(3), 2642–2650. doi: 10.1109/JSEN.2020.3021923.

Peng, C., Chen, M., Spicer, J. B. & Jiang, X. (2021b). Acoustics at the nanoscale (nanoacoustics): A comprehensive literature review. Part II: Nanoacoustics for biomedical imaging and therapy. Sensors and Actuators A: Physical, 332, 112925. doi: 10.1016/J.SNA.2021.112925.

Perçin, G. & Khuri-Yakub, B. T. (2002). Piezoelectrically actuated flextensional micromachined ultrasound transducers - II: Fabrication and experiments. IEEE Transactions on Ultrasonics, Ferroelectrics, and Frequency Control, 49(5), 585–595. doi: 10.1109/TUFFC.2002.1002457.

Ploquin, M., Basarab, A. & Kouamé, D. (2015). Resolution Enhancement in Medical Ultrasound Imaging. Journal of Medical Imaging, 2(1), 017001. doi: 10.1117/1.JMI.2.1.017001.

Pop, F., Herrera, B., Cassella, C. & Rinaldi, M. (2020). Modeling and Optimization of Directly Modulated Piezoelectric Micromachined Ultrasonic Transducers. Sensors 2021, Vol. 21, Page 157, 21(1), 157. doi: 10.3390/S21010157.

Prabakar, A. C., Killivalavan, G., Sivakumar, D., Chandra Babu Naidu, K., Sathyaseelan, B., Senthilnathan, K., Baskaran, I., Manikandan, E., Rao, B. R., Sarma, M. S. & Ratnamala, A. (2020). Structural, morphological, and magnetic properties of copper zinc cobalt ferrites systems nanocomposites. Biointerface Research in Applied Chemistry, 10(4), 6015–6019. doi: 10.33263/BRIAC104.015019.

Przybyla, R. J., Shelton, S. E., Guedes, A., Izyumin, I. I., Kline, M. H., Horsley, D. A. & Boser, B. E. (2011). In-air rangefinding with an AlN piezoelectric micromachined ultrasound transducer. IEEE Sensors Journal, 11(11), 2690–2697. doi: 10.1109/JSEN.2011.2157490.

Qin, D., Xia, Y., Rogers, J. A., Jackman, R. J., Zhao, X.-M. & Whitesides, G. M. (1998). Microfabrication, Microstructures and Microsystems. 1–20. doi: 10.1007/3-540-69544-3{_}1.

Qiu, Y., Gigliotti, J. V., Wallace, M., Griggio, F., Demore, C. E., Cochran, S. & Trolier-McKinstry, S. (2015). Piezoelectric Micromachined Ultrasound Transducer (PMUT) Arrays for Integrated Sensing, Actuation and Imaging. Sensors 2015, Vol. 15, Pages 8020-8041, 15(4), 8020–8041. doi: 10.3390/S150408020.

Rafiee, P., Khatibi, G. & Zehetbauer, M. (2017). A review of the most important failure, reliability and nonlinearity aspects in the development of microelectromechanical systems (MEMS). Microelectronics International, 34(1), 9–21. doi: 10.1108/MI-03-2015-0026.

Rastegar, S., GholamHosseini, H. & Lowe, A. (2019). Non-invasive continuous blood pressure monitoring systems: current and proposed technology issu Australasian Physical and Engineering Sciences in Medicine. Springer Netherlands. doi: 10.1007/s13246-019-00813-x.

Rey, A. B. A. (2024). Estimation of Blood Pressure by Image-Free, Wearable Ultrasound. Artery Research, (1). doi: 10.1007/s44200-024-00048-6.

Ringgaard, E., Levassort, F., Wang, K., Vaitekunas, J. & Nagata, H. (2024). Lead-Free Piezoelectric Transducers. IEEE Transactions on Ultrasonics, Ferroelectrics, and Frequency Control, 71(1), 3–15. doi: 10.1109/TUFFC.2023.3340950.

Robichaud, A., Cicek, P. V., Deslandes, D. & Nabki, F. (2018). Frequency Tuning Technique of Piezoelectric Ultrasonic Transducers for Ranging Applications. Journal of Microelectromechanical Systems, 27(3), 570–579. doi: 10.1109/JMEMS.2018.2831638.

Rödel, J., Jo, W., Seifert, K. T., Anton, E. M., Granzow, T. & Damjanovic, D. (2009). Perspective on the development of lead-free piezoceramics. Journal of the American Ceramic Society, 92(6), 1153–1177. doi: 10.1111/J.1551-2916.2009.03061.X;SUBPAGE:STRING:FULL.

Rogers, J. A., Someya, T. & Huang, Y. (2010). Materials and mechanics for stretchable electronics. Science, 327(5973), 1603–1607. doi: 10.1126/science.1182383.

Roy, K., Lee, J. E. Y. & Lee, C. (2023). Thin-film PMUTs: a review of over 40 years of research. Microsystems & Nanoengineering 2023 9:1, 9(1), 1–17. doi: 10.1038/s41378-023-00555-7.

Ruan, T., Wang, Q., Hu, Z., Li, L., Xu, Q., Liu, H., Yang, B. & Liu, J. (2025). A sandwich pMUT for the amplification of ultrasound transmission and reception. Applied Physics Letters, 126(14), 143503. doi: 10.1063/5.0250272/3342753.

Sadeghpour, S., Lips, B., Kraft, M. & Puers, R. (2020). Bendable Piezoelectric Micromachined Ultrasound Transducer (PMUT) Arrays Based on Silicon-On-Insulator (SOI) Technology. Journal of Microelectromechanical Systems. doi: 10.1109/JMEMS.2020.2972729.

Sadeghpour, S., Joshi, S. V., Wang, C. & Kraft, M. (2022). Novel Phased Array Piezoelectric Micromachined Ultrasound Transducers (pMUTs) for Medical Imaging. IEEE Open Journal of Ultrasonics, Ferroelectrics, and Frequency Control, 2, 194–202. doi: 10.1109/OJUFFC.2022.3207128.

Salim, M. S., Abd Malek, M., Heng, R., Juni, K. & Sabri, N. (2012). Capacitive micromachined Ultrasonic Transducers: Technology and application. Journal of Medical Ultrasound, 20(1), 8–31. doi: 10.1016/j.jmu.2012.02.001.

Schmid, S., Villanueva, L. G. & Roukes, M. L. (2023). Fundamentals of Nanomechanical Resonators (ed. 2). Cham: Springer. doi: 10.1007/978-3-031-29628-4.

Seabra, C., Belén Amado Rey, A., Seabra, G., Carolina, A., da Silva, F., Rey, A., Belen, A., Seabra, A. C., Silva, A. F., Stieglitz, T., Member, S., Amado-Rey, A. B. & diastolic systolic, D. D. (2017). Blood Pressure Models for Wearable Sensors Blood Pressure Models for Wearable Sensors. IEEE SENSORS JOURNAL, XX, 1. doi: 10.36227/techrxiv.15073383.v2.

Sempionatto, J. R., Lin, M., Yin, L., De la paz, E., Pei, K., Sonsa-ard, T., de Loyola Silva, A. N., Khorshed, A. A., Zhang, F., Tostado, N., Xu, S. & Wang, J. (2021). An epidermal patch for the simultaneous monitoring of haemodynamic and metabolic biomarkers. Nature Biomedical Engineering 2021 5:7, 5(7), 737–748. doi: 10.1038/s41551-021-00685-1.

Senturia, S. D. (2001a). Microsystem Design. Boston: Kluwer Academic Publishers.

Senturia, S. D. (2001b). Microsystem Design. Kluwer Academic Publishers. doi: 10.1007/b117574.

Seo, J., Pietrangelo, S. J., Lee, H. S. & Sodini, C. G. (2015a, 11). Carotid arterial blood pressure waveform monitoring using a portable ultrasound system. Proceedings of the Annual International Conference of the IEEE Engineering in Medicine and Biology Society, EMBS, 2015-November, 5692–5695. doi: 10.1109/EMBC.2015.7319684.

Seo, J., Pietrangelo, S. J., Lee, H. S. & Sodini, C. G. (2015b). Noninvasive arterial blood pressure waveform monitoring using two- Element ultrasound system. IEEE Transactions on Ultrasonics, Ferroelectrics, and Frequency Control, 62(4), 776–784. doi: 10.1109/TUFFC.2014.006904.

Seo, J., Pietrangelo, S. J., Sodini, C. G. & Lee, H. S. (2018). Motion Tolerant Unfocused Imaging of Physiological Waveforms for Blood Pressure Waveform Estimation Using Ultrasound. IEEE Transactions on Ultrasonics, Ferroelectrics, and Frequency Control, 65(5), 766–779. doi: 10.1109/TUFFC.2018.2812124.

Seo, J., Lee, H. S. & Sodini, C. G. (2021). Non-Invasive Evaluation of a Carotid Arterial Pressure Waveform Using Motion-Tolerant Ultrasound Measurements during the Valsalva Maneuver. IEEE Journal of Biomedical and Health Informatics, 25(1), 163–174. doi: 10.1109/JBHI.2020.2995344.

Sewify, A., Antico, M., Alzubaidi, L., Alwzwazy, H. A., Roots, J., Pivonka, P. & Fontanarosa, D. (2025). Systematic Review of Commercially Available Clinical CMUT-Based Systems for Use in Medical Ultrasound Imaging: Products, Applications, and Performance. Sensors, 25(7), 2245. doi: 10.3390/S25072245/S1.

Shahmirzadi, D., Li, R. X. & Konofagou, E. E. (2012). Pulse-wave propagation in straight-geometry vessels for stiffness estimation: Theory, simulations, phantoms and in vitro findings. Journal of Biomechanical Engineering, 134(11). doi: 10.1115/1.4007747,.

Shanbhag, P. P. & Patil, N. S. (2017). BioMicroelectromechanical systems: A novel approach for drug targeting in chronic diseases. New Horizons in Translational Medicine, 3(6), 265–271. doi: 10.1016/J.NHTM.2017.01.001/GALLEY/36/DOWNLOAD/.

Shee, C., Banerjee, S., Alagirusamy, R. & Ali, S. W. (2025). Deployment of piezoelectric transducers for diverse technical applications: A comprehensive review. Results in Engineering, 25, 103881. doi: 10.1016/J.RINENG.2024.103881.

Shen, Z., Xu, J., Li, Z., Chen, Y., Cui, Y. & Jian, X. (2021). An Improved Equivalent Circuit Simulation of High Frequency Ultrasound Transducer. Frontiers in Materials, 8, 663109. doi: 10.3389/FMATS.2021.663109/BIBTEX.

Sherrit, S., Leary, S. P., Dolgin, B. P. & Bar-Cohen, Y. (1999). Comparison of the Mason and KLM Equivalent Circuits for Piezoelectric Resonators in the Thickness Mode.

Shrivastava, A. K., Singh, H. V., Raizada, A. & Singh, S. K. (2015). C-reactive protein, inflammation and coronary heart disease. The Egyptian Heart Journal, 67(2), 89–97. doi: 10.1016/J.EHJ.2014.11.005.

Shrout, T. R. & Zhang, S. J. (2007). Lead-free piezoelectric ceramics: Alternatives for PZT? Journal of Electroceramics, 19(1), 111–124. doi: 10.1007/S10832-007-9047-0/FIGURES/23.

Shung, K. K. & Zipparo, M. J. (1996). Ultrasonic transducers and arrays. IEEE Engineering in Medicine and Biology Magazine, 15(6), 20–30. doi: 10.1109/51.544509.

Smyth, K. & Kim, S. G. (2015). Experiment and simulation validated analytical equivalent circuit model for piezoelectric micromachined ultrasonic transducers. IEEE Transactions on Ultrasonics, Ferroelectrics, and Frequency Control, 62(4), 744–765. doi: 10.1109/TUFFC.2014.006725.

Soleimani, E., Mokhtari-Dizaji, M., Fatouraee, N. & Saberi, H. (2016). Assessing the blood pressure waveform of the carotid artery using an ultrasound image processing method. Ultrasonography, 36(2), 144. doi: 10.14366/USG.16019.

Sun, C. K. (2013). Cardio-ankle vascular index (CAVI) as an indicator of arterial stiffness. Integrated Blood Pressure Control, 6, 27. doi: 10.2147/IBPC.S34423.

Sun, S., Zhang, M., Gao, C., Liu, B. & Pang, W. (2018). Flexible Piezoelectric Micromachined Ultrasonic Transducers Towards New Applications. IEEE International Ultrasonics Symposium, IUS, 2018-October. doi: 10.1109/ULTSYM.2018.8580227.

Sun, S., Wang, J., Zhang, M., Ning, Y., Ma, D., Yuan, Y., Niu, P., Rong, Z., Wang, Z. & Pang, W. (2022). MEMS ultrasonic transducers for safe, low-power and portable eye-blinking monitoring. Microsystems and Nanoengineering, 8(1), 1–14. doi: 10.1038/S41378-022-00396-W;SUBJMETA=166,170,639,925,929,987;KWRD=ELECTRICAL+AND+ELECTRONIC+ENGINEERING,EN

Tang, H. Y., Lu, Y., Jiang, X., Ng, E. J., Tsai, J. M., Horsley, D. A. & Boser, B. E. (2016). 3-D Ultrasonic Fingerprint Sensor-on-a-Chip. IEEE Journal of Solid-State Circuits, 51(11), 2522–2533. doi: 10.1109/JSSC.2016.2604291.

Tawfik, H. H., Alsaiary, T., Elsayed, M. Y., Nabki, F. & El-Gamal, M. N. (2019a). Reduced-gap CMUT implementation in polymumps for air-coupled and underwater applications. Sensors and Actuators A: Physical, 294, 102–115. doi: 10.1016/j.sna.2019.05.009.

Tawfik, H. H., Alsaiary, T., Elsayed, M. Y., Nabki, F. & El-Gamal, M. N. (2019b). Reduced-gap CMUT implementation in polymumps for air-coupled and underwater applications. Sensors and Actuators A: Physical, 294, 102–115. doi: 10.1016/j.sna.2019.05.009.

Teh, K. S. (2017). Additive direct-write microfabrication for MEMS: A review. Frontiers of Mechanical Engineering, 12(4), 490–509. doi: 10.1007/S11465-017-0484-4.

Ter Haar, G. R. (2001). High Intensity Focused Ultrasound for the Treatment of Tumors. Echocardiography, 18(4), 317–322. doi: 10.1046/J.1540-8175.2001.00317.X.

Tung, J., Gower, S., Ooteghem, K. V., Nouredanesh, M. & Gage, W. H. (2021). Point of care TECHNOLOGIES. Digital Health: Exploring Use and Integration of Wearables, 73–84. doi: 10.1016/B978-0-12-818914-6.00008-9.

Unlugedik, A., Atalar, A. & Koymen, H. (2013). Designing an efficient wide bandwidth single cell CMUT for airborne applications using nonlinear effects. IEEE International Ultrasonics Symposium, IUS, 1416–1419. doi: 10.1109/ULTSYM.2013.0359.

Ünlügedik, A., Tasdelen, A., Atalar, A. & Köymen, H. (2014). Designing transmitting CMUT cells for airborne applications. IEEE Transactions on Ultrasonics, Ferroelectrics, and Frequency Control, 61(11), 1899–1910. doi: 10.1109/TUFFC.2014.006457.

Vappou, J., Luo, J., Okajima, K., Di Tullio, M. & Konofagou, E. E. (2011). Non-invasive measurement of local pulse pressure by pulse wave-based ultrasound manometry (PWUM). Physiological measurement, 32(10), 1653. doi: 10.1088/0967-3334/32/10/012.

Vegas, A., Wells, B., Braum, P., Denault, A., Miller Hance, W. C., Kaufman, C., Bremner Patel, M. & Salvatori, M. (2025). Guidelines for Performing Ultrasound-Guided Vascular Cannulation: Recommendations of the American Society of Echocardiography. Journal of the American Society of Echocardiography, 38, 57–91. doi: 10.1016/j.echo.2024.12.004.

Vorp, D. A. (2007). BIOMECHANICS OF ABDOMINAL AORTIC ANEURYSM. Journal of biomechanics, 40(9), 1887. doi: 10.1016/J.JBIOMECH.2006.09.003.

Wang, C., Li, X., Hu, H., Zhang, L., Huang, Z., Lin, M., Zhang, Z., Yin, Z., Huang, B., Gong, H., Bhaskaran, S., Gu, Y., Makihata, M., Guo, Y., Lei, Y., Chen, Y., Wang, C., Li, Y., Zhang, T., Chen, Z., Pisano, A. P., Zhang, L., Zhou, Q. & Xu, S. (2018). Monitoring of the central blood pressure waveform via a conformal ultrasonic device. Nature Biomedical Engineering, 2(9), 687–695. doi: 10.1038/s41551-018-0287-x.

Wang, H., Ma, Y., Yang, H., Jiang, H., Ding, Y. & Xie, H. (2020). MEMS Ultrasound Transducers for Endoscopic Photoacoustic Imaging Applications. Micromachines, 11(10), 928. doi: 10.3390/MI11100928.

Wang, H., Huang, X., Yu, L., Ding, Q., Zhang, H., He, C. & Zhang, W. (2021). Hybrid Cell Structure for Wideband CMUT: Design Method and Characteristic Analysis. Micromachines 2021, Vol. 12, Page 1180, 12(10), 1180. doi: 10.3390/MI12101180.

Wang, T., Kobayashi, T. & Lee, C. (2016a). Highly sensitive piezoelectric micromachined ultrasonic transducer operated in air. Micro and Nano Letters, 11(10), 558–562. doi: 10.1049/MNL.2016.0207.

Wang, X., Yu, Y. & Ning, J. (2016b). Fabrication and Characterization of Capacitive Micromachined Ultrasonic Transducers with Low-Temperature Wafer Direct Bonding. Micromachines, 7(12), 226. doi: 10.3390/MI7120226.

Wang, Z., He, C., Zhang, W., Li, Y., Gao, P., Meng, Y., Zhang, G., Yang, Y., Wang, R., Cui, J., Wang, H., Zhang, B., Ren, Y., Zhen, G., Jiao, X. & Zhang, S. (2022). Fabrication of 2-D Capacitive Micromachined Ultrasonic Transducer (CMUT) Array through Silicon Wafer Bonding. Micromachines, 13(1). doi: 10.3390/MI13010099.

Wear, K. A. (2011). Attenuation and speed of sound in soft tissues: 50 years of progress. Ultrasound in Medicine & Biology, 37(8), 1381–1390. Consulted at https://www.sciencedirect.com/science/article/pii/S0301562911002352.

Welsch, J., Cretu, E., Rohling, R. & Gerardo, C. D. (2022). Ultrathin, High Sensitivity Polymer-based Capacitive Micromachined Ultrasound Transducers (polyCMUTs) for Acoustic Emission Sensing in Fiber Reinforced Polymers. IEEE International Ultrasonics Symposium, IUS, 2022-October. doi: 10.1109/IUS54386.2022.9958226.

Westenberg, J. J., Van Poelgeest, E. P., Steendijk, P., Grotenhuis, H. B., Jukema, J. W. & De Roos, A. (2012). Bramwell-Hill modeling for local aortic pulse wave velocity estimation: A validation study with velocity-encoded cardiovascular magnetic resonance and invasive pressure assessment. Journal of Cardiovascular Magnetic Resonance, 14(1). doi: 10.1186/1532-429X-14-2.

Wong, L. L., Na, S., Chen, A. I., Li, Z., Macecek, M. & Yeow, J. T. (2016). A feasibility study of piezoelectric micromachined ultrasonic transducers fabrication using a multi-user MEMS process. Sensors and Actuators A: Physical, 247, 430–439. doi: 10.1016/J.SNA.2016.06.029.

Wong, S. J., Roy, K., Lee, C. & Zhu, Y. (2024). Thin-Film Piezoelectric Micromachined Ultrasound Transducers in Biomedical Applications: A Review. IEEE Transactions on Ultrasonics, Ferroelectrics, and Frequency Control, 71(6), 622–637. doi: 10.1109/TUFFC.2024.3390807,.

Worthing, R. T. (2016). Using ultrasound to measure arterial diameter for the development of a wearable blood pressure monitoring device. (Ph.D. thesis, University of British Columbia). Consulted at https://open.library.ubc.ca/collections/ubctheses/24/items/1.0320796.

Wu, S., Liu, K., Wang, W., Li, W., Wu, T., Yang, H. & Li, X. (2023). Aluminum Nitride Piezoelectric Micromachined Ultrasound Transducer Arrays for Non-Invasive Monitoring of Radial Artery Stiffness. Micromachines 2023, Vol. 14, Page 539, 14(3), 539. doi: 10.3390/MI14030539.

Xia, F., Peng, Y., Ji, W., Saini, G., Wang, Y. C., Wudaru, A., Yu, X., Luo, M., De Guzman, A., Wang, Z., Yuan, Y., Chien, J. C. & Lin, L. (2025). Alignment-Free, Non-Invasive Blood Vessel Monitoring by Piezoelectric Micromachined Ultrasonic Transducers. Proceedings of the IEEE International Conference on Micro Electro Mechanical Systems (MEMS), 247–250. doi: 10.1109/MEMS61431.2025.10917752.

Xu, L., Wang, P., Xia, P., Wu, P., Chen, X., Du, L., Liu, J., Xue, N. & Fang, Z. (2022). A Flexible Ultrasound Array for Local Pulse Wave Velocity Monitoring. Biosensors, 12(7). doi: 10.3390/BIOS12070479.

Xu, L., Wu, P., Xia, P., Geng, F., Lu, S., Wang, P., Chen, X., Li, Z., Du, L., Liu, S., Li, L., Chang, H. & Fang, Z. (2023). Online continuous measurement of arterial pulse pressure and pressure waveform using ultrasound. Measurement, 220, 113379. doi: 10.1016/J.MEASUREMENT.2023.113379.

Xue, J., Deng, H., Jia, X., Wang, Y., Lu, X., Ding, X., Li, Q. & Yang, A. (2017). Establishing a new formula for estimating renal depth in a Chinese adult population. Medicine (United States), 96(5). doi: 10.1097/MD.0000000000005940.

Yang, H., Liu, H., Chen, J., Gao, X., Chen, C., Wang, Z., Zhang, X., Li, H. & Yin, F. (2024). A PMUT-Based Wearable Ultrasound System for Central Blood Pressure Monitoring. IEEE Ultrasonics, Ferroelectrics, and Frequency Control Joint Symposium, UFFC-JS 2024 - Proceedings. doi: 10.1109/UFFC-JS60046.2024.10793732.

Yang, Y., Tian, H., Wang, Y. F., Shu, Y., Zhou, C. J., Sun, H., Zhang, C. H., Chen, H. & Ren, T. L. (2013). An Ultra-High Element Density pMUT Array with Low Crosstalk for 3-D Medical Imaging. Sensors 2013, Vol. 13, Pages 9624-9634, 13(8), 9624–9634. doi: 10.3390/S130809624.

Yao, W. & Peddi, R. (2016). Customizable silicone materials for MEMS and semiconductor packages. Proceedings of the IEEE/CPMT International Electronics Manufacturing Technology (IEMT) Symposium, 2016-November. doi: 10.1109/IEMT.2016.7761976.

Yi, Z., Liu, Z., Li, W., Ruan, T., Chen, X., Liu, J., Yang, B., Zhang, W., Yi, Z., Li, W., Zhang, W., Liu, Z., Ruan, T., Chen, X., Liu, J. & Yang, B. (2022). Piezoelectric Dynamics of Arterial Pulse for Wearable Continuous Blood Pressure Monitoring. Advanced Materials, 34(16), 2110291. doi: 10.1002/ADMA.202110291.

Zang, J., Fan, Z., Li, P., Duan, X., Wu, C., Cui, D. & Xue, C. (2022). Design and Fabrication of High-Frequency Piezoelectric Micromachined Ultrasonic Transducer Based on an AlN Thin Film. Micromachines 2022, Vol. 13, Page 1317, 13(8), 1317. doi: 10.3390/MI13081317.

Zega, V., Langfelder, G., Falorni, L. G. & Comi, C. (2019). Hardening, softening, and linear behavior of elastic beams in MEMS: An analytical approach. Journal of Microelectromechanical Systems, 28(2), 189–198. doi: 10.1109/JMEMS.2019.2892296.

Zhang, H., Liang, D., Wang, Z., Ye, L., Rui, X. & Zhang, X. (2020a). Fabrication and Characterization of a Wideband Low-Frequency CMUT Array for Air-Coupled Imaging. IEEE Sensors Journal, 20(23), 14090–14100. doi: 10.1109/JSEN.2020.3007068.

Zhang, H., Liang, D., Wang, Z., Ye, L., Rui, X. & Zhang, X. (2020b). Fabrication and Characterization of a Wideband Low-Frequency CMUT Array for Air-Coupled Imaging. IEEE Sensors Journal, 20(23), 14090–14100. doi: 10.1109/JSEN.2020.3007068.

Zhang, L., Yan, K., Ye, L., Luo, X., He, J. & Chou, X. (2024). Design and Fabrication of High-Performance Piezoelectric Micromachined Ultrasonic Transducers Based on Aluminum Nitride Thin Films. Micromachines 2024, Vol. 15, Page 1001, 15(8), 1001. doi: 10.3390/MI15081001.

Zhao, L., Liang, C., Huang, Y., Zhou, G., Xiao, Y., Ji, N., Zhang, Y. T. & Zhao, N. (2023). Emerging sensing and modeling technologies for wearable and cuffless blood pressure monitoring. npj Digital Medicine. Nature Research. doi: 10.1038/s41746-023-00835-6.

Zhao, L., Xia, J., Yang, C. & Lu, Y. (2024). Modeling and experimental studies of mutual acoustic radiation effect on PMUT array. Sensors and Actuators A: Physical, 377, 115677. doi: 10.1016/J.SNA.2024.115677.

Zhou, J., Cheng, C., Qu, M., Lv, D., Liu, W. & Xie, J. (2023a). Continuous and Non-Invasive Monitoring of Blood Pressure Based on Wearable Piezoelectric Micromachined Ultrasonic Transducers Array. Journal of Microelectromechanical Systems, 1–8. doi: 10.1109/JMEMS.2023.3298021.

Zhou, J., Qu, M., Liu, W., Wang, Y., Zhang, G., Zheng, Y. & Xie, J. (2025). Continuous Monitoring of Blood Pressure by Measuring Local Pulse Wave Velocity Using Wearable Micromachined Ultrasonic Probes. IEEE Transactions on Biomedical Engineering. doi: 10.1109/TBME.2024.3514878.

Zhou, S., Xu, K., Fang, Y., Alastruey, J., Vennin, S., Yang, J., Wang, J., Xu, L., Wang, X. & Greenwald, S. E. (2024). Patient-specific non-invasive estimation of the aortic blood pressure waveform by ultrasound and tonometry. Computer Methods and Programs in Biomedicine, 247, 108082. doi: 10.1016/j.cmpb.2024.108082.

Zhou, Z.-B. ., Cui, T.-R. ., Li, D. ., Jian, J.-M. ., Li, Z. ., Ji, S.-R. ., Li, X. ., Xu, J.-D. ., Liu, H.-F. ., Yang, Y. ., Zhou, Z.-B., Cui, T.-R., Li, D., Jian, J.-M., Li, Z., Ji, S.-R., Li, X., Xu, J.-D., Liu, H.-F., Yang, Y. & Ren, T.-L. (2023b). Wearable Continuous Blood Pressure Monitoring Devices Based on Pulse Wave Transit Time and Pulse Arrival Time: A Review. Materials 2023, Vol. 16, Page 2133, 16(6), 2133. doi: 10.3390/MA16062133.

Zhu, J., Liu, X., Shi, Q., He, T., Sun, Z., Guo, X., Liu, W., Sulaiman, O. B., Dong, B. & Lee, C. (2019). Development trends and perspectives of future sensors and MEMS/NEMS. Multidisciplinary Digital Publishing Institute. Consulted at https://www.mdpi.com/2072-666X/11/1/7.

Zhu, K. ., Ma, J. ., Qi, X. ., Shen, B. ., Liu, Y. ., Sun, E. ., Zhang, R., Hernández, M., Ángel, M., Zhu, K., Ma, J., Qi, X., Shen, B., Liu, Y., Sun, E. & Zhang, R. (2022). Enhancement of Ultrasonic Transducer Bandwidth by Acoustic Impedance Gradient Matching Layer. Sensors 2022, Vol. 22, Page 8025, 22(20), 8025. doi: 10.3390/S22208025.

Zorman, C. A. & Mehregany, M. (2004). Materials Aspects of Micro- and Nanoelectromechanical Systems. shnt, 203. doi: 10.1007/3-540-29838-X{_}7.